Deep Mining 2017: Eighth International Conference on Deep and High Stress Mining – J Wesseloo (ed.)

doi:10.36487/ACG_rep/1704_0.1_Tarasov

Shear ruptures of extreme dynamics in laboratory and natural conditions

BG Tarasov *The University of Western Australia, Australia*

Abstract

In the Earth's crust shear ruptures are responsible for macroscopic dynamic failure causing earthquakes. Shear ruptures induced by and triggered by the mining-induced stress change sometimes result in damaging rockbursts. The fundamental mechanism of the shear rupture is critically linked to the magnitude of ground motion, and hence, any resulting damage. For the effective management of seismic hazard both from natural and mining-related causes, a comprehensive understanding of the fundamental mechanism of the shear rupture is crucial. In recent years it has been observed that shear ruptures can propagate with extreme velocities exceeding the shear wave speed. Experiments show that a remarkable feature of extreme ruptures is the fact that friction reduces toward zero in the rupture head. Coseismic reduction in friction is critical in accelerating the fault slip and to the magnitude of ground shaking which affects the amount of potential earthquake and rockburst damage. Despite the critical importance, physical processes which determine the dramatic weakening of friction are still unclear and continue to be vigorously debated. The second unresolved question is about the source of energy which provides extreme rupture dynamics. This paper shows that the nature of extreme ruptures in intact rocks and in pre-existing faults with frictional and coherent interfaces is the same. It demonstrates that in all types of extreme ruptures, the fault weakening can be explained by a recently-proposed shear rupture mechanism associated with the intensive tensile-cracking process in the rupture tip observed for all extreme ruptures. The tensile-cracking process creates, in certain conditions, a fan-like fault structure, the shear resistance of which is extremely low. The fan-structure represents the basis of a self-sustaining natural mechanism of stress intensification in the rupture head providing the driving power for rupture propagation with extreme velocities. The fan-mechanism causes dramatic embrittlement of intact hard rocks under high stress and makes transient strength of intact hard rocks during the rupture propagation significantly less than the frictional strength. This paper introduces features of the fan-mechanism operation in primary ruptures and in natural complex faults and proposes an alternative view on the nature of earthquakes and shear rupture rockbursts generated by extreme ruptures.

Keywords: *super shear, extreme rupture, fan-mechanism, Ortlepp shears, rockburst, earthquake*

1 Introduction

Shear rupture occurs in a plane shearing failure mode resulting from relative sliding of rupture faces near the rupture tip caused by shear stresses. The propagation of the rupture tip can occur in both static and dynamic regimes. Until recently, classic dynamic fracture theories predicted that the rupture velocity v (velocity of the rupture tip propagation) cannot exceed the velocity of the free surface or Rayleigh wave c_R that is less than the shear c_S and compression c_P wave speed ($v < c_R < c_S < c_P$). However, recent observations of shear ruptures during earthquakes and in laboratory experiments show that shear ruptures can propagate with velocities exceeding the shear wave speed c_S (Heaton 1990; Olsen et al. 1997; Ohnaka & Shen 1999; Rosakis et al. 1999; Lei et al. 2000; Rosakis 2002; Xia et al. 2004; Rubinstein et al. 2004; Lykotrafitis et al. 2006; Griffith et al. 2009; Ben-David et al. 2010; Ngo et al. 2012; Ghaffari et al. 2014). Such dynamic ruptures and corresponding rupture velocities are called 'supershear' or 'intersonic' ($c_S < v < c_P$). For example, for the 2001 Kunlun earthquake the rupture velocity was identified as 6 km/s (Wen et al. 2009). In this paper shear ruptures propagating faster than c_R will be referred to as 'extreme ruptures'.

Extreme ruptures can propagate through intact materials and along pre-existing faults with frictional and coherent (bonded) interfaces. It is generally accepted that earthquakes are normally generated on the basis of pre-existing faults, this provides the grounds to consider the earthquake mechanism as frictional stick-slip instability (Olsen et al. 1997; Scholz 2002). At the same time special studies conducted in South African ultra-deep mines identified that shear rupture rockbursts, which are seismically undistinguished from earthquakes, are caused by extreme shear ruptures generated in intact rock mass (McGarr et al. 1979; Ortlepp 1997). These ruptures are known as Ortlepp shears (Van Aswegen 2008).

Intensive laboratory studies of extreme ruptures, however, have been mainly concentrated on the rupture development in pre-existing faults (e.g. Ohnaka & Kuwahara 1990; Ohnaka & Shen 1999; Lei et al. 2000; Samudrala et al. 2002; Rubinstein et al. 2004; Lykotrafitis et al. 2006; Griffith et al. 2009; Ben-David et al. 2010; Lu et al. 2010; Ghaffari et al. 2014). One of the reasons for this is the fact that in pre-existing faults the interface for shear rupture propagation is pre-determined, which facilitates the rupture process observation and registration, unlike extreme ruptures in intact materials. The following three key features inherent to all extreme ruptures propagating in pre-existing interfaces have been identified experimentally (e.g. Lei et al. 2000; Ghaffari et al. 2014, Rosakis et al. 1999; Samudrala et al. 2002; Griffith et al. 2009; Rubinstein et al. 2004; Ben-David et al. 2010):

1. Dramatic decrease in friction (strength weakening) of the rupture head.
2. High slip velocity in the rupture head.
3. Intensive tensile-cracking process in the rupture tip.

Coseismic reduction in friction is critical in accelerating the fault slip, and to the magnitude of ground shaking, which affects the amount of potential earthquake damage. Despite the critical importance, physical processes which determine the dramatic weakening of friction are still unclear. The general explanation for dramatic fault weakening is that the high slip velocity in the rupture tip causes low friction. This approach is known as strong velocity-weakening friction. Some velocity-weakening models blame frictional heating (Kanamori & Heaton 2000; Ben-Zion 2001; Di Toro et al. 2004; Rice 2006; Ben-David et al. 2010). Indeed, if the width of slip localisation during rapid fault slip is sufficiently thin, conventional levels of friction lead to frictional melting (Kanamori & Heaton 2000). However, traces of melting are not found in interfaces of laboratory specimens after propagation of extreme ruptures or in exhumed earthquake fault zones in nature (e.g. Sibson 1992; Magloughlin & Spray 1992). To solve this heat flow paradox it has been suggested that strong velocity-weakening friction can be caused by a dynamic reduction in normal stress or by fault lubrication (Melosh 1979; Heaton 1990; Rice 1992; Brune et al. 1993; Andrews & Ben-Zion 1997; Di Toro et al. 2004) due to processes such as high pore pressure in the fault zone, intense compressional waves possibly generated by extreme ruptures, or gel formation at high slip velocities.

Despite the fact that models based on the velocity-weakening approach propose a number of physical processes which can potentially cause low friction, consensus on which is the real weakening process in the rupture head has not been reached. It should be emphasised that in extreme ruptures two features – high slip velocity and low friction – manifest themselves together. The basic question is ‘which comes first: the high slip velocity or the low friction?’. All existing models assume that high slip velocity in the rupture head comes first which then causes low friction. This approach is based on the knowledge that high slip velocity can induce different processes leading to reduction of friction. At the same time it is still unclear which mechanism provides high slip velocity in the rupture tip before the reduction of friction. This paper demonstrates that the generally accepted velocity-weakening approach is fallacious. It proposes an alternative concept according to which low friction comes first which then causes high slip velocity. Such unusual interrelation between slip velocity and friction in the rupture head is provided by a recently identified shear rupture mechanism (Tarasov 2014, 2016a).

The mechanism was identified theoretically on the basis of comprehensive analysis of side effects accompanying extreme ruptures. This mechanism is associated with the intensive tensile-cracking process in the rupture tip observed for all types of extreme ruptures (e.g. Lei et al. 2000; Ghaffari et al. 2014, Rosakis et al. 1999; Samudrala et al. 2002; Griffith et al. 2009; Rubinstein et al. 2004; Ben-David et al. 2010).

The tensile-cracking process creates, in certain conditions, a special fan-like fault structure; the shear resistance of which is extremely low (up to an order of magnitude less than the frictional strength). The fan-structure representing the rupture head causes strong interface weakening observed in extreme ruptures. Furthermore, the fan-structure represents the basis of a self-sustaining natural mechanism of stress intensification in the rupture head providing the driving power for rupture propagation with extreme velocities. This paper proposes that the fan-mechanism represents the universal mechanism of extreme rupture dynamics in pre-existing frictional and coherent interfaces and in intact materials.

As mentioned before, extreme ruptures also occur through intact rock in the form of Ortlepp shears. The role of the fan-mechanism in creation of extreme ruptures in intact hard rocks is also considered in this paper. The new mechanism is activated in intact hard rocks at highly confined compression at the post-peak stage of failure. Figure 1 shows features of post-peak properties of rocks of different hardness at different levels of confining pressure σ_3. The rock hardness here is characterised by the level of uniaxial compressive strength (UCS). The rock hardness increases from left to right. For the left rock (marble) with UCS ≈ 130 MPa rising σ_3 increases post-peak ductility (Rummel & Fairhurst 1970). All dotted lines reflecting negative post-peak modulus $M = d\sigma/d\varepsilon$ characterise rock behaviour under all σ_3 as Class I (Wawersik & Fairhurst 1970). The middle rock with UCS ≈ 180 MPa (quartzite) demonstrates that within a certain range of σ_3 post-peak behaviour becomes of Class II, characterised by positive post-peak modulus. Despite the Class II behaviour, post-peak control is achievable for rocks of this hardness.

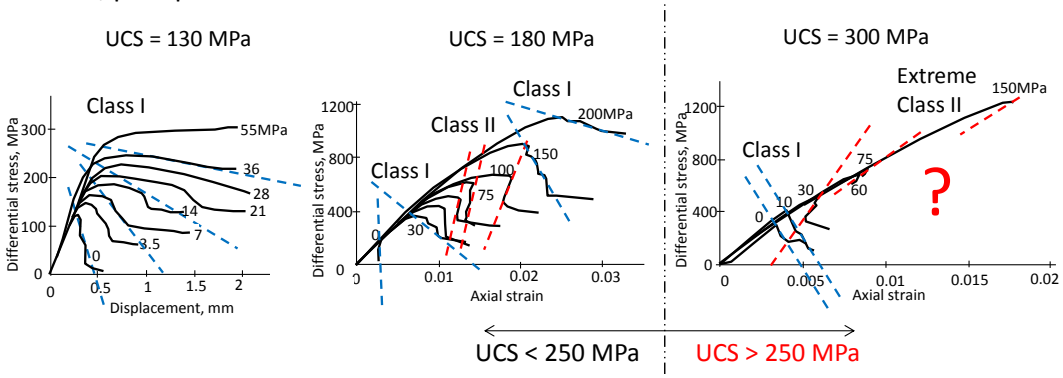

Figure 1 Three sets of stress–strain curves illustrating features of variation in post-peak modulus with rising confining pressure for rocks of different hardness characterised by levels of UCS

Analysis of available experimental data and additional experimental studies conducted in Tarasov (2010) and Tarasov and Randolph (2011), show that post-peak properties of hard rocks characterised by UCS > 250 MPa are still experimentally unexplored at highly confined compression corresponding to earthquake seismogenic depths and similar highly confined stress conditions in deep mines. These rocks are normally represented by highly metamorphic and volcanic rocks with fairly fine grains forming a very compact structure. The failure mode of these rocks at high σ_3 is shear rupture of extreme dynamics. Experiments show that the post-peak rupture control at these conditions is impossible even on ultra-stiff servo-controlled testing machines. The set of curves on the right in Figure 1 obtained on dolerite specimens (UCS = 300 MPa) illustrates typical behaviour of such hard rocks under different levels of confining pressure σ_3. Increasing confining pressure causes post-peak rock embrittlement associated with transition from Class I to Class II behaviour. At high confining pressure ($\sigma_3 \geq 60$ MPa for dolerite) the post-peak failure associated with extreme rupture dynamics becomes uncontrollable and abnormally violent. A special analysis (Tarasov 2014) showed that at the start of spontaneous failure the post-peak modulus is almost equal to the unloading elastic modulus, which indicates the extreme Class II behaviour characterised by extremely low post-peak rupture energy. Complete post-peak properties of hard rocks with UCS > 250 MPa at highly confined compression are still unknown.

It is important to note that the unexplored hard rocks (highly metamorphic and volcanic) represent about 90% of the Earth's crust including the seismogenic layer. Furthermore, the range of confining pressure σ_3 at which the post-peak control is impossible in laboratory corresponds to the sesmogenic depths. This fact allows supposing that the unknown post-peak properties of hard rocks at high σ_3 can represent a key factor

in dynamic activity of the rock mass within the seismogenic layer of the Earth's crust. The new knowledge of the fan-mechanism allows deriving the inaccessible information about real post-peak properties of hard rocks at high confining stresses. The fan-mechanism provides dramatic embrittlement of hard rocks at conditions of great depths and makes transient strength of intact hard rocks during the rupture propagation significantly less than the frictional strength.

This paper introduces features of the fan-mechanism operation in primary ruptures and in natural complex faults generated in hard rocks and proposes an alternative view on the nature of earthquakes and shear rupture rockbursts generated by extreme ruptures.

The structure of this paper is as follows:

- Section 2 introduces the general principles of the fan-mechanism.
- Section 3 presents physical and mathematical models of the fan-mechanism.
- Section 4 discusses unique features of the fan-mechanism illustrated by experimental results obtained for extreme ruptures on pre-existing interfaces.
- Section 5 discusses post-peak properties of hard rocks at highly confined compression governed by the fan-mechanism.
- Section 6 analyses features of the fan-mechanism generation in natural complex and segmented faults.
- Section 7 shows the role of the fan-mechanism in generation of shear rupture rockbursts (Ortlepp shears).
- Section 8 proposes an alternative understanding of the lithospheric strength and earthquake mechanisms caused by extreme ruptures governed by the fan-mechanism.

2 General ideas of the fan-mechanism

Shear ruptures are known to propagate through brittle material because of the creation of an echelon of tensile (or extension) cracks at the rupture tip (Reches & Lockner 1994). Figure 2 illustrates features of shear rupture propagation in brittle intact rocks. Figure 2(a) shows a shear rupture propagating from left to right under the effect of stresses applied. Here σ_1, σ_3, σ_n and τ correspondingly represent the applied major and minor stresses and the induced normal and shear stresses. According to Reches and Lockner (1994), the dilation of one tensile-crack induces the dilation of a closely spaced neighbouring crack, thereby sequentially forming an array of tensile cracks. These tensile cracks are generated along the major stress that is at angle $\alpha_o \approx (30° \div 40°)$ to the shear rupture plane and create an echelon of inclined inter-crack slabs which can be treated as domino-like blocks (Reches & Lockner 1994; Horii & Nemat-Nasser 1985).

Photographs in Figures 2(b) and 2(e) illustrate the typical fault structure of dynamic shear ruptures (modified from Ortlepp 1997). They show fragments of Ortlepp shears generated in intact quartzite which created severe shear rupture rockbursts in ultra-deep South African mines. The fault structure consists of an echelon of inclined tensile cracks and inter-crack slabs. We will call hereafter the inter-crack slabs as domino-blocks. Horizontal lines in Figure 2(b) indicate the rupture faces.

It was observed that domino-blocks (slabs) are subjected to rotation because of the relative displacement of the rupture faces (Peng & Johnson 1972; King & Sammis 1992; Reches & Lockner 1994). This fact is illustrated by Figure 2(e). Here angle α_0 indicates the initial orientation of domino-blocks, while angle β corresponds to block rotation. Two fundamentally different behaviours of domino-blocks at rotation can be distinguished depending on the material strength, the domino-block geometry and loading conditions:

- Frictional shear — characterised by domino-block collapse, which creates friction within the fracture head (Peng & Johnson 1972; King & Sammis 1992; Reches & Lockner 1994). The structure of the rupture head for such block behaviour is illustrated in Figure 2(c).

- Fan-hinged shear — characterised by domino-block rotation without collapse. Because the relative shear displacement of the rupture faces increases with distance from the fracture tip, the successively generated and rotated domino blocks form a fan-structure that represents the rupture head (Tarasov 2014). In this case, the domino blocks behave as hinges between the moving (sliding) rupture faces that causes a dramatic decrease of friction in the rupture head. For the fan-mechanism to generate, the following requirement has to be fulfilled. Strength of the material forming domino-blocks and the geometry of blocks must provide the block rotation without collapse at the applied stress conditions.

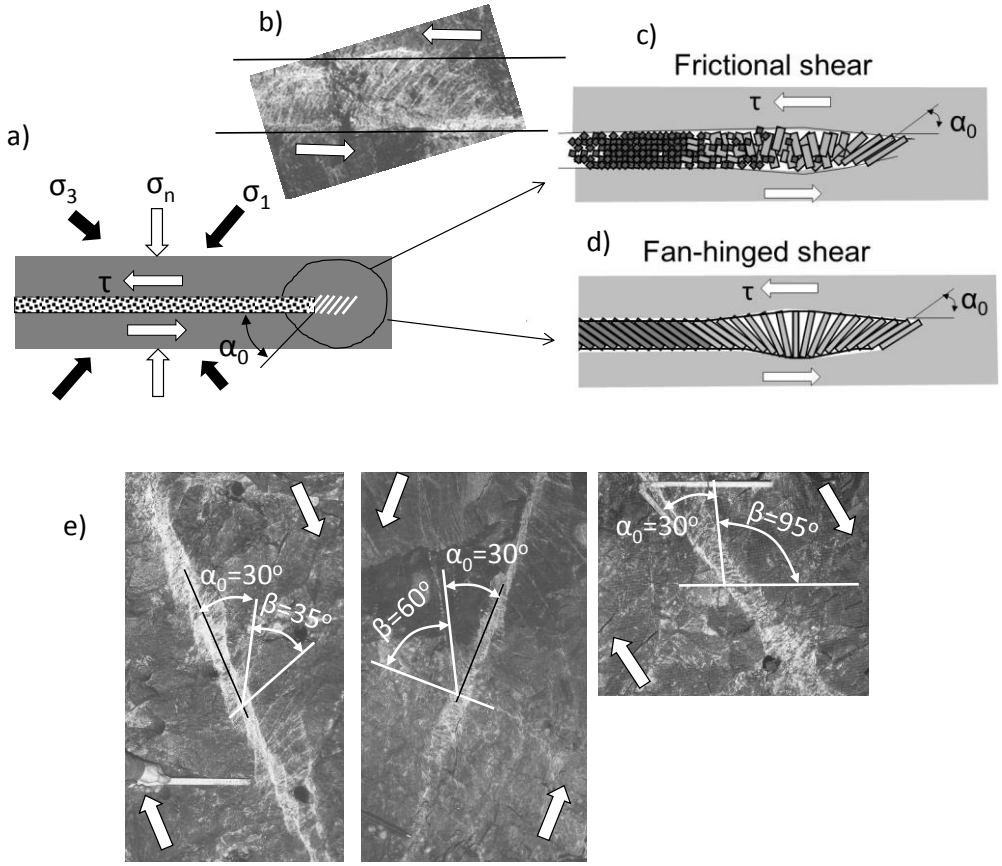

Figure 2 General principles of the fan-structure formation in shear ruptures propagating through intact rocks (modified photographs from Ortlepp 1997)

It will be shown in Section 5 that within intact rocks shear ruptures governed by the fan-mechanism can be generated in hard rocks at highly confined compression (under high confining pressures σ_3). High confining pressures, σ_3, are required to decrease the length of tensile cracks and, consequently, domino-blocks up to the level at which the rotation of blocks can occur without collapse. Three stages of the fan-structure formation in a specimen of intact rock are shown in Figure 3(a). For pre-existing interfaces the length of domino-blocks is determined by the interface thickness. Figures 3(b) and 3(c) schematically show specimens with bonded and frictional interfaces of thickness h. Both side views and cross-sections of the interfaces are shown. The bonded interface is represented by brittle bond — the strength of which is lower than the bulk material. The frictional interface is formed by contacted asperities (coloured spots). In accordance with modern frictional theory (Bowden & Tabor 2001) the applied normal force P is supported by an ensemble of microcontacts that are 'welded' together due to extremely high compressive stresses generated in them. The 'welded' contacts represent zones of the intact material.

The rupture propagation along the bonded and frictional interfaces is provided by the same principles as within intact materials: the consecutive creation of tensile-cracks and domino-blocks within the bond or 'welded' asperities followed by rotation of domino-blocks due to shearing of rupture faces. If the interface

thickness, h, is relatively large the long domino-blocks will collapse at rotation and the rupture propagation will occur in accordance with the frictional mechanism. In thin interfaces represented by brittle material the fan-mechanism can be generated because short domino-blocks can withstand the rotation without collapse and operate as hinges between shearing rupture faces. It should be noted that shear ruptures of extreme dynamics (including supershear) have been observed in laboratory experiments with very thin and carefully prepared interfaces. For example, in experiments on extreme dynamics with frictional interfaces (Ohnaka & Shen 1999; Rubinstein et al. 2004; Lykotrafitis et al. 2006; Ben-David et al. 2010) the interface thickness determined by asperities was about a few microns; for bonded interfaces the thickness was about 30 µm (Rosakis 2002; Samudrala et al. 2002; Griffith et al. 2009); for intact rocks tested at high confining pressures the rupture thickness was between 50–100 µm (Tarasov 2014).

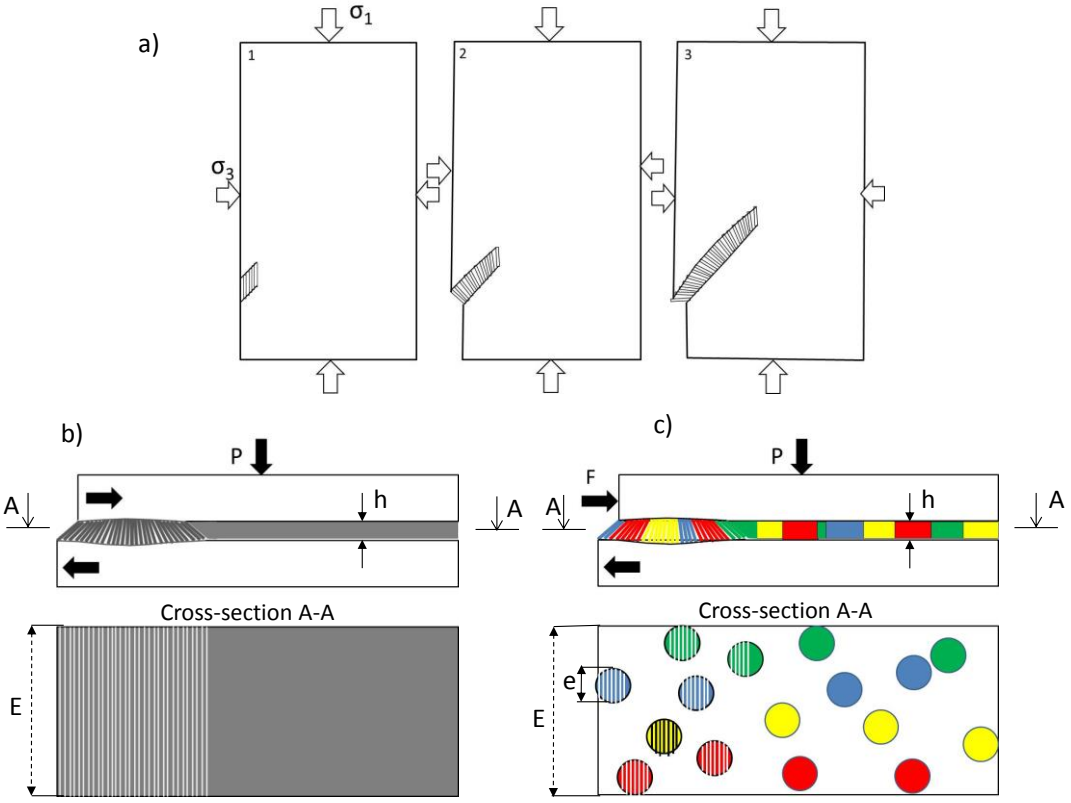

Figure 3 Fan-mechanism in (a) intact; and, (b), (c) pre-cut specimens with bonded and frictional interfaces. Both side views and cross-sections of the pre-cut interfaces are shown

3 Conceptual physical and mathematical models of the fan-mechanism

It should be noted that the fan-structure has never been observed in ruptures. This can be explained by the fact that the fan-structure, of very low shear resistance representing the rupture head, propagates with extreme dynamics and leaves behind a row of domino-blocks completed their rotation or a destroyed structure. The use of modern techniques (e.g. Lei et al. 2000; Ghaffari et al. 2014, Rosakis et al. 1999; Samudrala et al. 2002; Griffith et al. 2009; Rubinstein et al. 2004; Ben-David et al. 2010) has not allowed visualising the behaviour of the microstructure during the rupture propagation. The fan-structure generated in the rupture head was identified by comprehensive analysis of different side effects accompanying the rupture process (Tarasov 2014). Some basic features of the fan-structure will be illustrated in this section by physical and mathematical models. As noted before, shear ruptures propagate due to the consecutive creation of tensile cracks accompanied by the formation of identical domino-blocks from the interface material in the rupture tip. The mechanism responsible for the creation of identical domino-blocks was considered in Reches and Lockner (1994). In the models presented here we study the role of the fan-structure, formed on the basis of domino-blocks, in shear fracture development. To simplify the models we present the future fault as consisting of 'predetermined' domino-blocks.

3.1 Physical model

A video illustrating fan-structure formation and propagation by a physical model can be seen in Tarasov (2016b). Figure 4(a) shows images of the physical model representing different stages of this process. Figure 4(a-I) shows the initial structure of the future fault that is represented by 'predetermined' domino-blocks inclined at an angle α_0 to the rupture plane. All blocks are bonded together to simulate a 'monolithic' material. The bond strength is less than that of the block material. The row of domino blocks is located between two layers, AB and CD, representing the two opposite faces of the rupture. The upper and lower faces are fixed to the corresponding ends of each domino block. The entire row of blocks is loaded with an evenly distributed weight, σ_p.

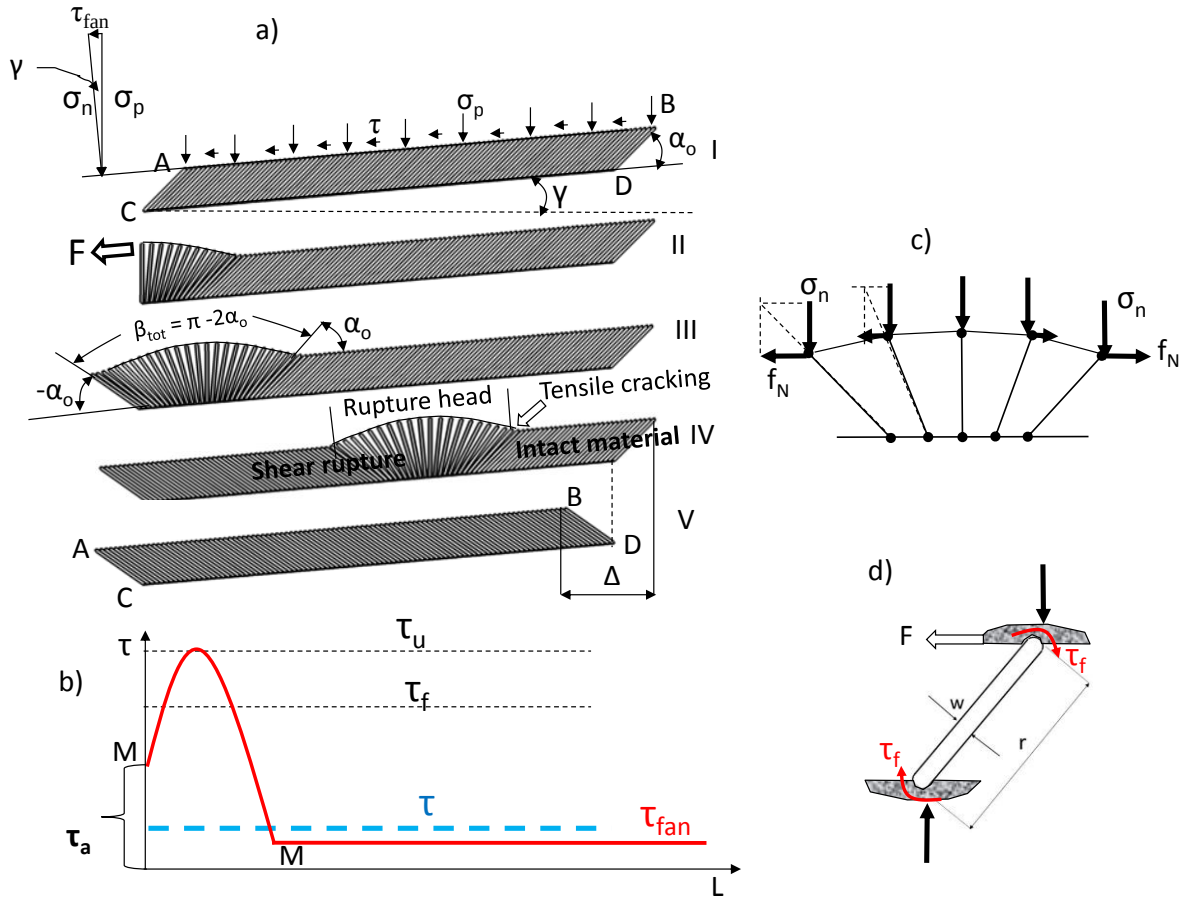

Figure 4 **(a) Different stages of the fan-structure formation and propagation illustrated by the physical model; (b) variation in shear resistance of the fan-structure at its initial formation and during propagation of the completed fan (red curve); (c) self-balancing conditions of the fan-structure; and, (d) illustration of friction between rotating domino-blocks and rupture faces**

Figure 4(a-V) shows the final stage at which the top face AB is moved against the bottom face CD by distance Δ due to the rotation of the domino-blocks on angle $\beta_{tot} = 180° - 2\alpha_0$. To move these surfaces with simultaneous creation of inter-block tensile cracks between all domino-blocks by rotation of all domino-blocks together, shear stress equal to the material strength τ_u should be applied. It should be noted that, at the final stage, the fault structure is represented by domino-blocks separated by tensile cracks similar to the structure of natural faults (Ortlepp shears) shown in photographs in Figure 2(e).

The physical model demonstrates that the same shear displacement Δ can be provided by the fan-mechanism at shear stresses τ significantly below the frictional strength. Horizontal lines in Figure 4(b) indicate levels of different stresses including the material strength τ_u, frictional strength τ_f, shear resistance of the fan-structure τ_{fan} (red line) and a low level of uniform stress τ (blue line) at which the fan-mechanism can provide relative shear displacement of AB and CD faces.

For the physical model, the easiest way to apply shear stress τ uniformly distributed along the entire model is the inclination of the model by an angle γ. The distributed weight, σ_p in this case, creates a shear stress $\tau = \sigma_p \sin(\gamma)$ and normal stress $\sigma_n = \sigma_p \cos(\gamma)$ along the model. By changing the angle γ, we can vary the applied stresses. It should be emphasised that for the initial formation of the fan-structure a local shear displacement should be organised. In the physical model the initial fan-structure is generated by application of force F to the first domino block. When the local stress applied reaches a level τ_a the front block will be torn off from the intact row, indicating the start of the tensile cracking process. The applied force is transmitted to the following blocks by elastically stretching the top rupture face (elastic connector), thereby causing the consecutive separation of the blocks and their rotation against the rupture faces. The fan formation is completed when the first block rotates to a total angle $\beta_{tot} = 180° - 2\alpha_0$ at a shear displacement Δ of the upper face.

The red graph MM in Figure 4(b) reflects the experimentally determined variation in shear resistance of the developing fan-structure during its formation and further propagation of the completed fan. The rising resistance up to τ_u is associated with the formation of the first half of the fan while the decreasing resistance corresponds to the second half formation. The reason for this is the fact that the distributed normal stress σ_n creates elementary forces f_N applied to domino-blocks, which are directed in opposite directions on two halves of the fan as shown in Figure 4(c). These forces are neutralised by horizontal components of elastic forces generated in the stretched elastic connector. The completed fan represents the self-balancing structure in unstable equilibrium.

Due to the existence of uniform shear stress $\tau > \tau_{fan}$ the fan-structure becomes self-unbalancing and propagates as a wave along the model. In this case the propagating fan represents the rupture head. Shear resistance of the propagating fan-structure τ_{fan} is determined by: 1) the reduced resistance associated with tearing off each front domino-block from the intact row; and, 2) friction in contacts of rotating domino-blocks with the rupture faces. A schematic illustration of frictional resistance of rotating domino-block is shown in Figure 4(d). Experiments on the physical model show that the minimum angle γ at which the fan becomes self-unbalancing (unstable) and provides spontaneous rupture development is about 4°. The static frictional strength for this model is characterised by $\gamma \approx 40°$.

Hence, results obtained on the physical model clearly demonstrate that shear resistance of the fan-structure τ_{fan} can be significantly less than frictional strength. For this particular model, shear resistance (strength) of the fan-structure τ_{fan} is by the factor of ten less than the frictional strength: $\tau_{fan} \approx 0.1\tau_f$. It should be emphasised that the low shear resistance takes place within the zone of the moving fan-head only. In front of the fan the material is in an intact condition. Behind the fan shear resistance is equal to friction. The fan-like rupture head propagating as a wave along the physical model at low angle γ is demonstrated in Tarasov (2016b).

3.2 Mathematical model

This section introduces briefly the mathematical model of the fan-mechanism. More detailed information can be seen in Tarasov and Guzev (2013) and in Tarasov (2014). Figure 5 shows different stages of the fan-structure formation. Figure 5(a) represents the potential fault in the initial condition. All domino-blocks here are represented by beams of length r, inclined at the initial angle α_0 and distanced from each other by s. The distance $s = w/\sin\alpha_0$, where w is the block width. Both ends of each beam are connected to the upper and lower faces. For ease, we assume that the upper face is represented by an elastic material while the lower face and the beams (domino-blocks) are stiff. Evenly distributed normal σ_n and shear τ stresses are applied to this construction. The value of τ is less than the shear stress necessary for displacement of the upper layer against the lower. Each beam is loaded by the same elementary normal force, N, and elementary shear force, f_τ, representing the evenly distributed normal σ_n and shear τ stresses applied to the whole structure. Elementary forces N and their horizontal components f_N in Figures 5(b)–5(e) are shown by black arrows whilst elementary shear forces f_τ are shown by red arrows. The meaning of the elementary forces is as follows: $N = \sigma_n s \cdot 1$; $f_\tau = \tau s \cdot 1$, where depth (or thickness) of the model is equal to unity (1). As such, a version of the model with blocks bonded together can be treated as representing the intact material.

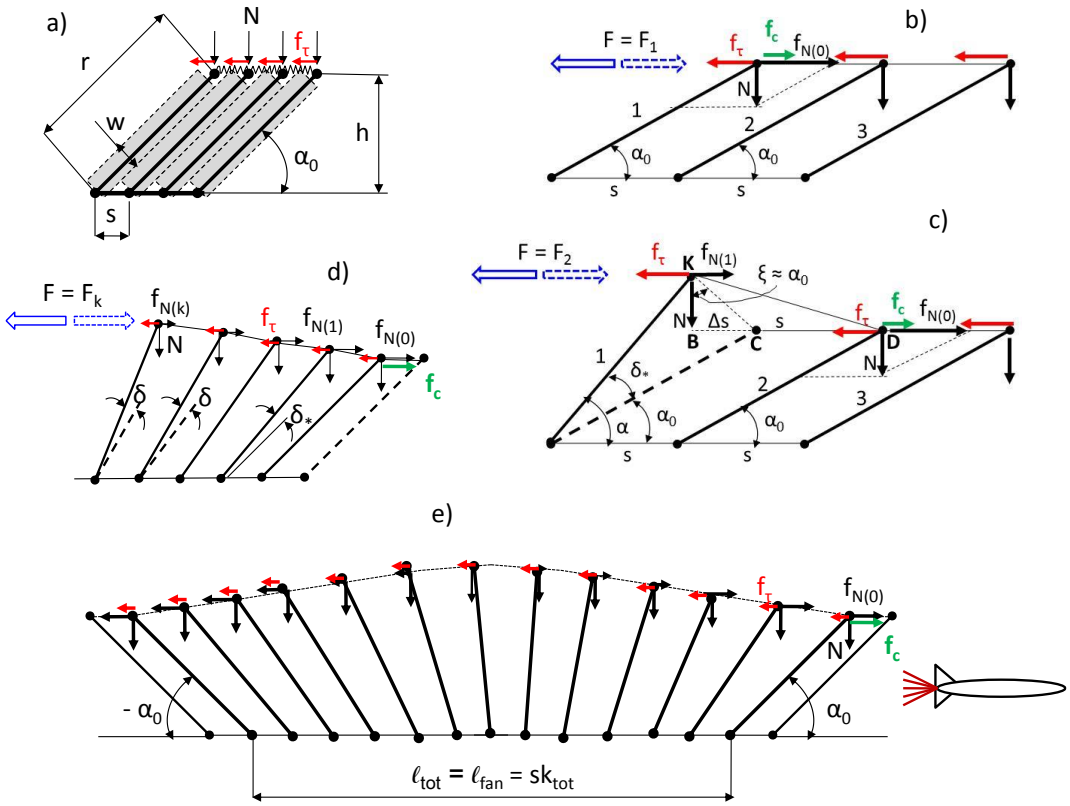

Figure 5 Mathematical model of the fan-structure formation from domino-blocks. a) A row of inclined domino-blocks (beams) representing an implicit structure of the future fault loaded by elementary forces; and, (b)–(e) interaction between activated beams during the fan formation

The fan-structure can be formed if, in addition to the existing evenly distributed stresses, a local supplementary force (or stress) is applied. We will illustrate the main principals of interaction between the blocks at the fan-structure formation on the first three beams shown in Figures 5(b) and 5(c). Let us apply a supplementary horizontal force F to the upper end of beam-1. Beam-1 will be torn off from beam-2 and start rotating against the lower and upper rupture faces when the applied force F reaches the critical level F* (see Equation (1)) equal to the resistance provided by internal horizontal forces $f_{N(0)}$, f_τ and f_c. Here, $f_{N(0)} = N/tg\alpha_o$ is the horizontal resistance caused by the normal force N at $\alpha = \alpha_0$ (this value is the same for any beam at the initial position); f_c (green arrow) is the reduced resistance of tearing off beam-1 from beam-2, which are bonded together. This value is the same for any beam that is being torn off. At this stage of the discussion we consider friction in contact areas between the beam ends and rupture faces as being equal to zero. Later, friction in these areas will be estimated and taken into account.

$$F^* = F_1 = f_{N(0)} + f_c - f_\tau \tag{1}$$

At the precise moment when beam-1 has been torn off from beam-2 the total resistance decreases by the value f_c:

$$F = F'_1 = f_{N(0)} - f_\tau \tag{2}$$

A further increase of the applied force *F* will lead to the further rotation of beam-1 (see Figure 4(c)) causing the stretch of the fragment of the upper elastic connector located between beam-1 and beam-2 (DC = *s* is the initial and DK is a new length of the elastic connector). The stretching of the elastic connector will be accompanied by an increasing force transmitted from beam-1 to beam-2. The transmission of forces from one beam to another (by stretching the elastic connector representing the fracture face) is the key feature of the fan-mechanism. Beam-2 will then be torn off from beam-3 when the applied force *F* reaches the value F_2:

$$F = F_2 = f_{N(0)} + \frac{N}{tg(\alpha_0+\delta_*)} + f_c - 2f_\tau \tag{3}$$

Here, $Ntg(\alpha_0 + \delta_*)$ is the horizontal resistance of beam-1 caused by force *N* when $\alpha = (\alpha_0 + \delta_*)$. We will call angle δ_* a 'detachment angle' because any previous beam must be rotated on this angle to tear off the front beam. The critical force *F** required to tear off the front beam described by Equation (1) is equal to force F_c generated by the stretched elastic connector DK. Taking into account that angle δ_* is very small, we can suppose that $\xi \approx \alpha_0$ (see Figure 5(c)). In this case we will have:

$$F_c = EA\frac{\Delta s}{s} = EA(^r/_S)\delta_* sin\alpha_0 \quad (4)$$

where: *E* = the modulus of elasticity of the elastic connector; *A* = the cross-sectional area of the elastic connector; *r* = the beam length; *s* = initial length of the elastic connector between the neighbouring beams.

It is because *F** = F_c from Equations (1) and (4) we can determine δ_*:

$$\delta_* = \frac{Nctg\alpha_0}{EA(r/s)sin\alpha_0} + \frac{f_c - f_\tau}{EA(r/s)sin\alpha_0} \quad (5)$$

At the moment when beam-2 has been torn off from beam-3 the shear resistance F_2 described by Equation (3) decreases by the value f_c:

$$F = F'_2 = f_{N(0)} + \frac{N}{tg(\alpha_0 + \delta_*)} - 2f_\tau \quad (6)$$

The decrease of the resistance by the value f_c accompanies each tearing off act for all sequentially activated beams. These acts cause the release of some portion of elastic energy and can be treated as acts of acoustic emission observed at shear rupture development in intact and pre-cut specimen.

The physical model discussed previously shows that angle δ between any two neighbouring beams is variable along the fan-head. For ease, at this stage of the mathematical model development we will consider angle δ_* (Equation (5)) as the average angle δ between all beams involved in the fan. In this case the resistance of k activated beams F_k in Figure 5(d) is determined by Equation (7):

$$F = F_k = \frac{N}{\delta} ln \left|\frac{\sin(\alpha_0 + k\delta)}{\sin(\alpha_0)}\right| + f_c - kf_\tau \quad (7)$$

An essentially important feature of the fan-structure is the fact that the resistance f_N = N/tgα (see Figure 5(d)) of each beam decreases with increasing angle α from α_0. It reaches zero at α = 90° and becomes negative at $\alpha > 90°$. It means that the formation of the first half of the fan-structure is accompanied by the increase in shear resistance F; it reaches its maximum when half of the fan has completed and then decreases down to zero. Such variation in shear resistance is in accordance with red graph MM in Figure 4(b). For the completed fan shear resistance of relative displacement of the rupture faces separated by the fan-structure is determined by the sum of all horizontal forces applied to all beams involved in the completed fan, which is represented by Equation (8). The completed fan with elementary forces applied to all beams is shown in Figure 5(e).

$$F_{k(tot)} = \frac{N}{\delta} ln \left|\frac{\sin(\alpha_0 + k_{tot}\delta)}{\sin(\alpha_0)}\right| + f_c - f_\tau k_{tot} \quad (8)$$

Analysis of Equation (8) shows that at the absence of distributed shear stress, the completed fan represents a self-balancing structure. The first member of Equation (8) in this case is equal to zero because forces f_N affecting each beam of the symmetrical fan are directed in opposite directions against the centre of the fan-structure. These forces cause stretching of the elastic connector between the beams, which makes the fan-structure self-balancing. Equation (8) shows that, at the presence of distributed shear stress (represented in the equation by f_τ), the fan-structure becomes self-unbalancing. It means that the fan can propagate along the intact model driven by distributed shear stress.

The second member of Equation (8) reflects the reduced resistance f_c of tearing off the front beam (domino-block) from the intact material. The elementary force f_c (green in Figure 5) is applied to the front beam only. It will be shown that the contribution of f_c to the total resistance of the fan-structure in real materials is negligibly small. The third member of Equation (8) represents an active united force assisting displacement. It is caused by the evenly distributed shear stress τ applied to the material. Unlike f_c the elementary forces f_τ (red) are applied to all k_{tot} beams of the fan-structure.

Due to this, the separation of each front domino-block with the reduced resistance f_c (green arrow) from the intact material is caused by the united active force $k_{tot}f_\tau$, where k_{tot} is the total number of domino-blocks in the fan-head. Estimations made in Tarasov (2014) show that the fan-structure in natural materials can incorporate thousands of domino-blocks. It means that separation of the front domino-block from the intact material can be caused by very low shear stress applied $f_\tau = f_c/k_{tot}$. Hence, the contribution of f_c to shear resistance of the fan-structure is negligible. It means that for real materials the fan-structure resistance is mainly determined by friction in contact areas between rotating blocks and the fracture faces. Shear resistance of the fan-structure τ_{fan} represents the shear resistance to displacement of the rupture faces relative to each other in the rupture head. Due to the fact that domino-blocks in the fan-structure operate as hinges frictional shear resistance between the rupture surfaces separated by the fan-structure is significantly less than the conventional frictional resistance τ_f between fault surfaces in the absence of the fan-structure. Equation (9) from Tarasov and Guzev (2013) demonstrates that the fan-structure resistance to shear τ_{fan} depends on the block geometry characterised by w/r:

$$\tau_{fan} \approx \tau_f \frac{w}{r} \tag{9}$$

where: τ_f is the sliding friction; w is the width and r is the length of domino-blocks (see Figures 4(d) and 5(a)).

At the block geometry characterised by w/r = 0.1 shear resistance (strength) of the fan-structure τ_{fan} is by the factor of ten less than the frictional strength: $\tau_{fan} \approx 0.1\tau_f$. This result is consistent with the previously discussed result for the physical model. Thus, the fan-structure represents a mechanical system that creates significant strength weakening in the rupture head observed in ruptures of extreme dynamics.

4 Unique features of the fan-mechanism in extreme ruptures with pre-existing interfaces

The fan-mechanism has a number of unique features observed in laboratory experiments at study extreme shear ruptures. These features are listed below and discussed in more detail together with experimental observations in the following sections:

- Dramatic strength weakening and high slip velocity in the rupture head.
- Shear stress intensification and source of power of extreme ruptures.
- Pulse-like and crack-like rupture modes.
- Tensile stress generation and off-fault tensile cracking process.
- Conditions of spontaneous rupture propagation.
- Supershear rupture velocity.

4.1 Dramatic strength weakening in the head of extreme ruptures

4.1.1 Theoretical analysis based on fan-mechanism theory

This section analyses the variation in shear resistance, slip and fault structure along the fault governed by the fan-mechanism. Figure 6 (a) shows a fragment of the physical model where the fan-structure representing the rupture head propagates from left to right. The red vertical line indicates the boundary between the intact material in front of the rupture tip (all domino-blocks here are glued together) and the cracked material representing the fault structure behind the rupture tip (all domino-blocks are separated by tensile cracks). The fan-mechanism suggests that immediately behind the rupture tip (zone I) the density of material located between the rupture faces should decrease significantly due to tearing off the front domino-block from the intact base. Figure 6(b) shows a schematic of the variation in shear resistance in front of the fan-structure, in the fan zone and behind the fan. In front of the fan, shear resistance corresponds to the material strength τ_u. Within the fan zone shear resistance decreases sharply with a

minimum resistance in the centre part of the fan where domino-blocks are oriented normally to the rupture plane. Behind the fan, shear resistance can correspond to static τ_{fs} or dynamic τ_{fd} frictional strength depending on the level of shear stress applied (discussed in more detail in Section 4.2.2). Figure 6(c) illustrates that high interface slip should take place within the fan zone II. Behind the fan the interface slip should significantly decrease or completely stop depending on loading conditions (discussed in more detail in Section 4.2.2).

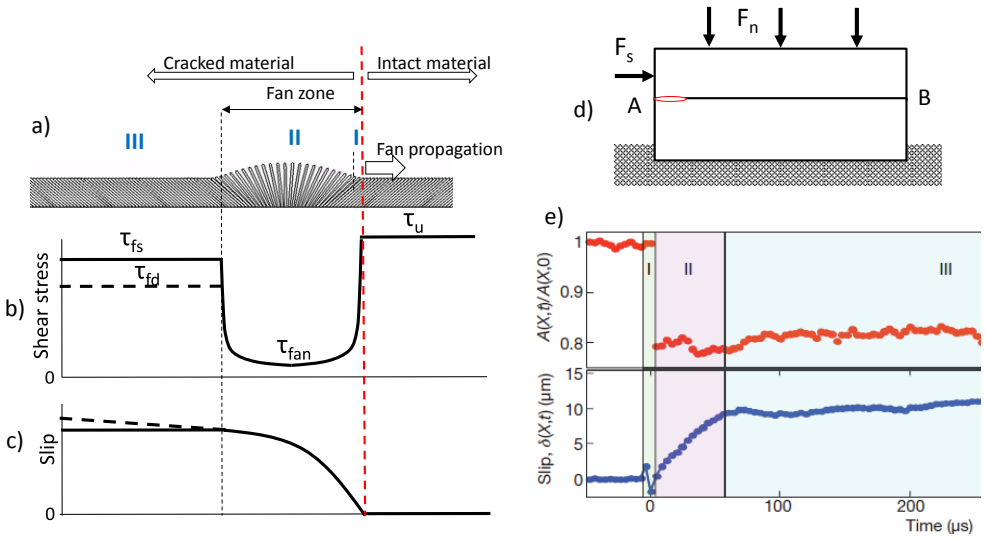

Figure 6 Explanation on the basis of the fan-mechanism the evolution of contact area A(t), interface slip δ(t) and strength weakening in the rupture head observed in extreme ruptures

4.1.2 Experimental investigation

The combination of such features as intensive microcracking, interface slip and strength weakening in the head of extreme ruptures has been observed in different experiments (e.g. Ohnaka & Kuwahara 1990; Ohnaka & Shen 1999; Lei et al. 2000; Samudrala et al. 2002; Rubinstein et al. 2004; Lykotrafitis et al. 2006; Griffith et al. 2009; Ben-David et al. 2010; Lu et al. 2010; Ghaffari et al. 2014). In this section, we will discuss experimental results that provide the most detailed information about these features (Rubinstein et al. 2004; Ben-David et al. 2010). The specimen type used in these experiments is shown in Figure 6(d) consisted of two blocks made from transparent brittle polymethyl methacrylate (PMMA) with a very thin carefully prepared frictional interface AB. These blocks were initially pressed together with a constant normal force F_n resulting in a uniform distributed stress on interface AB. At application of force F_s to the upper block's 'trailing' edge shear resistance along the interface is provided by friction caused by asperities contacts. At a certain level of force F_s an extreme shear rupture is generated and propagates spontaneously along the interface from point A towards point B. The rupture head is shown as red ellipse.

Experiments provided continuous measurements of the concurrent local evolution of the real contact area (associated with fracturing of the asperity contacts) and the corresponding interface slip at the rupture front propagation. The real contact area was measured by illuminating the interface area with a laser sheet imaged by a fast camera. These measurements provide an inclusive picture of processes that occur within frictional slip. Four distinct phases of evolution were identified. We will discuss here the first three phases because phase IV is related to the contact rejuvenation and strengthening due to the 'ageing' process after the rupture propagation.

Figure 6(e) shows results of simultaneous measurements of the local dynamics of contact area A(t) and slip δ(t) before, during and after the passage of the rupture front. According to the graph (top panel of Figure 6(e)) the entire net reduction of A(t) equal to 20 per cent occurs in phase I, immediately upon the passage of the rupture front. The reduction of A(t) is caused by a contact of asperities fracture, which takes place within the short (about a microsecond) passage of time. Phase II is characterised by high slip (bottom panel of Figure 6(e)) and slip velocities with variations of A(t) that are an order of magnitude smaller than

those in phase I. The duration of this phase is about 60 μs. Phase III is characterised by a significant decrease in the slip velocity. It should be noted that direct measurements of shear resistance (friction) within the sliding rupture head is impossible today. However, high slip velocities within the rupture head measured in experiments clearly indicate dramatic weakening of friction in this zone (will be illustrated by experimental results later).

The combination of observed features such as tensile-cracking process in the rupture tip, three phases of variation in the interface slip and in the contact area, and high slip velocity within the rupture head indicating very low friction are in accord with the fan-mechanism features discussed in Figures 6(a)–6(c). In contrast with the fan-model, the explanation for the observed features proposed in Ben-David et al. (2010) is based on the traditional approach associated with thermal effect. It is supposed that the strength weakening is caused by fracture-generated heat at phase I. The heat released by this rapid irreversible deformation is deposited along the interface layer before the net slip. Such a rapid heat injection will cause an 'immediate' large temperature increase ΔT within the thin interface layer. Any increase beyond the glass temperature Tg (~ 110°C) will cause significant shear strength weakening until the heat generated by fractures diffuses away from the interface region. After that phase III is followed. However, it should be emphasised that the measurement of high temperatures generated by the fracture process in the tip of extreme shear ruptures has never been conducted in a laboratory. At the same time, some field observations indicate relatively low heat flow in the vicinity of the most active faults (Brune et al. 1969; Lachenbruch 1980; Richards 1976).

4.2 Shear stress intensification and source of power of extreme ruptures

4.2.1 Principles of shear stress intensification in the fan-mechanism model/theory

Figure 7 illustrates principles of shear stress intensification caused by the fan-mechanism. Figure 7(a) shows the fan-structure propagating from left to right. Distributed shear stress τ is applied to the whole fault. All domino-blocks are loaded by elementary forces f_τ. In front of the fan-structure, domino-blocks are bonded together and represent the intact material. Small elementary forces f_τ here cannot separate and rotate domino-blocks. Behind the fan, domino-blocks completed their rotation form very compact structure. Here rotation of blocks under the effect of forces f_τ is also impossible. However, within the fan-structure zone domino-blocks are separated. Due to this, elementary forces f_τ applied to each block cause corresponding rotation of them and stretch the elastic connector (i.e. the upper rupture face) in front of each block, thus transmitting their forces to the rupture tip. This principle is illustrated in Figure 7(b). In this case, real forces affecting domino-blocks within the fan-structure zone increase from the back of the zone towards the front. The maximum force $F_{tot} \approx f_\tau k_{tot}$ (see Equation (8)) is applied to the front domino-block. Here, k_{tot} is the number of domino-blocks involved in the fan-structure. Such distribution of forces makes the fan-structure asymmetrical, as shown in Figure 7. A graph in Figure 7(a) demonstrates the general character of shear stress distribution along the fault involving the fan-structure. In the model, τ_o is the initial distributed shear stress applied and τ_1 is the stress behind the fan, yielding a static stress drop $\Delta\tau = \tau_o - \tau_1$. The part of the graph NN reflects the stress distribution within the rupture head, while the part Nn is in front of the rupture tip. High stresses in both zones are generated by the fan-mechanism.

Estimations made in Tarasov (2014) show that the fan-structure in natural materials can incorporate thousands of domino-blocks. It means that potential capacity of the fan-mechanism for stress intensification is huge. However, despite very high capacity the actual magnitude of stresses generated in the rupture tip is restricted by shear resistance of front domino-blocks to tearing off from the intact material. This means that shear stress in the rupture tip corresponds to the material strength τ_u when the rupture propagates in the intact material or to frictional strength τ_f when the rupture propagates along the frictional interface. At the same time, due to high difference between the material strength and potential stress capacity of the fan-mechanism the rupture propagates easily and can reach extreme velocities. It should be noted that, due to the asymmetrical shape of the fan-structure during its propagation, normal stresses applied to the fan-structure create an additional driving force F_{ad} as illustrated in Figure 7(c).

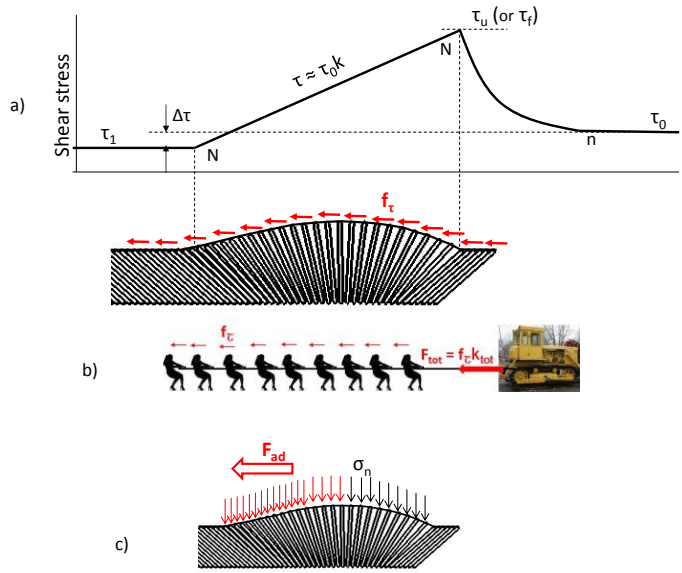

Figure 7 Principles of shear stress intensification caused by the fan-mechanism

4.2.2 Fan-mechanism model applied to experimental results of extreme ruptures with pulse-like and crack-like modes

Natural and laboratory observations show that extreme ruptures can propagate as either self-healing slip pulses (pulse-like mode), where the fault relocks shortly behind the rupture front, or sliding cracks (crack-like mode), where a large section of the interface slides behind a fast-moving rupture front (e.g. Heaton 1990; Lykotrafitis et al. 2006; Lu et al. 2010). Figure 8 shows some experimental results obtained by Lu et al. (2007, 2010) at study of extreme ruptures with the pulse-like and crack-like modes. The study was conducted on specimens made from a brittle resin homalite. The homolite is a photo-elastic material which allows capturing the stress field caused by the propagating rupture tip because of its ability to visualise generated shear shock waves. Figure 8(a) represents the specimen configuration and loading conditions. The inclined frictional interface AB was prestressed in compression and in shear due to application of vertical force P. The level of shear prestress in some experiments was about 40 per cent of the static frictional strength $\tau_o \approx 0.4\ \tau_{fs}$. After that rupture was initiated in the simulated fault by producing a local pressure pulse in a small area of the interface. In experiments the following parameters were measured: velocities of shear and compression elastic waves, rupture velocity, interface slip and slip velocity.

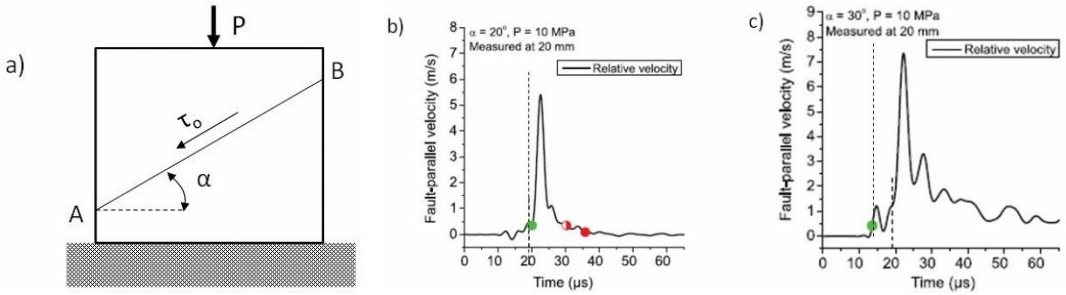

Figure 8 (a) Configuration and loading conditions of homalite specimens used for study of the pulse-like and crack-like rupture modes (Lu et al. 2007, 2010); and, (b), (c) slip velocity variation with time in a certain point of the interface during the rupture propagation for two specimens indicating the pulse-like and crack like rupture modes (Lu et al. 2007)

Figures 8(b) and 8(c) show the variation of slip velocity with time in a certain point of the interface during the rupture propagation. The curves obtained for different specimens subjected to different pre-stress conditions. The curve in Figure 8(b) illustrates the pulse-like rupture mode. Here, the green dot indicates the moment at which the rupture front (tip) crosses the point and initiates the interface slip. The red dot

indicates the moment of interface locking behind the rupture head. The curve in Figure 8(c) corresponds to the crack-like rupture mode. Here there is no interface locking within the time observation. Both curves show that behind the rupture tip (green dots) slip velocity increases, reaches a maximum and then decreases. Lu et al. (2007, 2010) revealed that different rupture modes (pulse-like and crack-like) can be selected by the level of fault prestress and demonstrate that both rupture modes can transition to intersonic speeds.

Today, the generally accepted explanation for the pulse-like rupture mode is based on the strong velocity-weakening friction law. According to this hypothetical law the fault strength is inversely proportional to the slip velocity (Heaton 1990; Cochard & Madariage 1994; Zheng & Rice 1998). Figure 9(a) shows an idealised model of a self-healing rupture pulse propagating from left to right at a velocity of V_r (Heaton 1990). Three panels here illustrate variations in the interface slip, slip velocity, stress and fault strength along the fault. Shear stresses applied to the fault are: τ_o is the stress before the initiation of rupture and τ_1 is the final stress after rupture has terminated, yielding a static stress drop $\Delta\sigma = \tau_o - \tau_1$. The applied shear stress τ_o is significantly less than the static frictional strength τ_s. In the region ahead of the rupture, the shear stress τ_{zy} is assumed to be given by crack theory. Fracture initiates when the stress at the rupture tip exceeds the static strength of the fault τ_s and then drops to a sliding frictional level that is inversely proportional to the slip velocity. Slip velocities are high and sliding friction is very low near the rupture front. As the slip velocity decreases away from the rupture front, the sliding friction increases and the fault heals itself. After that the strength of the fault returns to high level τ_s.

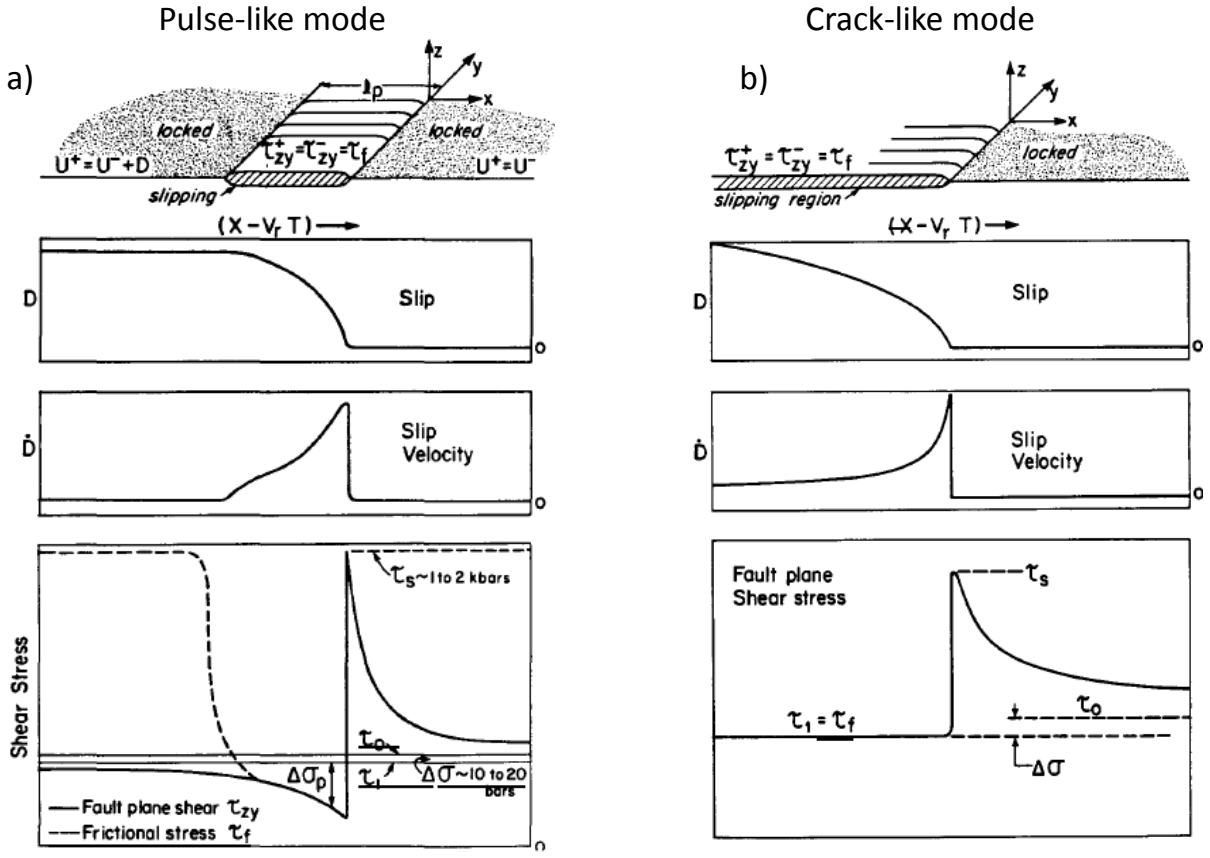

Figure 9 Models of the pulse-like and crack-like rupture modes from Heaton (1990)

This model has the following unresolved problems:

1. The assumption that friction is inversely proportional to the slip velocity can explain the corresponding variation of friction in response to a specific variation of slip velocity. However, the model does not involve a mechanism that determines the specific variation of slip velocity as shown in Figure 9(a).

2. There is no explanation for dramatic increase in slip velocity in the rupture tip where the initial friction is high and equal to the static friction τ_s.
3. The model does not include the source of energy that can provide extreme rupture velocities up to intersonic levels observed in experiments.
4. This model cannot explain the reason for transition from the pulse-like mode to the crack-like mode with increasing the level of fault prestress as observed in experiments by Lu et al. (2007, 2010).

Figure 9(b) shows an idealised model of a rupture propagating with the crack-like mode described by Kostrov (1966) (figure from Heaton 1990). In this model another velocity weakening principle is accepted. After the fracture initiation the static strength of the fault τ_s drops sharply down to the constant dynamic friction $\tau_f = \tau_1$. Experimental studies of rock friction indicate that the coefficient of dynamic friction for a sliding surface is within several percent of the static coefficient of friction (Dieterich 1979). According to this model the rupture continues to grow and does not heal until information is received that the rupture front has stopped propagating.

This model has the following shortcomings.

1. It does not have a potential for transition from the crack-like mode to the pulse-like mode with variation in the prestress level.
2. The model does not include the source of energy that can provide extreme rupture velocities up to intersonic levels observed in experiments.

The fan-mechanism theory can resolve the discussed problems. Figure 10 shows two models of extreme ruptures propagating with the pulse-like and crack-like modes governed by the fan-mechanism. The models take into account two fundamental and very important features of the fan-structure: extremely low shear resistance (independent on slip velocities) and high intensification of reduced stresses. The relative variation of shear resistance and shear stresses along the faults shown in Figure 10 determine corresponding behaviour of the interface slip and slip velocity.

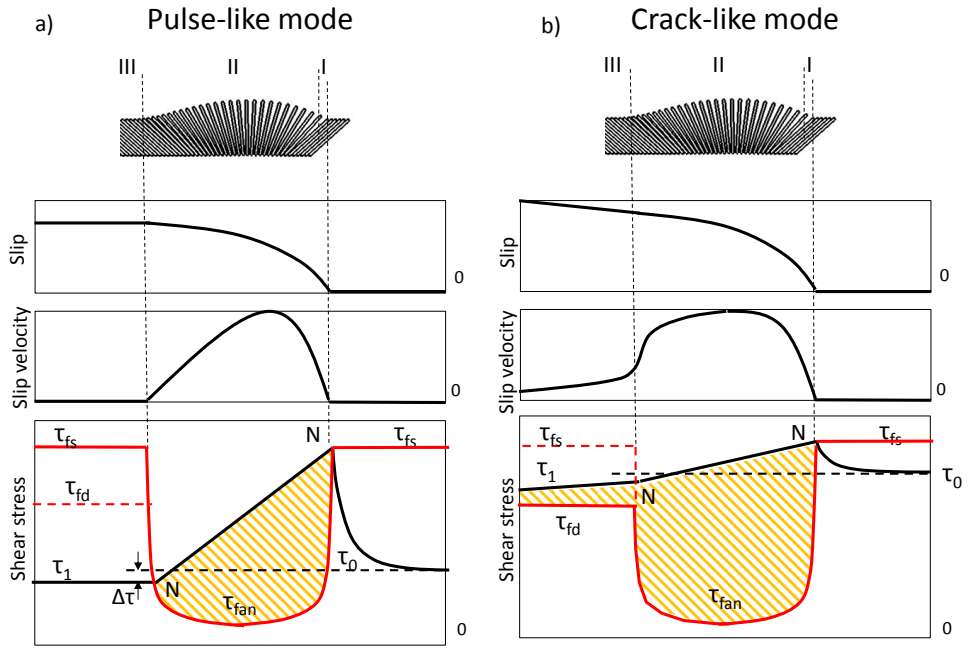

Figure 10 Models of the pulse-like and crack-like modes of extreme ruptures governed by the fan-mechanism

Let us discuss first the pulse-like mode in Figure 10(a). The red graph reflects the variation of fault frictional strength at shear rupture propagation governed by the fan-mechanism as discussed in Figure 6(b). The initial stress applied τ_o is significantly less than the static frictional strength τ_{fs}. The variation of stresses

generated by the fan-mechanism due to intensification of the applied stress τ_o (as discussed in Figure 7(a)) is shown by the black graph. Due to a large difference between the generated stresses and the fan strength in the rupture front, the slip velocity here accelerates sharply. With distance from the tip, the relative variation of stress (NN line) and fan strength (red curve) will cause initially further acceleration of the slip velocity up to a maximum level and then deceleration (similar to the experimental curve in Figure 8(b). At the end of the fan, when the applied stress and shear resistance are equalised, the fault heals itself. After that, the strength of the fault returns to a high level τ_{fs} determined by the static friction. It should be emphasised that the pulse-like mode takes place when the level of τ_1 is less than the level of dynamic friction τ_{fd} (red horizontal dotted line). Due to the interface locking behind the rupture head the level of τ_1 here is constant.

The yellow area on the graph represents the energy released through the fan-mechanism, which is responsible for the extreme rupture dynamics. The fan-mechanism is the self-sustaining source of energy accumulated in the moving rupture head. The higher the applied stress τ_o the greater the accumulated energy in the rupture head and the higher the rupture speed. It is important to note that an additional portion of the accumulated energy is derived from normal stresses affecting the fault, as discussed in Figure 7(c).

Figure 10(b) shows a model of extreme ruptures with the crack-like mode governed by the fan-mechanism. Unlike the pulse-like model, here stress τ_1 exceeds the dynamic frictional strength τ_{fd}. Due to this, slip will continue behind the fan indicating the crack-like rupture mode. The increase in the interface slip with distance from the rupture head should lead to the corresponding decrease in the level of τ_1. When $\tau_1 < \tau_{fd}$ the interface slip should stop. Generally, extreme ruptures of the crack-like mode involve larger energy in the rupture head compared with the pulse-like mode, which makes them faster. This is in agreement with experimental results obtained by Lu et al. (2007, 2010), which demonstrate that an increase in shear prestress (τ_o) causes a variation from pulse-like to crack-like modes. The experiments also show that both crack-like and pulse-like rupture modes can transition to supershear speeds, with pulse-like rupture modes having smaller supershear rupture speeds than crack-like modes.

4.3 Tensile stress generation

4.3.1 Principles of tensile stress generation in the fan-mechanism model/theory

The fan-structure formation and propagation is accompanied by an extension of the rupture face on one side of the fan-head. The photograph in Figure 11(a) shows the symmetrical fan-structure at self-balancing conditions created on the physical model. Values of angle δ between neighbouring domino-blocks within the fan-structure reflect tensile strains ε_t of elastic connectors between the domino-blocks and, consequently, tensile stresses σ_t in them. The graph in Figure 11(a) illustrates the character of distribution of $\sigma_t(\delta)$ along the symmetrical fan-structure. Maximum values of $\sigma_t(\delta)$ are located at the fan centre and tensile stresses decrease up to zero towards both fan ends.

When the fan-head propagates under the effect of distributed shear stress τ through the material, the shape of the fan-structure and distributions of δ, ε_t and σ_t along the fan becomes asymmetrical. The photograph in Figure 11(b) illustrates the shape of the fan-head propagating from left to right along the row of domino-blocks bonded together and representing intact material. A relatively large angle δ_0 in the fan front indicates corresponding high values of ε_t and σ_t. The high tensile stress is produced by the fan-structure, which at the presence of distributed shear stress represents a self-sustaining shear stress intensifier as discussed in Figure 7(a). Shear stresses increasing from the end to the front of the fan-structure provide corresponding stretch of the elastic connector (rupture face), which changes the overall distribution of tensile stresses along the fan-structure. The graph in Figure 11(b) illustrates a variation of $\sigma_t(\delta)$ along the propagating fan. The level of tensile stress in the rupture tip is restricted by the resistance to tearing off the front domino-block from the intact structure. We call this stress a detachment stress $\sigma_t = \sigma_{t(det)}$. The intensification of tensile stresses in the rupture tip by the fan-mechanism causes the fault propagation due to sequential (one-by-one) separation of the front blocks from the intact material. Figure 11(c) shows that, at bilateral rupture propagation, the fan-heads create an extension of rupture faces on opposite sides.

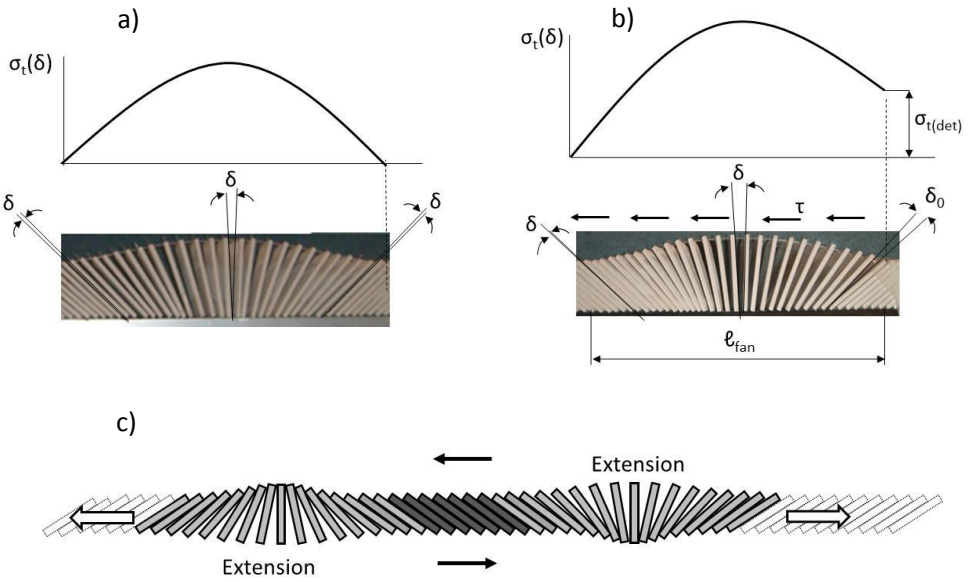

Figure 11 (a) Variation of tensile stresses generated in the rupture face by the self-balancing symmetrical fan-structure; and, (b) by self-unbalancing asymmetrical fan-structure. (c) Location of extension zones on opposite sides of the interface created by two bilaterally propagating fan-structures

4.3.2 Fan-mechanism model applied to experimental results of showing off-fault tensile cracking under extreme dynamics

In laboratory experiments on pre-cut homalite specimens with bonded interfaces, it was observed that spontaneous shear ruptures can create an array of secondary tensile microcracks in the bulk material adjacent to the interface (Samudrala et al. 2002; Griffith et al. 2009; Ngo et al. 2012). Homalite is a brittle photo-elastic resin. Two types of specimens and loading conditions were used in the experiments as illustrated in Figures 12(a) and 12(b). The bonding process provided the constitutive properties of adhesive bond close to that of the bulk material, however, the rupture strength of the bond line was kept lower than the constituent pieces. Therefore, the bond represented a thin layer (less than 30 μm) of brittle solid material between two stronger interfaces.

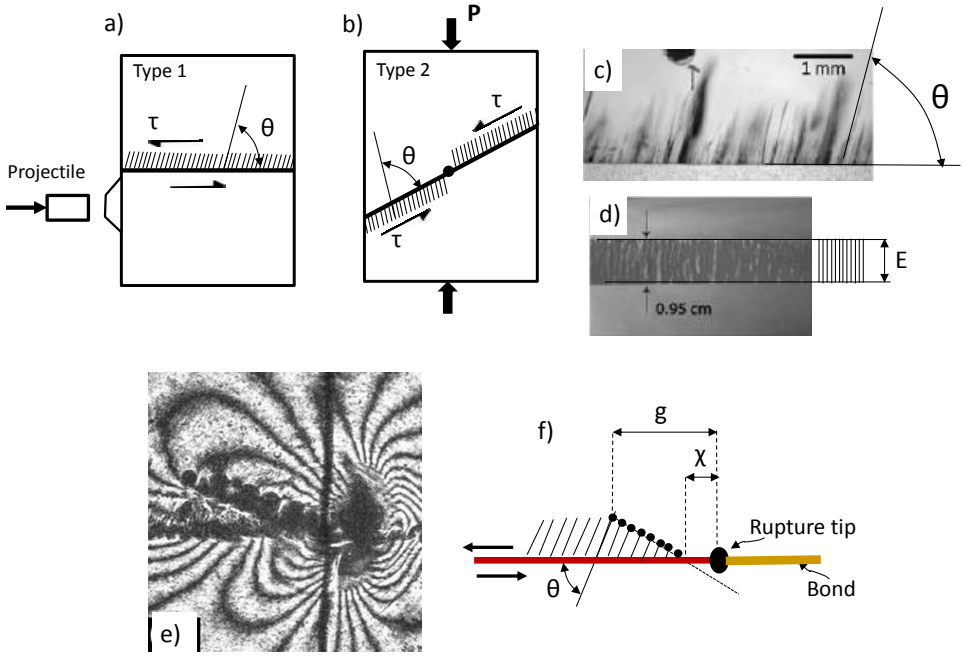

Figure 12 Specimen configurations and experimental results illustrating features of the off-fault tensile cracking process in photo-elastic specimens with bonded interfaces

In experiments with the horizontal interface (entirely free of normal compressive pre-stress), a horizontal impact-loading was utilised (Figure 12(a)). The stress waves resulting from the impact, produced by a projectile, generated dynamic rupture moving along the interface. In experiments with the inclined interface, the specimen was subjected to static uniaxial pre-compression with the creation of normal and shear pre-stress in the interface (Figure 12(b)). After that, a local pressure pulse in a small area of the interface was produced. The local pressure pulse nucleated spontaneous shear ruptures, propagating bilaterally. The dynamic stress field produced by spontaneously propagating shear rupture in the photo-elastic material for both types of tests was recorded by high-speed photography. For both types of specimens, an array of secondary tensile microcracks that formed adjacent to the rupture interface was observed. Arrays of tensile cracks being generated along the interface for both types of specimens are shown schematically in Figures 12(a) and 12(b). Dynamically propagated rupture heads created arrays of tensile cracks on one side of the rupture interface. In the case of bilateral rupture propagation, tensile cracks were created in different blocks of the specimen.

Photographs in Figure 12 illustrate some features of tensile cracks. Figure 12(c) shows that microcracks are parallel to each other, steeply inclined to the fault path ($\theta \approx 80°$) and some curved slightly as they propagated into the sample. Figure 12(d) shows the top view of the interface and indicates that microcracks extend across the specimen thickness E. The frequency of short microcracks adjoining to the interface is very high. Longer microcracks are interspersed with shorter microcracks. Figures 12(e) and 13(f) show a typical photo-elastic image and a graphical schema illustrating features of the initiation, propagation, and arrest of the off-fault tensile cracks along the head of shear rupture. The large shadow spot here corresponds to the main shear rupture tip. A series of small shadow spots mark the locations of the tips of the growing mode-I microcracks as they propagate a finite distance into the specimen. The analysis of images shows that tensile cracks nucleate at some distance X behind the rupture tip. The tensile cracks grow with distance from the shear fracture tip. At a certain distance g from the rupture tip the microcracks stop growing; behind this zone static microcracks are left in the wake of the propagating rupture.

All features associated with the off-fault cracking process discussed above can be explained by the fan-mechanism model. The model in Figure 13(b) shows a fan-head propagating along the bond line from left to right. The driving shear stress is applied to the fan-structure from the face material. The graph in Figure 13(a) shows the variation of tensile stress σ_t generated by the fan-head in the face material (similar to that discussed in Figure 11(b)). At the rupture tip, the level of tensile stress $\sigma_{t(bond)} = \sigma_{t(det)}$ is determined by the resistance of the bond material to tearing off the front domino-blocks from the intact bond (reduced tensile strength of the bond). Behind the tip, the level of tensile stress increases with distance from the tip. It is important to note that the maximum tensile stress generated between each pair of domino-blocks acts in a direction perpendicular to the plane located between these domino-blocks. Open arrows in the model illustrate this for three pairs of domino-blocks. This fact determines the orientation of generated tensile cracks.

At the rupture tip the maximum tensile stress $\sigma_{t(bond)}$ is oriented at angle α_0. Between points 1 and 2 on the graph the level of tensile stress is below the tensile strength of the bulk material and tensile cracks cannot propagate in the bulk material. At distance X from the tip, the level of tensile stress reaches the strength of the bulk material $\sigma_{t(bulk)}$ (point 2 on the graph) nucleating a secondary tensile crack oriented along the domino-block at angle θ. This crack grows with propagation of the fan-head until the zone of maximum tensile stress $\sigma_{t(max)}$, which is created by the head, has reached this point. Due to rotation of the stress field generated by the rotating domino-blocks, the growing crack slightly alters its orientation approaching the vertical direction as observed in the homalite experiments. After the point of the fan-head characterised by $\sigma_{t(max)}$ has passed the growing crack, the crack growth stops due to the decrease in tensile stresses in the second half of the fan-structure.

It is important to note that the off-fault tensile cracking was observed in experiments with the coherent (bonded) interface (Samudrala et al. 2002; Griffith et al. 2009; Ngo et al. 2012) and was not observed for the frictional interface (Xia et al. 2004; Lykotrafitis et al. 2006). The explanation for this feature is as follows. For the bonded interface shown in Figure 13(b) the tensile cracks and domino-blocks involved in the fan extend across the whole bond layer equal to the specimen thickness E and produce corresponding

stresses and tensile cracks in the bulk material. This fact is confirmed by the photograph in Figure 12(d) that shows the top view of the interface of the homalite specimen. In the frictional interface, the fan-structure involves domino-blocks formed on the basis of 'welded' asperities as illustrated in Figures 13(e) and 13(f). Due to this, tensile stresses generated in the bulk material by the fan-structure are concentrated in small areas of asperities characterised by the dimension e in Figure 13(f). These stresses are too small to cause off-fault tensile cracks across the whole interface thickness E.

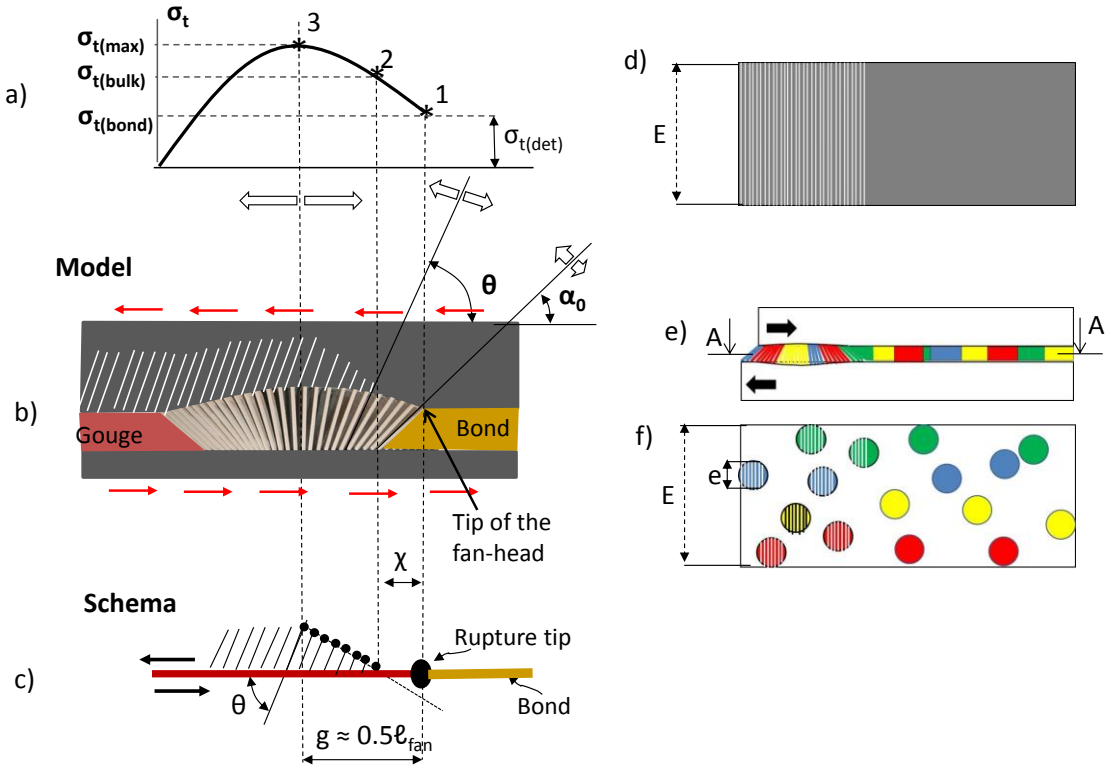

Figure 13 Schema for the off-fault cracking process generated by the fan-mechanism. (a) Tensile stress σ_t variation in the upper face along the fan-head; (b) a model of the fan-head propagating along the bond from left to right and creating off-fault tensile cracks in the bulk material; (c) schema illustrating features of the off-fault cracking process observed in photo-elastic experiments; and, (d), (e) and (f) features of tensile cracks formation in coherent (bonded) and frictional interfaces

4.4 Conditions of instability and spontaneous rupture propagation

4.4.1 Theoretical explanation based on fan-mechanism model/theory

The analysis conducted in the preceding sections showed that the fan-structure represents a natural strength weakening mechanism that governs shear rupture propagation with extreme dynamics. The physical and mathematical models showed that, for the initial formation of the fan-structure, a local irreversible deformation accompanied by a specific microcracking is required. The generation of the initial fan-structure can be caused by different methods, which will be discussed later. This section shows that at a certain stage of the initial fan-structure formation this process becomes inevitably instable leading to spontaneous rupture growth caused by the fan-structure. The reason for that is explained in Figure 14.

The blue horizontal line in Figure 14(a) indicates the level of distributed shear stress τ applied to the model (shown under the graph) before the fan initiation. This stress is too small to cause shear displacement. For this model, a local irreversible deformation accompanied by formation of tensile cracks and domino-blocks can be organised by application of high local shear stress. When the local stress τ_{loc} exceeds τ_a the consecutive generation of tensile cracks and formation of domino-blocks occurs (Figure 14(b)). For formation of the front half of the fan-structure, the applied local stress should reach the material strength

τ_u (if the rupture is generated in intact material) or the frictional strength τ_f (if the rupture is generated in the frictional interface). At formation of the rear half of the fan-structure the general instability of the rupture propagation associated with spontaneous rupture growth should start beyond point A where shear resistance of the developing fan is less than the applied stress τ. The mathematical model discussed in Section 3.2 describes conditions of instability by Equation (10):

$$F = F_k = \left(\frac{N}{\delta} ln \left|\frac{\sin(\alpha_0+k\delta)}{\sin(\alpha_0)}\right| + f_c - kf_\tau\right) \leq 0 \qquad (10)$$

It is important to note that the rest part of the fan-structure at the stage AM will be formed in dynamic (spontaneous) regime with accelerating the rupture velocity. Figure 14(b) shows an incomplete fan-structure at the moment of the instability start. After completion of the fan-structure its shear resistance reaches the minimum level, which causes rupture propagation with a maximum rupture velocity.

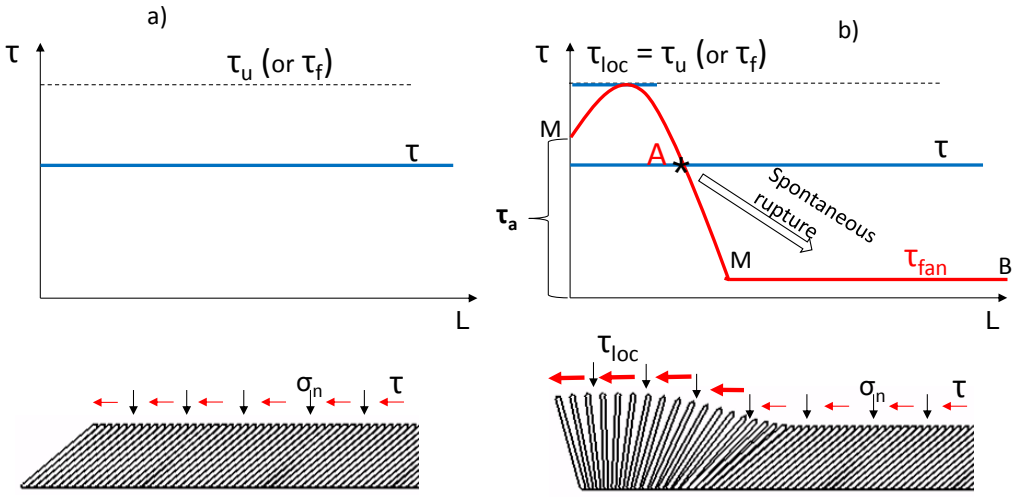

Figure 14 Illustration of conditions for the start of spontaneous rupture propagation caused by the fan-mechanism

4.4.2 Fan-mechanism model applied to experimental result

This section discusses how dynamic shear ruptures of extreme dynamics have been initiated in different laboratory experiments on pre-cut specimens. It will be shown that the rupture behaviour in all experiments is in accord with the fan-mechanism. It should be noted, again, that materials of all specimens were brittle and the rupture propagation was accompanied by intensive microcracking process in the rupture head reported in, for example, Lei et al. (2000), Ghaffari et al. (2014), Rosakis et al. (1999), Samudrala et al. (2002), Griffith et al. (2009), Rubinstein et al. (2004) and Ben-David et al. (2010).

The specimen type in Figure 15(a) was used in the experiments discussed in Figures 6(d) and 6(e) conducted by Rubinstein et al. (2004) and Ben-David et al. (2010) on PMMA specimens. The specimen was initially loaded by force F_n to create normal stress σ_n in the interface AB. As reported by the researches, force F_s applied then to the upper block's 'trailing' edge generated non-uniform shear stress τ distribution along the interface shown symbolically by the blue line in Figure 15(b). In the perfectly prepared interface (1 μm root-mean-square roughness) the distribution of the frictional strength τ_f can be considered as uniform, as shown by the black dotted line in Figure 15(b). When shear stress τ in the 'trailing' zone locally approaches the frictional strength, the interface in this zone is subjected to irreversible deformation with microcracking processes. We suppose that shear displacement accompanied by microcracking causes the initial formation of the fan-structure. The red graph in Figure 15(b) illustrates variation in shear resistance of the fan-structure at its initial formation and then at propagation of the completed fan as discussed in Figure 14(b). The spontaneous rupture propagation starts at the descending part of the red curve where shear resistance of the developing fan becomes less than the applied shear stress. The completed fan with extremely low shear resistance provides the extreme rupture propagation at shear stresses applied the level of which is less than the frictional strength. Intersonic rupture velocities were observed in these experiments.

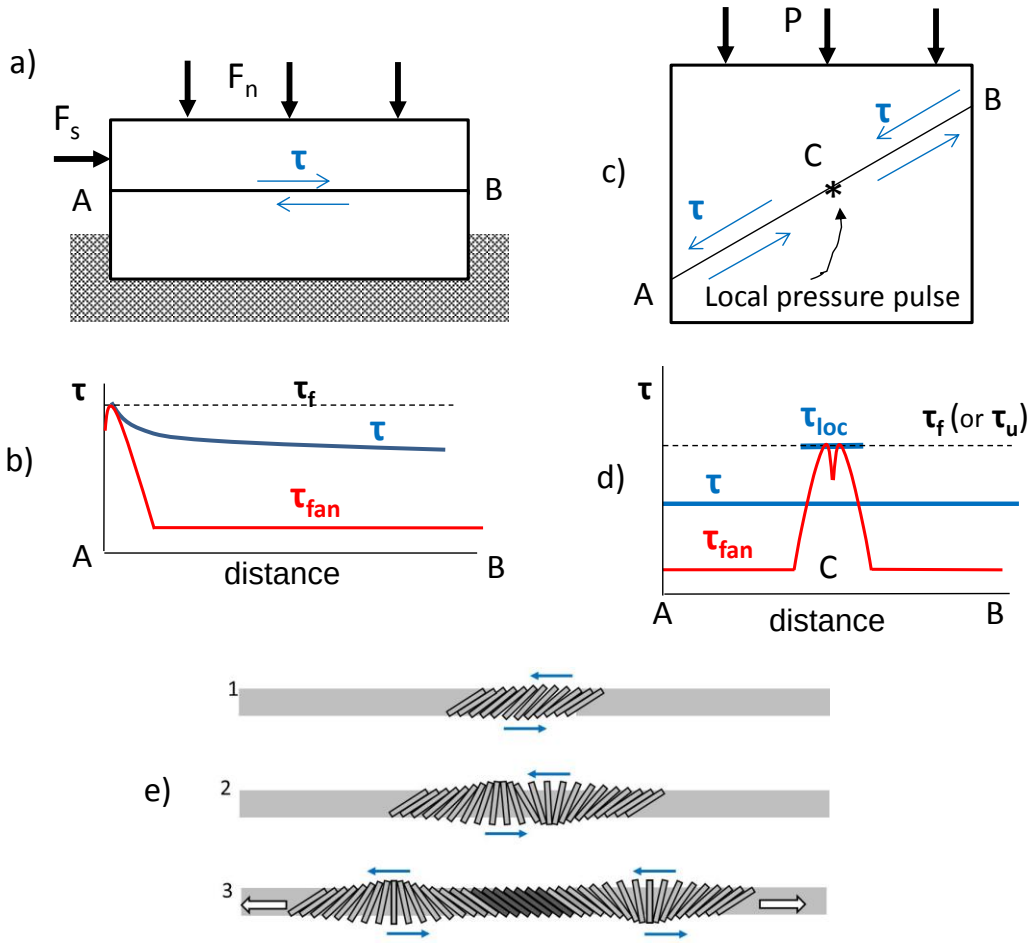

Figure 15 Spontaneous rupture initiation in different experiments on extreme rupture dynamics

Schema in Figure 15(c) was used in experiments on homalite specimens conducted by Xia et al. (2004), Griffith et al. (2009) and Ngo et al. (2012). Both frictional and bonded interfaces were used in different experiments. The inclined interface AB in all experiments was prestressed in compression and in shear. Rupture was initiated in the centre of the simulated fault by producing a local pressure pulse in a small area of the interface. The produced pressure generates locally irreversible deformation and microcracking process, which can lead to the formation of the fan-structure. The red graph in Figure 15(d) illustrates a possible variation of shear resistance of the fan-structure at the initial formation and further propagation of the completed fan. It should be noted that, in these experiments, the generated ruptures propagated bilaterally from point C towards points A and B. The principal of bilateral rupture generation by the fan-mechanism is illustrated in Figure 15(e). Intersonic rupture velocities were observed in these experiments.

Special comments are required for experiments on extreme rupture dynamics conducted by Rosakis et al. (1999) and Samudrala et al. (2002) on the specimen type shown in Figure 16. Here, in contrast to the experiments discussed in Figure 15, the bonded interface between two blocks of brittle homalite was not prestressed by normal stress. Shear ruptures of extreme dynamics up to intersonic velocities were generated in the interface by impact shear loading. It should be noted that, for the fan-mechanism activation, the existence of normal stresses is essential because it provides self-balancing conditions in the fan-structure as discussed in Figure 4. The important feature of bonded interfaces is the fact that the normal stresses here are generated in the propagating fan by reactive forces of interfaces as shown in Figure 16. The impact loading generates shear stresses in the 'trailing' zone of the interface, the level of which exceeds the bond strength $\tau_{loc} \geq \tau_u$. The irreversible deformation caused in this zone is accompanied by the formation of tensile cracks and intercrack blocks. The consecutive creation and rotation of domino-blocks causes elastic deformation of the rupture faces in the direction perpendicular to the bond plane. The reactive forces generated by the rupture faces represent normal stresses affecting the fan-head

at any stage of its propagation. After formation of the fan-structure shear resistance of the rupture head dramatically decreases providing corresponding strength weakening of the rupture head which can propagate with extreme dynamics under the effect of applied shock waves. Intersonic rupture velocities were observed in these experiments.

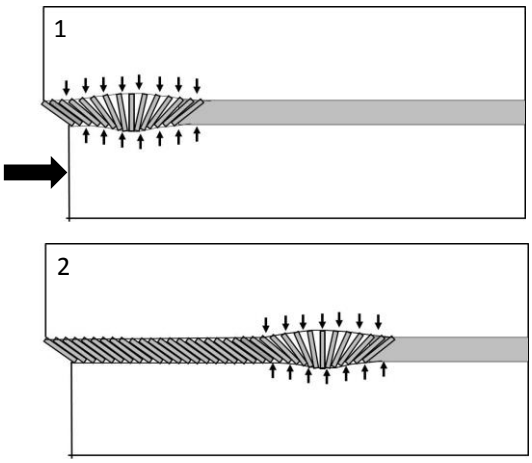

Figure 16 Extreme ruptures in bonded interfaces without normal prestress

4.5 High rupture velocity

4.5.1 Relation between slip and rupture velocities determined by the fan-mechanism

The next unique feature of the fan-mechanism is the capability to provide an extremely high rupture velocity at a relatively slow rotation of the domino-blocks. Figure 17 illustrates this. It shows the fan-head at three stages of propagation (1, 2 and 3). The fan at stages 2 and 3 are shown as shifted down. The fan-head propagates through the material due to the formation and rotation of domino-blocks. The front (red) block at stage 1, after complete rotation, represents the rear block of the fan at stage 3. The distance Δ associated with the block rotation corresponds to relative displacement (slip) of the rupture faces. During the time at which the slip Δ occurs, the fracture tip propagates the distance d. According to the fan-mechanism, the rate between the rupture and slip velocities is determined by the rate d/Δ. However, for long fan structures, typical for natural faults, we can assume that d ≈ ℓ_{fan}. In this case the rate between the rupture velocity V and the slip velocity Q can be expressed by Equation (11):

$$V/Q \approx l_{fan}/\Delta \tag{11}$$

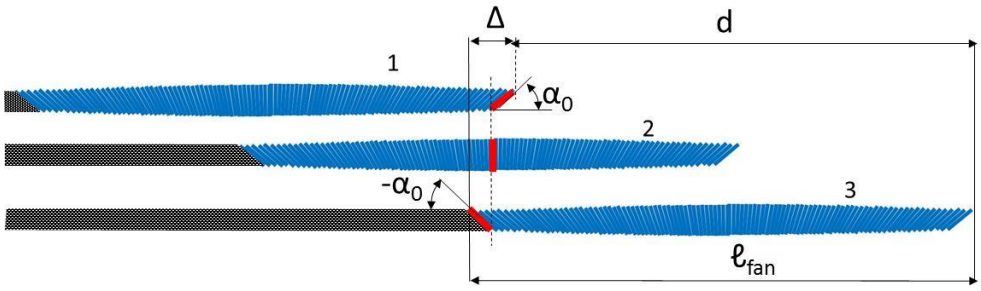

Figure 17 Fan-mechanism determines the relation between slip and rupture velocities

4.5.2 Two stages of dynamic rupture propagation: acceleration and constant velocity

We can check the validity of Equation (11) by analysing some experimental results. In different experiments on extreme rupture dynamics (e.g. Ohnaka & Shen 1999; Rosakis et al. 1999; Rubinstein et al. 2004; Lu et al. 2010; Xia et al. 2004) it was observed that after the instability start the shear rupture propagation has two dynamic stages: rupture acceleration and then propagation with a constant rupture velocity. This behaviour is in accordance with the fan-mechanism. At the initial creation of the fan-structure the

instability can occur during formation of the second half of the fan as discussed in Section 4.4. The fan-structure reaches the minimum shear resistance and acquires the capability to operate as a stress intensifier with maximum efficiency after the completion of the fan. We can suppose that the stage of the fan-formation associated with strong weakening should be accompanied by rupture acceleration, while the completed fan-structure should provide constant rupture velocity.

Figure 18(a) illustrates two stages of the spontaneous rupture growth obtained on PMMA specimens the configuration of which, and loading conditions, are shown in Figure 15(a) (Rubinstein et al. 2004). The blue curve on the left representing the acceleration stage shows that the rupture velocity increases from sub-Rayleigh up to intersonic levels. The shear wave velocity V_s = 1,000 m/s is indicated by the black horizontal dotted line. The red curve corresponds to the rupture propagation with approximately constant velocity. After point B the rupture velocity is stable intersonic. We can suppose that at point B the fan-structure formation has completed. In this case the fan length is ℓ_{fan} = 6.2 cm. In experiments conducted by Ben-David et al. (2010) on PMMA specimens, the relation between slip $\delta_{rapid} = \Delta$ and slip velocity $V_{rapid} = Q$ was determined (Figure 18(b)). Due to linear relation between δ_{rapid} and V_{rapid} we can estimate the ratio Q/Δ using this graph. For example, from Figure 18(b) we have: Q = 11.7 cm/s, Δ = 0.0007 cm. From Equation (11) we can estimate the rupture velocity as $V = Q\,\ell_{fan}/\Delta \approx 1.04$ km/s. The calculated value of the rupture velocity correlates with the experiment.

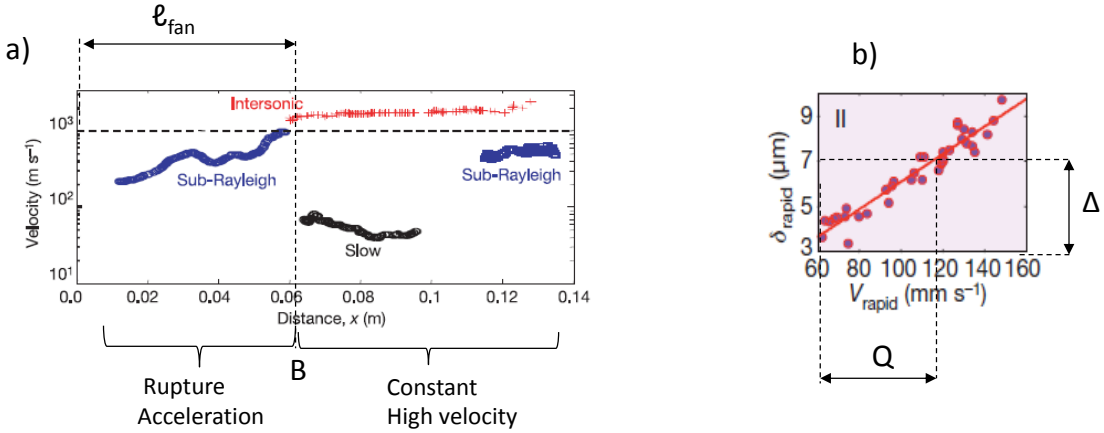

Figure 18 Illustration of two stages of the spontaneous rupture growth along a pre-existing interface and the relation between the interface slip and slip velocity obtained for PMMA specimens (Rubinstein et al. 2004; Ben-David et al. 2010)

4.6 Fan-mechanism efficiency in pre-existing interfaces

The possibility of the fan-mechanism activation in pre-existing interfaces depends on a number of factors. It can be activated at specific combinations of such parameters as material strength, brittleness, the interface condition (e.g. roughness of surfaces), level of normal stress etc. Different combinations of these factors vary the fan-mechanism efficiency. In this section we introduce briefly the effect of the interface surfaces roughness observed in the discussed experiments. For frictional interfaces the length of domino-blocks is determined by roughness of contacted surfaces. Roughness is defined as the average height of the surface profile. Ohnaka and Shen (1999) studied experimentally the role of the fault surfaces roughness in rupture propagation. Specimens with three different parameters of roughness were used in experiments: ≈ 10 μm, ≈ 20 μm and ≈ 70 μm. Experiments showed that extreme ruptures with velocities close to the shear wave velocity (2.9 km/s) were developed on faults with small roughness of ≈ 10 μm only. The fault surfaces roughness of homalite and PMMA specimens, where supershear velocities were observed, was within 1–5 μm (Rubinstein et al. 2004; Lykotrafitis et al. 2006; Ben-David et al. 2010; Lu et al. 2007, 2010). Using this information we can conclude that extreme ruptures in frictional interfaces can be developed in fine interfaces where 'welded' contacted asperities representing the intact material (according to Bowden & Tabor 2001) provide a sufficient density of the 'welded' zones for the fan-structure creation. High roughness and the presence of gouge between rupture surfaces do not provide conditions for the domino-block formation and, consequently, the fan-mechanism activation.

5 Post-peak properties of intact hard rocks at high confining pressure

5.1 Conditions of the fan-mechanism activation in intact rocks

In the previous sections we discussed unique features of the fan-structure and demonstrated that the fan-mechanism provides extreme dynamics of shear rupture propagation in pre-existing interfaces. In this section we will show that extreme ruptures in intact hard rocks at high confining stresses σ_3 are also governed by the fan-mechanism. First of all it should be noted that the consecutive creation of tensile cracks and intercrack (domino) blocks is the fundamental mechanism of shear rupture propagation in brittle medium. Shear rupture development in pre-cut specimens is predetermined by pre-existing interfaces. Length of tensile cracks and intercrack blocks in this case is determined by the interface thickness. In intact brittle rocks the rupture interface is not pre-determined. Furthermore, a shear rupture acquires capability to propagate in its own plane at conditions of confined compression. This rock feature is illustrated in Figure 19.

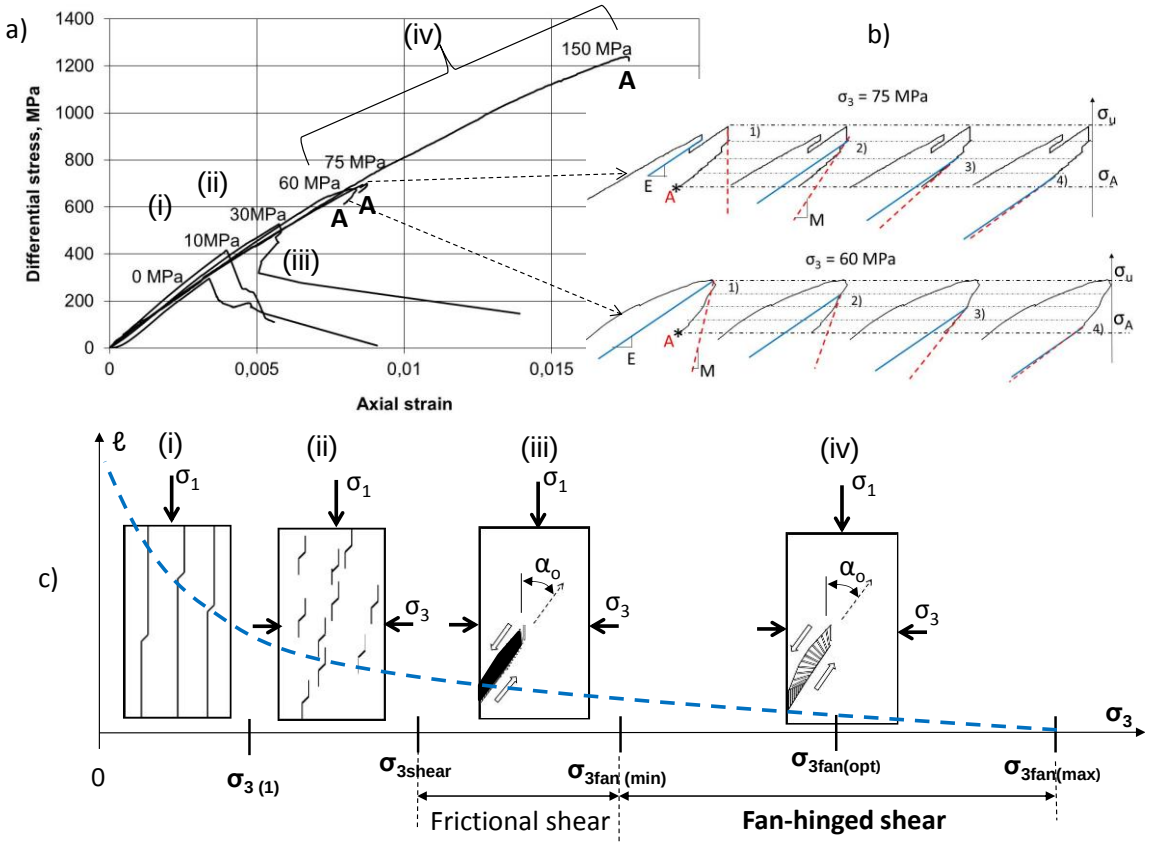

Figure 19 (a) Stress–strain curves for dolerite specimens tested at different levels of confining pressure; (b) enlarged fragments of post-peak curves, before the instability, start at points A for σ_3 = 75 MPa and 60 MPa; and, (c) the evolution of failure mechanisms in hard rocks with rising confining pressure σ_3

Let us analyse the evolution of rupture mechanisms in hard rocks with rising confining pressure σ_2 using stress–strain curves for dolerite specimens (UCS = 300 MPa) shown in Figure 19(a). The testing was conducted on an ultra-stiff, servo-controlled testing machine based upon the loading principles described in Stavrogin & Tarasov (2001). The loading stiffness of the machine was 4 MN/mm, the loop-closure rate of control system was 10 kHz. Curves in Figure 19(a) show that increasing confining pressure changes post-peak rock behaviour from Class I to extreme Class II. At $\sigma_3 < 60$ MPa the total post-peak control was provided for both types of rock response: Class I and Class II. At $\sigma_3 \geq 60$ MPa control was only possible at the start of the post-peak stage. After points A on the graphs, the unstable failure took place characterised by abnormally high dynamics and violence. The post-peak dynamic failure at high $\sigma_3 \geq 60$ MPa is associated with propagation of a thin shear fracture (thickness less than 0.1 mm).

The reason for loss of control after points A can be explained on the basis of analysis of enlarged fragments of the stress–strain curves for σ_3 = 75 and 60 MPa involving the post-peak parts at stress degradation from σ_u till σ_A presented in Figure 19(b). The fragments are replicated four times and divided into four steps (from 1 to 4) with equal intervals of differential stress. Each post-peak step is characterised by elastic modulus E (solid blue lines) and post-peak modulus M (dotted red lines). To determine elastic modulus the specimen tested at σ_3 = 75 MPa was slightly unloaded just before the peak stress. The same value of elastic modulus was used for σ_3 = 60 MPa. Areas located between the E and M lines at each post-peak step indicate the current post-peak rupture energy W_r associated with shear rupture development. We can see that W_r decreases dramatically with the rupture development from step 1 to step 4. It should be noted that, within the whole stress region between σ_u and σ_A, the servo-control system provided reliable control of the static fracture growth. However, after points A where the fracture energy became vanishingly small (post-peak modulus M and elastic modulus E practically coincide), the instable fracture propagation started. Despite very high values of the loading stiffness and the loop-closure rate of control system, the machine could not provide sufficiently high unloading velocity to prevent the spontaneous shear rupture propagation beyond points A.

The underlying mechanics of hard rock failure under high σ_3 can be explained by analysis of the evolution of failure mechanisms in rock specimens (I–IV) with rising confining stress σ_3 as represented schematically in Figure 19(c). Confining pressure σ_3 increases along the horizontal axis from left to right. At the origin of the horizontal axis σ_3 = 0. It is known that failure of brittle rocks is accompanied by formation of tensile cracks at any level of σ_3. However, the ultimate length ℓ of tensile cracks that can be developed at failure depends on the level of σ_3. A dotted blue line in Figure 19(c) shows symbolically the typical variation of ultimate length ℓ of tensile cracks as a function of σ_3: the higher σ_3 the shorter ℓ. The length ℓ of tensile cracks in turn determines the macroscopic failure mechanism and the failure pattern shown schematically in rock specimens (i) to (iv).

At confining pressures $0 \le \sigma_3 < \sigma_{3shear}$ shear rupture cannot propagate in its own plane due to creation at the rupture tip of relatively long tensile cracks that prevent the shear rupture propagation. Two failure mechanisms may be distinguished at these stress conditions:

- Splitting by long tensile (extension) cracks: specimen (i) in Figure 19(c).
- Distributed microcracking followed by coalescence of microcracks: specimen (ii) in Figure 19(c).

At $\sigma_3 \ge \sigma_{3shear}$ the failure mode is localised shear. Here high confining pressure suppresses the formation of long tensile cracks and tensile cracks generated in the rupture tip become sufficiently short to assist shear rupture to propagate in its own plane. According to Reches and Lockner (1994) the fracture front moves through the rock due to creation of an echelon of micro tensile cracks in the fracture tip. Here dilation of one microcrack induces dilation of closely spaced neighbouring cracks and creates an echelon of inclined intercrack domino-blocks, as discussed in Section 2 (Figure 2). These domino-blocks are subjected to rotation at shear displacement of the rupture faces (Peng & Johnson 1972; King & Sammis 1992; Reches & Lockner 1994). However, the decrease in length of tensile cracks and domino-blocks with rising σ_3 causes fundamentally different behaviour of rotating domino-blocks within different ranges of σ_3:

- Frictional shear — specimen (iii) in Figure 19(c). This mechanism operates within the pressure range $\sigma_{3shear} \le \sigma_3 \le \sigma_{3fan(min)}$. Shear displacement of the rupture faces is accompanied by collapse of relatively long domino-blocks during rotation that provides friction in the rupture head.
- Fan-hinged shear — specimen (iv) in Figure 19(c). Within the pressure range $\sigma_{3fan(min)} < \sigma_3 < \sigma_{3fan(max)}$ specifically short domino-blocks formed from very strong material (UCS ≥ 250 MPa) can withstand the rotation caused by shear displacement of the rupture faces without collapse. Due to consecutive generation and rotation of the domino-blocks they create the fan-structure representing the shear rupture head. The fan-mechanism governing shear rupture development at these conditions makes failure extremely dynamic and violent.

5.2 Low transient strength of hard rocks at highly confined compression

Due to inability to prevent spontaneous dynamic failure in the post-peak region caused by the fan-mechanism real post-peak properties of hard rocks with UCS > 250 MPa at high σ_3 corresponding to seismogenic depths are experimentally unexplored and actually unknown. However, the new knowledge about unique features of the fan-mechanism allows us deriving the inaccessible information about real post-peak properties of hard rocks at high confining stresses.

General features of the shear rupture propagation in hard intact rocks at high σ_3 governed by the fan-mechanism are illustrated in Figure 20. Figure 20(a) shows five stages of the fan-head formation and propagation in a rock specimen along the dotted line ON. The fan-head here is shown as a red ellipse. Applied stresses σ_1 and σ_3 induce the distributed shear stress τ along the line ON indicating the future fault. Acoustic emission studies (e.g. Reches & Lockner 1994; Lei et al. 2000) show that in hard rocks under high confining stresses, the microcracking process evidencing the nucleation of a localised shear rupture takes place at the pre-peak stage close to peak stress. The microcracking process is the basis for the fan-structure formation.

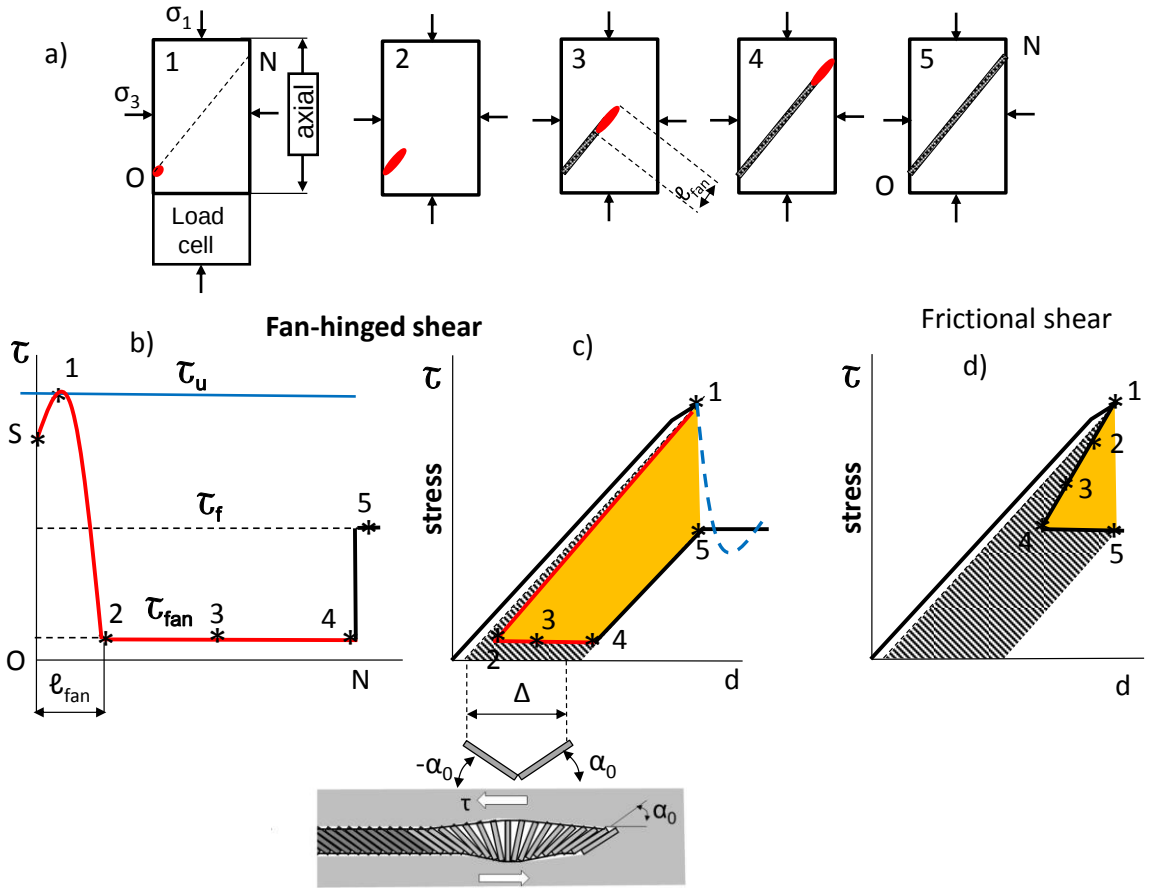

Figure 20 Features of the failure process, governed by the fan-mechanism in specimens of hard rocks tested at high confining pressure σ_3, and post-peak rock properties

The red curve in Figure 20(b) illustrates the variation in shear resistance of the fan-head during the fan-structure formation and propagation through the specimen between points O and N. Points on the curve indicate identical stages of shear rupture propagation shown in Figure 20(a). Point S corresponds to the level of distributed shear stress at which the fan-structure starts developing on the basis of a weakest zone in the specimen (e.g. on the basis of a pre-existing defect). Further, its development is caused by further increasing axial load and, consequently, distributed shear stress τ. Between points S and 1 the stable formation of the front half of the fan-structure takes place.

At point 1, when the front half of the fan has completed, the level of distributed shear stress τ (blue line) applied along the future fault (dotted line ON) is equal to the maximum shear resistance of the developing

fan. Point 1, therefore, represents the onset of instability in the fan formation. Further development of the fan-head and its propagation through the specimen occurs in the dynamic regime, because shear resistance of the fan-structure at this stage sharply decreases and becomes less than the level of distributed shear stress applied. The stage between points 1 and 2 reflects shear resistance of the fan-structure during dynamic formation of the rear part of the fan. At point 2 shear resistance of the fan-head equal to τ_{fan} is determined by the completed fan-structure. It should be emphasised that, after completion of the fan-head, the spontaneous propagation of the shear rupture through the intact material between stages 2 and 4 can proceed at any level of stress exceeding τ_{fan}. This means that during this stage of the failure process the transient strength of intact rock is equal to τ_{fan}, which can be significantly less than the frictional strength τ_f. When the fan-head has crossed the specimen (stage 5), the specimen strength is determined by friction τ_f.

The stress–displacement curve in Figure 20(c) reflects real post-peak properties of hard rocks caused by the fan-mechanism. The post-peak stage between points 1 and 2 is associated with formation of the rear half of the fan-structure. The analysis of post-peak curves before the instability start in Figure 19(b) demonstrates that the post-peak modulus of hard rocks at high σ_3 almost coincides with the elastic unloading modulus indicating extremely low rupture energy. The red line 1–2 in Figure 20(c) represents the descending part of the post-peak curve. The post-peak rupture energy at this stage of failure is shown by the hatched area above the line 1–2. The horizontal red line 2–4 represents the transient strength τ_{fan} of the intact material during the failure process. We will refer to this strength as the fan-strength τ_{fan}. The displacement Δ with very small shear resistance τ_{fan}, is provided by rotating domino-blocks of the fan-structure, which is illustrated by images under the graphs representing the fan-head. The post-peak rupture energy at this stage of the rupture process corresponds to the hatched area below the red line 2–4. When the fan-head has crossed the specimen (stage 5), the specimen strength is determined by normal friction τ_f.

To prevent spontaneous failure the high stress applied to the specimen at point 1 should be dropped below τ_{fan} before the fan-head has crossed the specimen. However, due to the fact that the rupture velocity in intact rocks can reach intersonic levels modern servo-controlled testing machines cannot provide a sufficiently high speed of unloading to interrupt the failure process due to high inertia of loading actuators. As a result, the failure occurs with extreme dynamics that does not allow recording of the true material properties during the failure process. The dotted blue curve in Figure 20(c) illustrates the post-peak part of the stress-displacement graph typically measured at the uncontrollable spontaneous failure. We can see that this curve does not reflect absolutely the real post-peak rock properties caused by the fan-mechanism.

The post-peak properties caused by the fan-mechanism differ remarkably from the generally accepted properties of hard rocks illustrated in Figure 20(d). Hatched areas in Figures 20(c) and 20(d) represent post-peak rupture energy up to stage 5, while yellow areas correspond to elastic energy released from the specimens during post-peak failure. Abnormally high released energy caused by the fan-mechanism is the source of extreme dynamics and violence. These properties of hard rocks determine dynamic events at great depth. Without this knowledge it is impossible to understand properly mechanics of very powerful shear rupture rockbursts generated in intact rock mass surrounding deep mines and also mechanics of earthquakes. The fan-mechanism is the most energy efficient shear rupture mechanism.

5.3 Variable efficiency of the fan-mechanism

Equation (9) shows that the shear resistance of the fan-structure is determined by the domino-block geometry (ratio r/w) and friction (τ_f) between the ends of the rotating domino-blocks and shear rupture interfaces. The meaning of parameters involved in the equation is illustrated in Figure 21(a). Very short blocks ($r/w \leq 1$) cannot operate as hinges and shear resistance of the interfaces corresponds to normal friction τ_f. Increasing the ratio r/w increases the hinge efficiency and, consequently, decreases the shear resistance of the fan-structure. As discussed previously, the length of the domino-blocks is a function of confining pressure σ_3 (blue dotted line 'ℓ *versus* σ_3' in Figure 19(c)). By analogy with Figure 19(c), the blue dotted line in Figure 21 shows symbolically the variation of the ratio r/w versus σ_3 within the pressure range between σ_{3shear} and $\sigma_{3fan(max)}$. This line indicates the variation in fan-mechanism efficiency $\psi = \tau_f / \tau_{fan}$ with confining pressure, if the domino-blocks do not collapse at rotation.

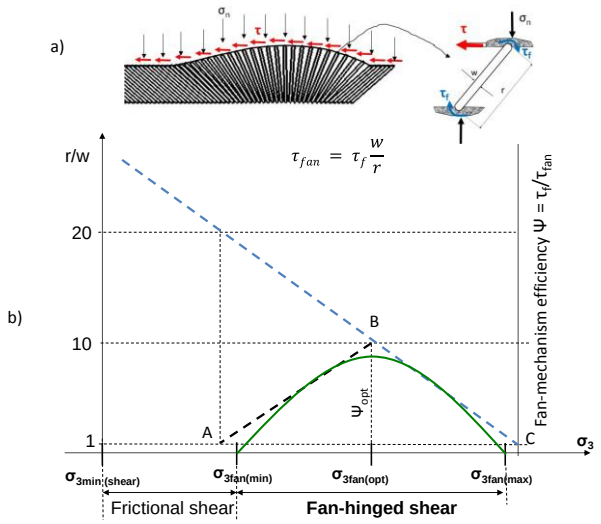

Figure 21 Variation of the fan-mechanism efficiency $\psi = \tau_f/\tau_{fan}$ with confining pressure σ_3 for hard rocks

Each block in the fan works as a beam with rotation-free end conditions loaded along the beam axis. Despite the fact that domino-blocks formed in hard rocks (UCS > 250 MPa) are very strong, they can collapse due to improper geometry causing a specific variation of the fan-mechanism efficiency with confining pressure. On the basis of information presented in Megahid et al. (1993) we assume that domino-blocks with slenderness ratio r/w ≤ 10 can withstand rotation. Domino-blocks with slenderness ratio r/w > 10 will collapse to varying degrees as they rotate, depending on the ratio r/w. At r/w > 20 the blocks collapse easily and, therefore, lose any potential to operate as hinges. The inclined black dotted line AB located between $\sigma_{3fan(min)}$ and $\sigma_{3fan(opt)}$ reflects symbolically a possible variation of the fan-mechanism efficiency $\psi = \tau_f/\tau_{fan}$ within this pressure range. The total variation of the fan-mechanism efficiency should be within triangle ABC and represented by the green curve. The key point is that the fan-mechanism is active only within the range of confining pressure $\sigma_{3fan(min)} < \sigma_3 < \sigma_{3fan(max)}$, with optimal efficiency ψ_{opt} at $\sigma_{3fan(opt)}$.

The fan-mechanism efficiency depends also on the material strength (rock hardness). Figure 22(a) shows three curves indicating variations of $\psi = \tau_f/\tau_{fan}$ versus σ_3 for three rocks of different hardness. Here the harder the rock the greater the optimal fan-mechanism efficiency ψ_{opt} and the larger the range of σ_3 where the fan-mechanism is active. The red curve in Figure 22(b) illustrates symbolically the dependence of the optimal efficiency of the fan-mechanism ψ_{opt} on the rock strength (UCS). The fan-mechanism operates with the largest efficiency in rocks with UCS > 250 MPa. Within the range of UCS 150–250 (roughly) the efficiency is significantly lower. In soft rocks the fan-mechanism is not active. The variable efficiency of the fan-mechanism with confining pressure determines corresponding variations of such rock properties as post-peak brittleness and post-peak transient strength. These questions will be discussed in Sections 5.4 and 5.5.

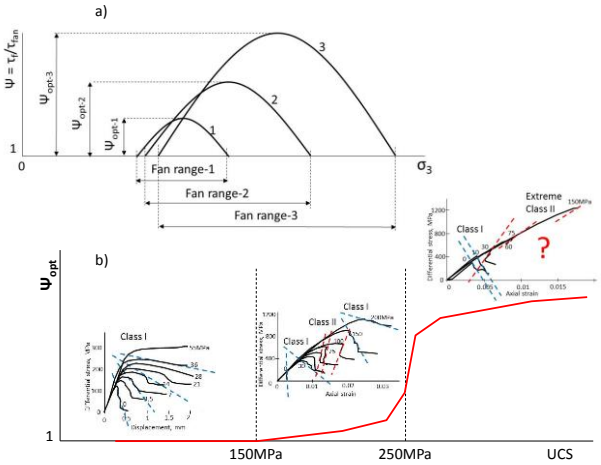

Figure 22 (a) Variation of the fan-mechanism efficiency $\psi = \tau_f/\tau_{fan}$ versus confining pressure σ_3 for rocks of different hardness; and, (b) variation of the optimal efficiency of the fan-mechanism ψ_{opt} versus UCS

5.4 Dramatic rock embrittlement at high confining pressures

5.4.1 Principle of determination of brittleness at compression

Experiments show that macroscopic instability associated with spontaneous failure of rock specimens in compression can only take place in the post-peak region. At the pre-peak stage the situation is stable. This implies that post-peak instability can be treated as a manifestation of rock brittleness, therefore, post-peak characteristics should be used for rock brittleness estimation. The division of rocks into two classes (Class I and Class II) on the basis of post-peak modulus proposed by Wawersik & Fairhurst (1970) represents a rough characterisation on rock brittleness. To provide detailed characterisation, a special brittleness index K_1 and universal scale of brittleness was developed in Tarasov (2010), and Tarasov and Potvin (2013).

Informative characteristics of intrinsic material properties, before and after the peak stress is reached, can be obtained from the complete stress–strain curves. Figure 23 illustrates the essence of the special brittleness index K_1. The post-peak curve here at different stages corresponds to Class I (Figure 23(a)) and Class II (Figure 23(b)) behaviour. Points B and C for both stages represent points located infinitely near to each other on the post-peak curve. The failure process between points B and C can be characterised by the following types of energy:

- Elastic energy withdrawn from the specimen dW_e (red area or delineated by the red line):

$$dW_e = \frac{\sigma_B^2 - \sigma_C^2}{2E} \tag{12}$$

- Rupture energy absorbed by the specimen dW_r (grey area):

$$dW_r = \frac{(\sigma_B^2 - \sigma_C^2)(M - E)}{2EM} \tag{13}$$

- Released energy dW_a (yellow area representing the excess of elastic energy that was not absorbed by the rupture process):

$$dW_a = \frac{\sigma_B^2 - \sigma_C^2}{2M} \tag{14}$$

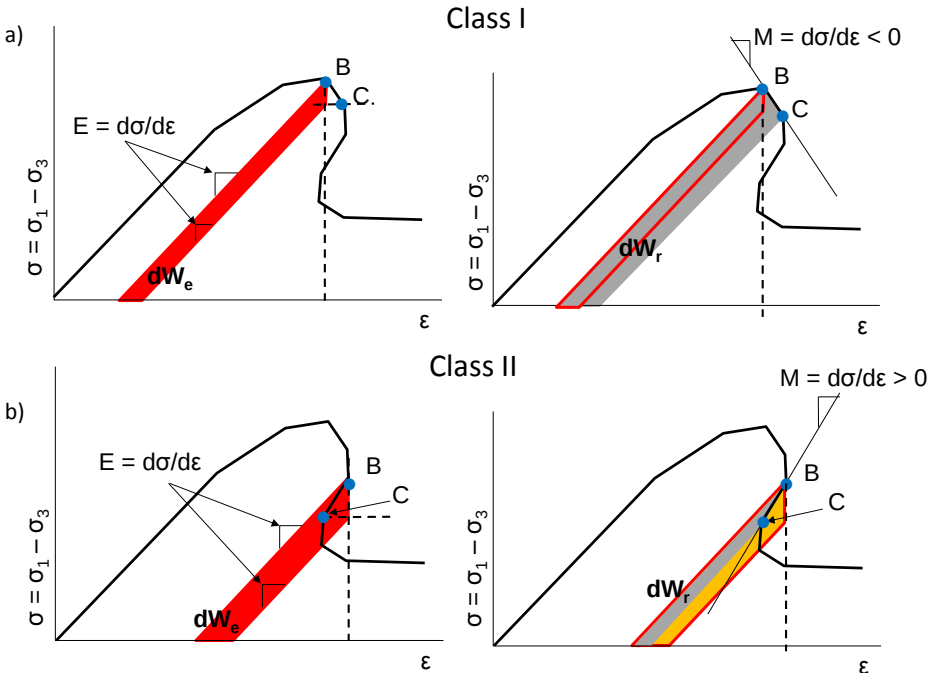

Figure 23 Principle of determination of brittleness index K_1

The brittleness index K_1 is determined by the ratio between the rupture energy and the withdrawn elastic energy:

$$K_1 = \frac{dW_r}{dW_e} = \frac{M - E}{M} \tag{15}$$

This index characterises the capability of the rock for self-sustaining failure due to the elastic energy available from the material. In other words, it characterises the degree of intrinsic instability of the material at failure.

Figure 24 shows the universal scale of brittleness based upon the index K_1, with brittleness increasing from left to right. The complete stress–strain curves illustrate how the different shapes of post-peak curves (indicated by dotted blue lines) describe a variation in brittleness. Areas delineated by red lines correspond to elastic energy W_e stored in the specimen at the peak stress, and available for the post-peak failure process. Grey areas represent the post-peak rupture energy W_r at complete failure. Yellow areas correspond with the released energy. The important point on the scale is K_1 = 1 representing the intermediate situation between Class I and Class II behaviour. On the right of this point the material behaviour is Class II, characterised as self-sustaining failure. The closer the value of K_1 is to zero, the more brittle the material and the more violent the failure. At absolute brittleness K_1 = 0, E = M and the post-peak rupture energy is equal to zero (Wr = 0), which means that the total elastic energy stored in the material body will be transformed into dynamic forms of energy. On the left of the point K_1 = 1, self-sustaining failure is impossible, and some additional energy from the loading system is necessary to cause the post-peak failure development. The greater the brittleness index K_1 in this region, the more ductile the post-peak rock behaviour. The index K_1 and the universal scale of brittleness are based on sound physics principles, and thus provide proper characterisation of rock brittleness for all types of rock and testing conditions (unconfined and confined compression). It should be emphasised that K_1 characterises the intrinsic rock brittleness independently of the loading stiffness.

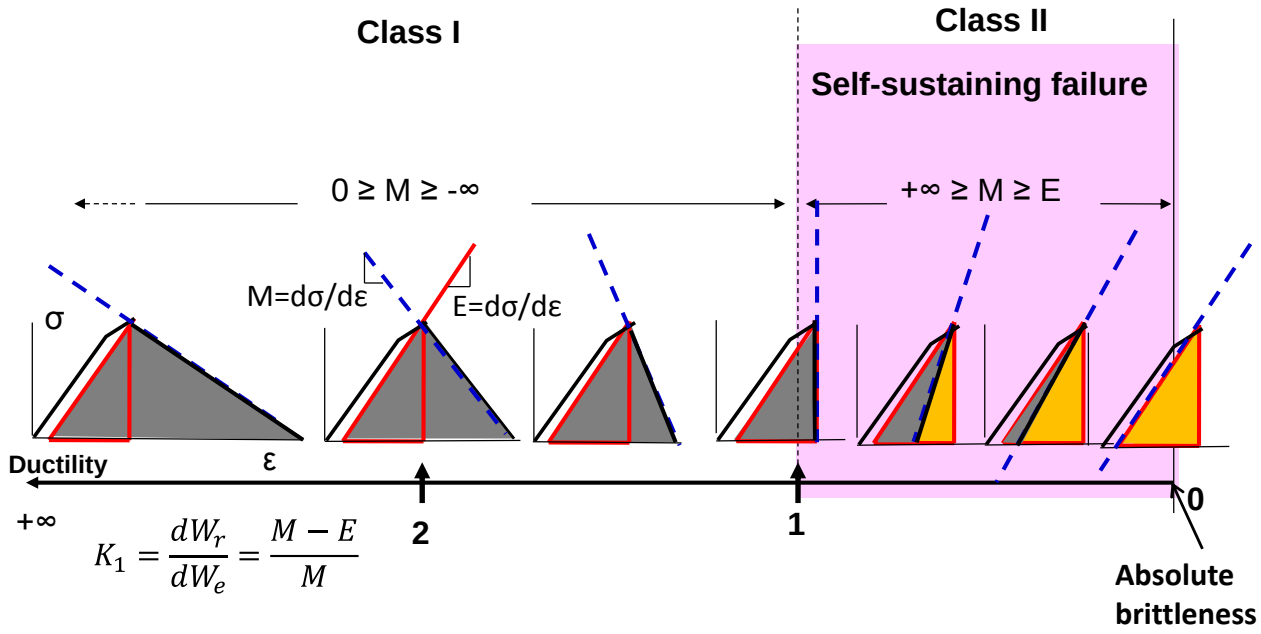

Figure 24 The universal scale of rock brittleness at compression

5.4.2 Rock brittleness variation with confining pressure caused by the fan-mechanism

Figure 25 shows the variation of brittleness index K_1 for rocks of different hardness: sandstone UCS = 150 MPa, quartzite UCS = 180 MPa, Westerly granite UCS = 250 MPa (Wawersik & Brace 1971), and dolerite UCS = 300 MPa. This demonstrates different responses to rising confining pressure σ_3.

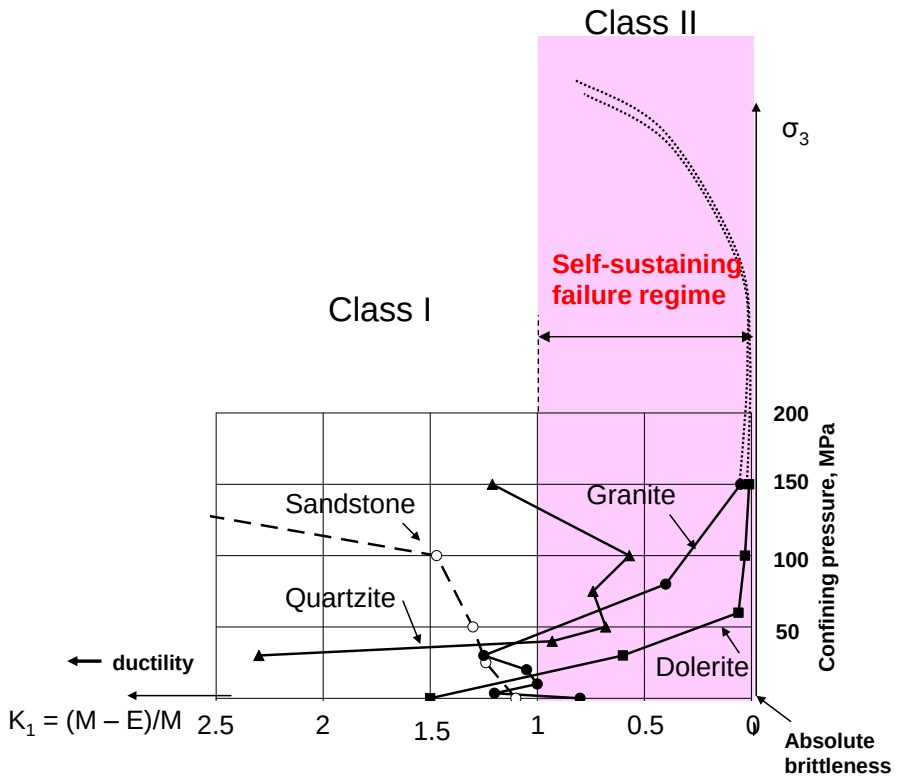

Figure 25 Variation of brittleness index K_1 versus confining pressure σ_3 for rocks of different hardness

The self-sustaining failure regime corresponds to $1 > K_1 > 0$ (pink area). The sandstone curve indicates that an increase in confinement σ_3 makes the rock less brittle. This behaviour is typical for soft rocks. For the quartzite (see stress–strain curves for this rock in Figures 1 and 22(b)), an increase in confinement σ_3 within the range of 30–100 MPa makes the material more brittle. At greater confinement, the brittleness decreases. For the granite, an increase in σ_3 within the range of 0–30 MPa makes it less brittle. When $\sigma_3 > 30$ *MPa*, the brittleness increases dramatically. The dolerite curve also shows very severe rock embrittlement (see stress–strain curves for this rock in Figures 1 and 22(b)). At σ_3 = 75 MPa, according to the brittleness index K_1, the dolerite became 250 times more brittle when compared to uniaxial compression ($K_{1(0)} = 1.5$; $K_{1(75)} = 0.006$). At σ_3 = 100 and 150 MPa, the brittleness increased significantly, further approaching absolute brittleness. The dotted lines indicate the expected brittleness variation for granite and dolerite at greater values of σ_3; the brittleness continues to increase until it reaches a maximum at some level of σ_3 and then decreases, as all rocks become ductile at very high σ_3. Such variation of brittleness is similar to one observed for quartzite. We can suppose that the maximum brittleness for granite and quartzite can be reached at $\sigma_3 \approx 300$ *MPa*. For softer rocks that are as hard as quartzite, the mode of brittleness variation is similar, but the maximum brittleness is lower and the range of confining pressure where embrittlement takes place is smaller.

The observed dramatic rock embrittlement within a specific range of confining pressure is caused by the fan-mechanism. The embrittlement depends on the fan-mechanism efficiency as discussed in Figure 22. The harder the rock the greater the pressure range of rock embrittlement and the greater the level of optimal brittleness.

5.5 New strength profiles for hard rocks

Variable efficiency of the fan-mechanism with confining stresses σ_3 determines corresponding variation in the transient strength of hard rocks (Tarasov 2016c, Tarasov & Randolph 2016). Figure 26(a) shows schematically an improved model of strength profiles involving the transient fan strength τ_{fan} profile (red curve) along with conventional fracture τ_u and frictional τ_f strength profiles. Stress-displacement curves in

Figures 26(b) and 26(c) reflecting real post-peak rock properties (similar to discussed in Figure 20(c)) explain the meaning of the fan strength and its variation versus σ_3. Figure 26(b) illustrates the situation at $\sigma_3 = \sigma_{3fan(opt)}$ where the fan-mechanism exhibits the maximum efficiency. At peak stress the material strength is τ_u. During spontaneous failure the completed fan-head determines the transient material strength τ_{fan}. This means that the shear fracture governed by the fan-mechanism can propagate through the material at any level of shear stress above τ_{fan}. After completion of the failure process the material strength is determined by the frictional strength τ_f of the new fault.

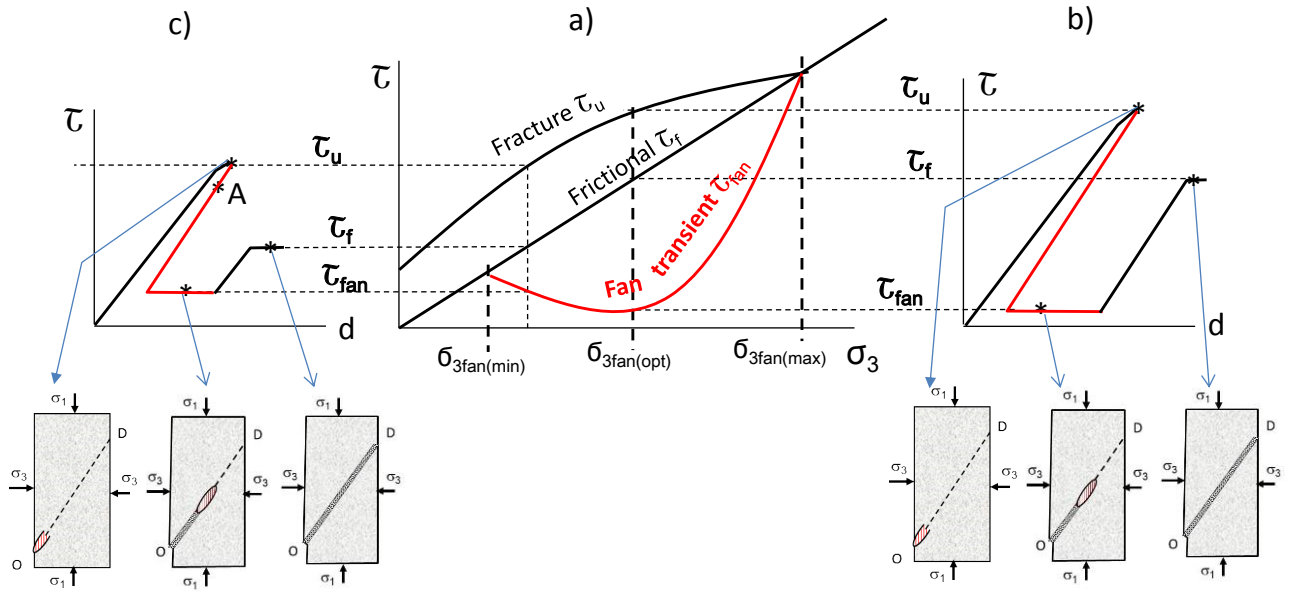

Figure 26 (a) Strength profiles of the fracture τ_u, frictional τ_f, and fan transient τ_{fan} strength for hard rocks; and, (b) and (c) complete stress–strain curves involving three characteristics of strength (τ_u, τ_f, τ_{fan})

For confining pressures $\sigma_3 < \sigma_{3fan(opt)}$ or $\sigma_3 > \sigma_{3fan(opt)}$ the fan-mechanism efficiency is lower. The graph in Figure 26(c) indicates the relative values of τ_u, τ_f and τ_{fan} and their positions on the envelops for the situation where $\sigma_3 < \sigma_{3fan(opt)}$. It should be noted that improper operation of domino-blocks at low efficiency of the fan-mechanism increases the level of τ_{fan} and also provides the possibility for restricted post-peak control up to point A (see experimental curves in Figure 19(a) for σ_3 = 60 and 75 MPa) before the start of instability. Stress–strain curves in Figure 19(a) show that the controllable post-peak part (between σ_u and σ_A) decreases with rising confining pressure indicating the improvement of the fan-mechanism operation. At σ_3 = 200 MPa the instability started right at the peak stress due to efficiency of the fan-mechanism close to the optimal level for this testing condition.

It should be noted that the pressure range of the fan-mechanism activity $\sigma_{3fan(min)} < \sigma_3 < \sigma_{3fan(max)}$ and the optimal level of the transient strength depend on the rock hardness (strength) as was discussed in Figure 22: the harder the rock the greater the pressure range of the fan-mechanism operation and the lower the optimal level of the transient strength. We can suppose that the maximum pressure $\sigma_{3fan(max)}$ of the range corresponds to conditions at which the fracture and frictional strength profiles in Figure 26(a) intersect. This subject, however, requires special studies.

6 Fan-mechanism in complex natural faults

6.1 Structure and evolution of segmented faults

Generally, faults have very complicated segmented and multi-hierarchical structure (Segal & Pollard 1980; Sibson 1982; Scholz 2002). Here we outline briefly some principles of the fault evolution in association with

the fan-mechanism (Tarasov 2014). Experiments conducted by Otsuki and Dilov (2005) in laboratory at high confining pressure demonstrated the following features of complex faults:

- Faults are multi-hierarchical segmented formations.
- Segmentation as a mechanism of fault propagation acts on all hierarchical ranks of complex faults.
- Segmentation is a result of advanced triggering of a new bilaterally propagating shear fracture (new segment) in front of the propagating current shear fracture (current segment) due to the stress transfer at some distance ahead of the current fracture.
- The current and new segments propagating toward each other form a jog (step) where they meet.
- Jogs of a compression type are very common at high confining pressures to fault zones regardless of their sizes.
- Once a number of segments of a given hierarchical rank coalesce, they behave as a whole as a new and longer segment of one higher rank.
- Segment of higher rank can trigger a new segment (shear fracture) at greater distance.
- The new triggered segment starts as a primary fracture.

All these features are illustrated below (Tarasov 2014a). Series of photographs in Figure 27(a) shows different stages (I to IV) of the fault evolution by the advanced triggering of new segments (modified from Otsuki & Dilov 2005). Segments are represented here by white lines. The fault propagates from left to right. The segments are generated one by one due to the stress transfer and propagate bilaterally. At the meeting of each two neighbouring segments they are connected by a compressive jog. Overlap zones of the jogs are subjected to significant irreversible deformation. Figure 27(b) shows features of compressive jogs formed in brittle quartzite (photographs from Ortlepp 1997). Overlap zones of these jogs are represented by a row of domino-blocks.

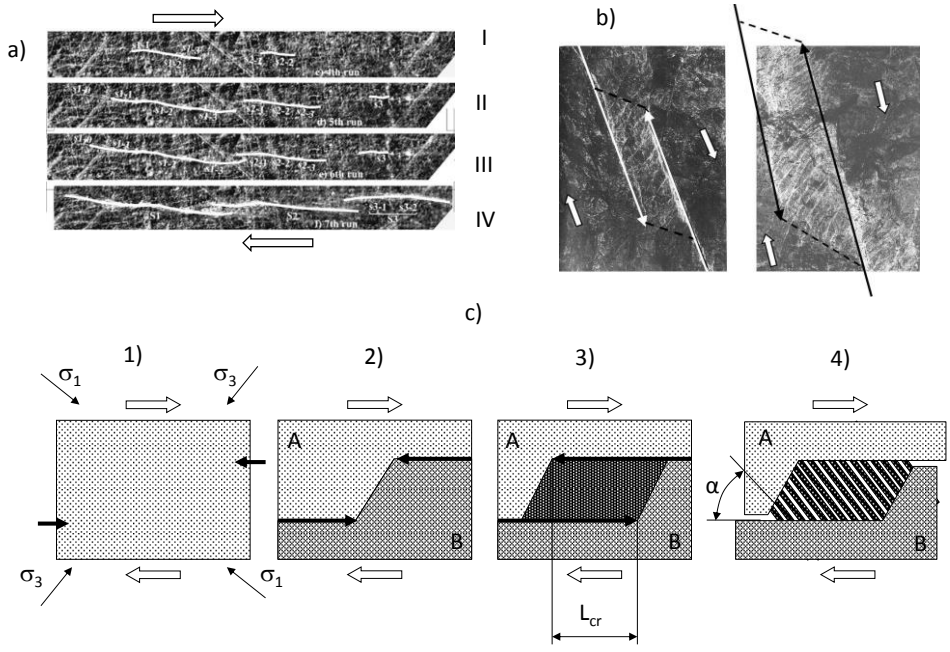

Figure 27 (a) Fault segmentation due to advanced triggering of new segments caused by the stress transfer; and, (b) and (c) creation of domino-structure on the basis of compressive jogs

Figure 27(c) proposes a possible mechanism of the domino-structure formation in compressive jogs (Tarasov & Ortlepp 2007). It shows four steps of linkage between two segments (bold arrows) propagating towards each other in intact rock. Figure 27(c-1) indicates the directions of the applied stresses against the propagating segments. In Figure 27(c-2) the rock mass surrounding the approaching segments is

theoretically divided into two massive blocks (A and B) pressed against each other by the applied stresses. The propagation of the segments decreases shear resistance between the massive blocks along these segments, which overstresses an area located between the tips of the approaching segments (Segall & Pollard 1980). With further propagation of the segments they confine a zone that is now overstressed (Figure 27(c-3)). When the extending overlap zone in hard brittle rocks reaches a critical length it fractures dynamically into an echelon of domino-blocks (slabs) due to the shear of the overlap zone between the parallel faces of the massive blocks A and B (Figure 27(c-4)). This process is accompanied by the release of some portion of elastic energy. After that the segments stop propagating. The initial orientation of the tensile cracks separating the overlap zone into domino-blocks is parallel to the major stress σ_1. By analogy with primary ruptures angle $\alpha_o \approx (30° \div 40°)$. In contrast to primary ruptures where the domino-blocks are generated sequentially one by one in the rupture tip this mechanism generates a row of parallel domino-blocks simultaneously within the overlap zone of compressive jogs.

The discussed mechanism can create cascades of compressive jogs, which in combination can represent a fault segment of higher hierarchical rank. Figure 28 illustrates the principle of formation of a multi-segmented fault, the photograph of which is shown on the right. The fault propagates upwards. Open arrows indicate the direction of shear stress applied. Six stages of the fault propagation are shown here. At stage I a dynamically propagating primary shear fracture triggers an advanced fracture. Asterisks indicate centres of initiation of advanced triggered fractures. This new fracture (as well as all further triggered fractures) propagates bilaterally towards the current fracture and in the opposite direction. This fracture in turn triggers the next advanced fracture shown at stage II. At this stage the overlap zone between the two bottom fractures has reached the critical length and divided into a row of domino-blocks. Further fault development occurs through repetition of similar stages. In Figure 28 new compressive jogs adjoining the tip of propagating fault are shown in red.

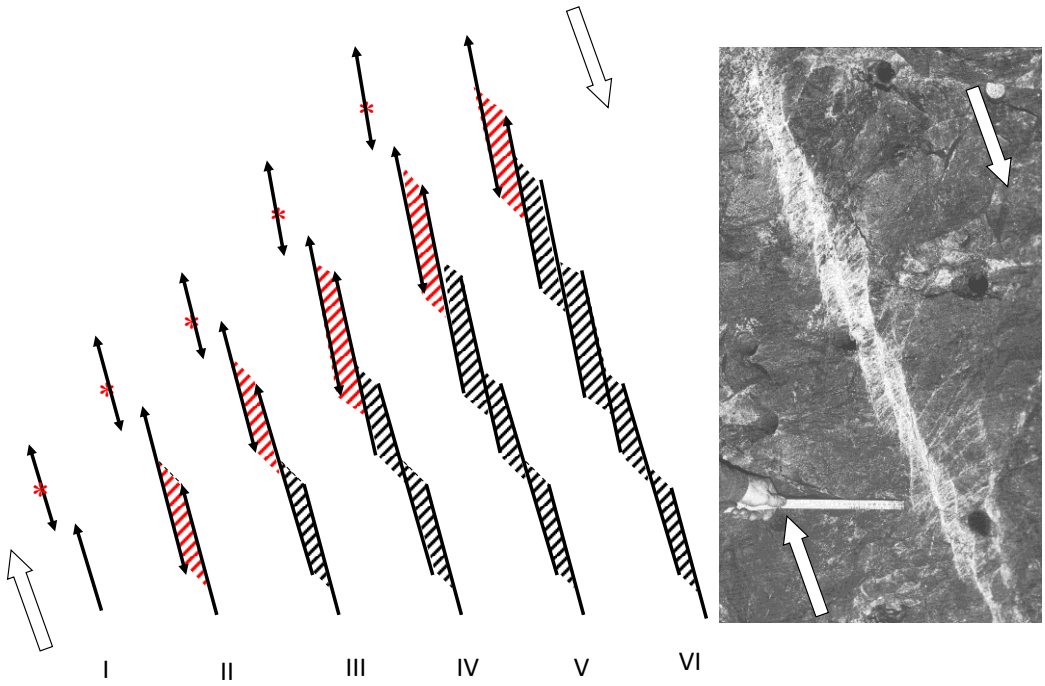

Figure 28 Cascade-like combination of compressive jogs formed due to advanced triggering of new segments (photograph from Ortlepp 1997)

Figure 29 shows evolution of a multi-hierarchical segmented fault. The fault nucleates as a primary shear fracture (left-bottom corner) because the fan-mechanism mobilised in very thin primary ruptures is the most energy efficient shear rupture mechanism. A new primary rupture can be triggered in front of the current one at a distance X_I due to stress transfer. Primary ruptures represent segments of rank-I. Once a number of segments of a given hierarchical rank coalesce, they behave as a whole as a new and longer segment of one higher rank. The rank-II segmented rupture can trigger a series of new primary ruptures at

different distances with maximum remoteness of X_{II}. The key feature of fault segmentation is the fact that a new segment triggered by the current segment of any rank nucleates as a primary rupture. At its propagation towards the current segment (and in the opposite direction) the new segment will be subjected to similar evolution as the current segment has been subjected. After linkage of a number of rank-II segments the next rank-III segment will be formed (shown on a smaller scale ≈ 1:5). Further development of this fault will be accompanied by creation of higher rank segments. Segments of each hierarchical rank at meeting form compressive jogs and domino-structure of corresponding rank.

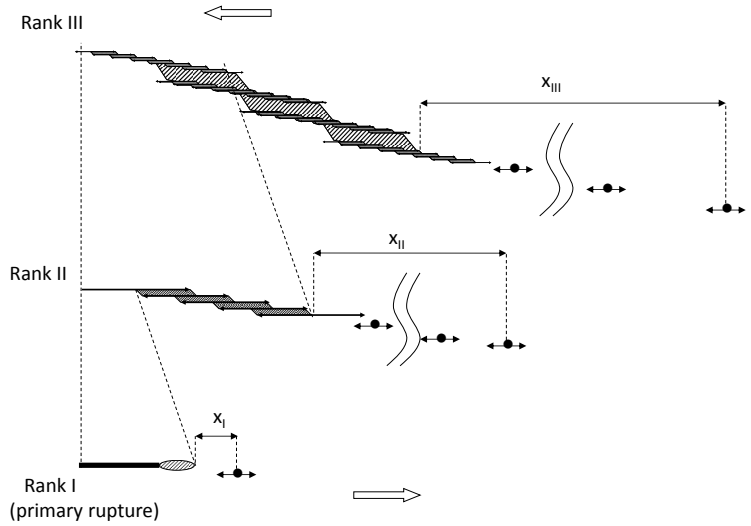

Figure 29 Evolution of a multi-hierarchical segmented fault

6.2 Formation of the fan-structure in segmented faults

Photographs in Figure 2(e) (from Ortlepp 1997) demonstrate that domino-blocks involved in complex segmented faults can be subjected to rotation by angle β due to shear displacements of the fault faces. Observations show that angle β can be relatively high, exceeding 90°. It is known that the magnitude of relative displacement between the fault faces increases with distance from the fault tip. Due to this the magnitude of angle β should also increase correspondingly with distance from the fault tip in a segmented fault as shown in Figure 30(a). Segments involving domino-blocks with different angle β can form a segmented fan-structure representing the fault head. In the front segment the domino-block orientation is α_0 and the final block position at the end of the fan-head is $(-\alpha_0)$. The segmented fan-structure has the same remarkable features as discussed for primary ruptures.

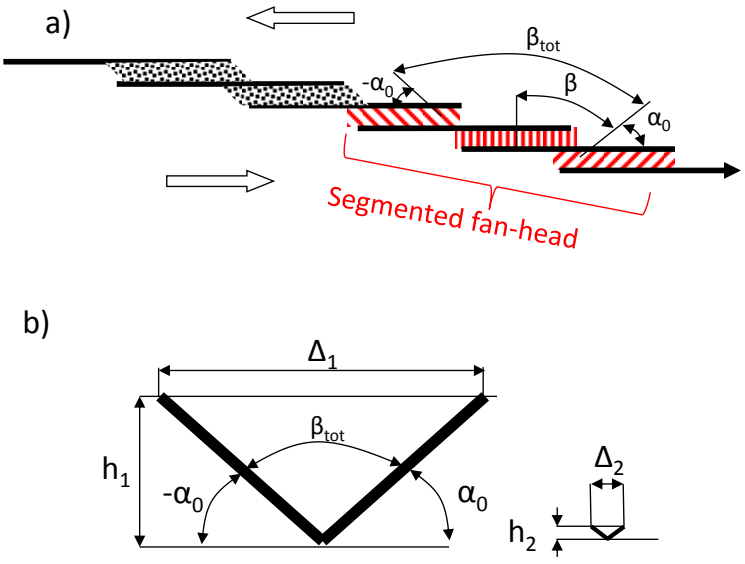

Figure 30 Principle of the fan-structure formation in segmented faults

It should be emphasised that the fan-structure can be formed if shear displacement between the fault faces is sufficient for the completed block rotation. Figure 30(b) shows the initial and final position of domino-blocks for two shear ruptures of thickness h_1 and h_2. The thick rupture requires significantly greater displacement Δ to complete the block rotation. Equation (16) allows estimating the fault displacement Δ_{fault} necessary for creation of the fan-structure:

$$\Delta_{fault} \geq \Delta_{fan} = 2h/tg\alpha_0 \qquad (16)$$

Taking into account this feature we can analyse the possibility of the fan-mechanism activation in a complex fault shown in Figure 31 (photograph from Ortlepp 1997). The structure of this fault is shown symbolically on the left. It includes primary ruptures and higher rank segments formed on the basis of compressive jogs (rank-II and rank-III). Ortlepp (1997) indicates that the magnitude of the jog (or step) of rank-III is h_{III} = 260 mm, while the magnitude of shear displacement along the fault is about 100 mm. It means that the fan-structure cannot be formed on the basis of domino-blocks of rank-III because $\Delta_{fault} < \Delta_{fan}$. However, the development of primary ruptures (rank-I) and ruptures of rank-II can be governed by the fan-mechanism because for them $\Delta_{fault} > \Delta_{fan}$.

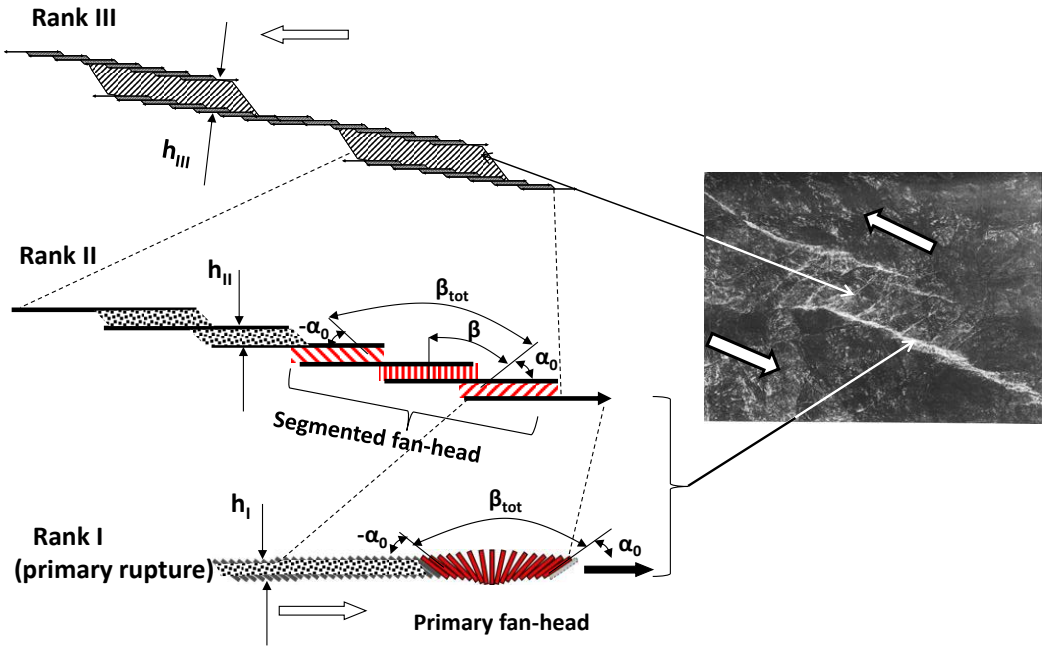

Figure 31 The fan-mechanism is predominantly activated in fault segments of lower hierarchical ranks where $\Delta_{fault} > \Delta_{fan}$

Due to this, the fan-structure (red zones in Figure 31) is predominantly created in segments of lower ranks. The fan-mechanism generated here is responsible for high dynamics of the failure process. Relatively thin localised zones of very intense destruction can be observed in each dynamic fault. The initial domino-structure of these segments is completely destroyed by extensive and violent shear and represented by pulverised gouge. This explains why the fan-structure has never been seen in nature unlike domino-structures of high rank segments observed in the myriad of different faults. In high rank segments domino-blocks rotate by low angles without destruction and accommodate displacement along the whole fault.

7 Fan-mechanism as a source of shear rupture rockbursts

7.1 General features of shear rupture rockbursts

Special studies conducted in ultra-deep South African mines (Gay & Ortlepp 1979; McGarr et al. 1979) show that shear rupture rockbursts, which are seismically indistinguishable from natural earthquakes, are caused

by the dynamic formation of new faults in pristine hard rock (dry quartzite). It was shown that these mine tremors and earthquakes share the apparent paradox of failure under low shear stress (McGarr et al. 1979). David Ortlepp, who acquired more than 40 years of experience in the study of shear rupture rockbursts in deep and ultra-deep South African mines, emphasised that:

> *"Shear rupture rockbursts nucleate in pristine rocks within the rock space at a point some considerable distance away from the surface of an opening… after which a very large amount of energy is suddenly and violently emitted from somewhere in the semi-infinite rock-space surrounding a mine, to express itself as a large rockburst. Large incidents cause damage of such intense violence that it seems that our knowledge of the mechanism of damage is completely inadequate." Ortlepp (1997); Ortlepp et al. (2005).*

Thus, main characteristic features of shear rupture rockbursts are:

- Great depths of rockburst activity.
- Generation of new faults of extreme dynamics in pristine hard rocks.
- Fault nucleation at a point considerable distance away from the opening surface.
- Fault propagation at low shear stresses.
- Abnormal violence.

Indeed it is difficult to explain the entire combination of the features of this phenomenon on the basis of the traditional understanding of rock properties and failure mechanisms. In this section we will demonstrate that all characteristic features of shear rupture rockbursts represent manifestations of the intrinsic properties of the fan-mechanism.

7.2 Shear rupture rockbursts of abnormal violence as phenomena of great depths

In Sections 5.4 and 5.5 we introduced features of variation of such properties of hard rocks as post-peak brittleness (brittleness index K_1) and transient strength τ_{fan} with variation of confining pressure σ_3 caused by the fan-mechanism. Similar variation of the same rock properties we can expect with depth supposing that minor stress σ_3 increases linearly with depth. Figure 32 shows models of depth distribution of the following parameters: a) efficiency of the fan-mechanism operation $\psi = \tau_f/\tau_{fan}$, b) rock strength, and c) rock brittleness. The models of rock strength and brittleness involve new information about rock properties associated with the fan-mechanism. They demonstrate that below a critical upper depth boundary (upper cutoff) determined by the level of minor stress $\sigma_3 = \sigma_{3fan(min)}$ (red horizontal dotted line) the fan-mechanism makes the transient rock strength less than the frictional strength and increases rock brittleness. This means that below the upper cutoff rocks acquire the capability for generation of extreme ruptures caused by the fan-mechanism and this capability increases with depth due to increase in the fan-mechanism efficiency up to a depth corresponding to $\sigma_3 = \sigma_{3fan(opt)}$. Then the fan-activity decreases and ceases at a lower critical depth (lower cutoff) characterised by $\sigma_3 = \sigma_{3fan(max)}$. Within the depth range between the upper and lower cutoffs rocks are specifically inclined to dynamic events. For different rocks the position of the upper and the lower cutoffs can be different. For the dolerite discussed in Figure 19(a) the minimum level of confining pressure at which the fan-mechanism becomes active is 60 MPa, which corresponds to a depth of about 2 km. The lower cutoff of the fan-mechanism activity is determined by levels of minor stress and temperature at which rock becomes insufficiently brittle for formation of the domino-structure. For some types of rock this depth can correspond to 20 km.

The depth of mining activity today is up to 4 km. The pink area in Figure 32 indicates symbolically the depth range within the fan active zone where the mining occurs today. It represents a quite narrow zone within the wide zone of fan-activity. Nevertheless mines located in this zone are dangerous in respect of shear rupture rockbursts and the deeper the mine the more severe rockbursts can occur due to the increase in fan-mechanism efficiency. The abnormal violence is resulted from high brittleness and low transient strength of hard rocks at these conditions, which determine the extremely low rupture energy and high elastic energy release during the rupture process (see post-peak properties of hard rocks determined by the fan-mechanism in Figure 20(c)).

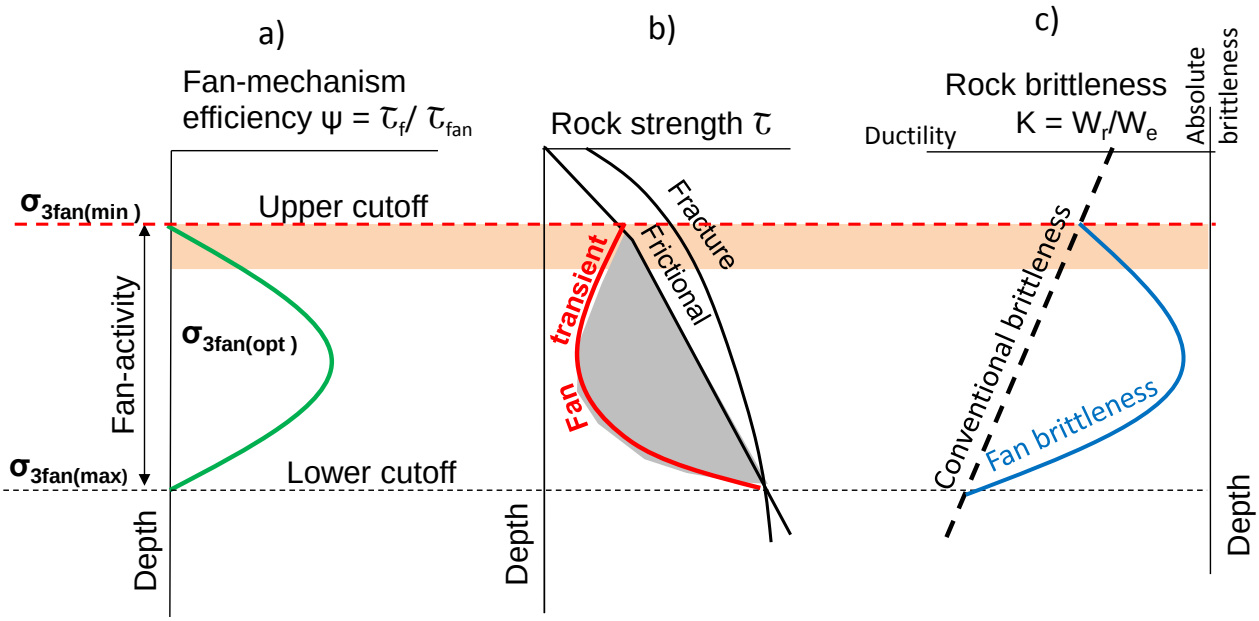

Figure 32 Variation of rock strength and brittleness with depth determined by the fan-mechanism

7.3 Generation of shear rupture rockbursts at low shear stresses

It is very important that in the zone of the fan-mechanism activity extreme ruptures creating severe shear rupture rockbursts can be generated in intact rock at shear stresses below the frictional strength. Figure 33 explains this situation. Figure 33(a) shows a fragment of the rock mass located at great depth below the upper cutoff where the minor stress σ_3 exceeds the critical level $\sigma_3 > \sigma_{3fan(min)}$. This fragment is loaded by a field shear stress τ, which is lower than the frictional strength τ_f. Relative levels of shear stresses corresponding to fracture strength τ_u, frictional strength τ_f and field stress τ are shown schematically by horizontal lines on the graph. In this situation the rock mass is in stable conditions. However, if high stress corresponding to the fracture strength τ_u is generated for some reason in a small area of this rock mass the initial fan-structure can be formed. After that the completed fan-head, with extremely low shear resistance τ_{fan}, can propagate spontaneously through the rock mass loaded by the low field stress τ because $\tau_{fan} < \tau$. This situation is graphically illustrated in Figure 33(b). The formation of the new fault will be very dynamic and violent because rupture energy provided by the fan-mechanism is extremely low. Local high stresses causing the initial formation of the fan-structure can be generated on the basis of pre-existing discontinuities representing stress concentrators.

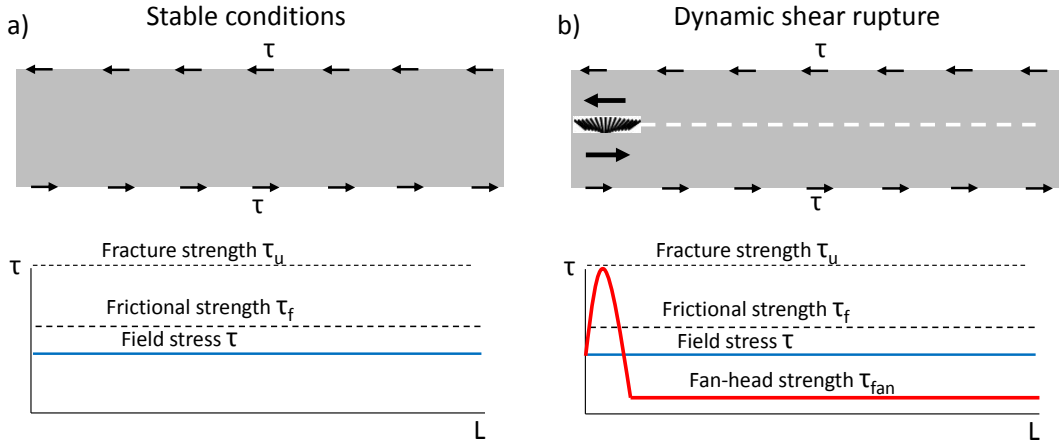

Figure 33 Principle of a new dynamic fault generation in pristine rock at low field stress governed by the fan-mechanism

7.4 Fault nucleation at a considerable distance away from the opening

Figure 34(a) shows a cross-section of the Earth's crust involving an opening made in hard rock. The left graph illustrates depth distribution of minor stress σ_3 in the area involving the opening. The fan-mechanism can be activated below the upper cutoff corresponding to the critical level of minor stress $\sigma_{3fan(min)}$. The fan-mechanism efficiency $\psi = \tau_f/\tau_{fan}$ is a function of σ_3. The right green graph symbolically reflects the depth distribution of the fan-mechanism efficiency. It shows that around the opening, the minor stress is below the critical level $\sigma_3 < \sigma_{3fan(min)}$ at which $\psi = 1$ (on the opening surface $\sigma_3 = 0$). Hatched areas in Figure 34(a) show zones where the fan-mechanism cannot be generated. The zone of the fan-mechanism activity is shown by the grey area.

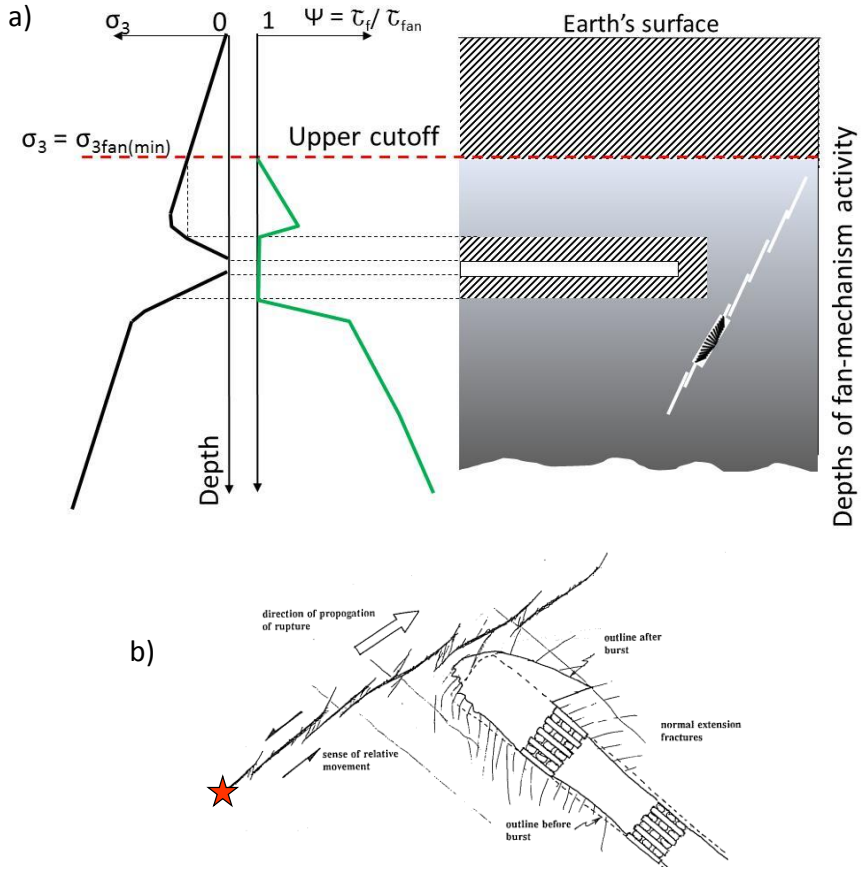

Figure 34 Fault nucleation away from the opening surface caused by the fan-mechanism

Deep openings change the stress conditions in the surrounding rock mass. If mine induced stress locally reaches the level of ultimate stress τ_u somewhere in the grey area in Figure 34(a), the fan-structure will be generated in pristine rocks. This can happen within the rock space at a point some considerable distance away from the surface of an opening because around the opening $\sigma_3 < \sigma_{3fan(min)}$. After formation of the fan-head, further spontaneous propagation of the new fault characterised by extremely low rupture energy will be accompanied by the release of very large amounts of energy suddenly and violently emitted from the semi-infinite rock-space surrounding a mine, to express itself as a rockburst, as David Ortlepp indicated. Figure 34(b) from Ortlepp (1997) illustrates relative positions of the opening and new rupture, which created a shear rupture rockburst. The asterisk indicates the point of shear rupture nucleation.

8 Fan-mechanism as a source of earthquakes

8.1 Earthquakes generated by extreme ruptures in intact rock mass

It is generally accepted that the main earthquake mechanism is frictional stick-slip instability on pre-existing faults. During the last two decades the research interest has been concentrated on study of extreme ruptures which can propagate along pre-existing frictional interfaces with high velocities up to supershear levels at low shear stresses (significantly below the frictional strength) due to strong interface weakening in the rupture head. Analysis of laboratory results conducted in Section 4 shows that supershear velocities in frictional interfaces were reached on extremely smooth faults only (roughness 1–10 μm). In rougher faults and in faults involving gouge extreme rupture velocities are not achievable. The explanation for this fact is as follows. According to the new approach, the fan-structure of extremely low shear resistance can be generated in smooth faults because at these conditions very short domino-blocks formed from 'welded' asperities can withstand rotation without collapse. Larger asperities do not provide conditions for formation of domino-blocks of the proper geometry. Due to this at relative displacement of the rupture faces the domino-blocks collapse and create gouge providing common friction in the rupture head. The presence of gouge in the interface before the rupture generation excludes conditions for formation of domino-blocks.

We can suppose that by analogy with the laboratory results extreme ruptures can propagate along natural pre-existing faults if interface conditions provide the fan-mechanism activation. The fan-mechanism cannot be generated within fresh faults with gauge between the fault faces. Seismic data and geologic observations suggest that faults strengthen (heal) during the interseismic period of the earthquake cycle due to metamorphism and intruding igneous rocks. When the structure of the healed fault becomes monolithic and strong enough for the creation of domino-blocks capable of rotating without collapse, the fan-mechanism can be generated in pre-existing faults. So, the fan-mechanism operation in pre-existing faults is restricted by conditions of the interface structure.

At the same time, the fan-mechanism can operate in intact hard rocks at stress conditions corresponding to seismogenic depths without restrictions. Due to extremely low transient strength of intact hard rocks caused by the fan-mechanism, earthquake ruptures can be generated at low shear stresses. The fact that earthquakes are commonly attributed to pre-existing faults can be explained as follows. Pre-existing discontinuities play the role of local stress concentrators, creating the starting conditions for the fan-structure formation. However, after completion of the initial fan-structure it can create a new dynamic fault in the form of earthquake by propagation through intact rock mass subjected to low shear stresses. This supposition is supported by observations of shear ruptures generated in intact rocks and caused severe rockbursts, as discussed in Section 6.

Figure 35 shows an example of how a new fault can be generated in intact rock in vicinity of a pre-existing fault by the fan-mechanism. In Figure 35(a) a rock fragment involving a fault with a compressive jog is subjected to stress conditions corresponding to point R in Figure 35(b), for which $\tau = \tau_{(R)}$ and $\sigma_3 = \sigma_{3(R)}$. Figure 35(b) represents strength profiles characterising rock strength at different depths (or σ_3) as discussed in Figures 26(a) and 32(b). Because shear stress $\tau_{(R)}$ affecting the fault is significantly less than the frictional strength $\tau_{f(R)}$ at his depth, the fault condition is absolutely stable (safe condition). However, the pre-existing segmented fault represents a stress concentrator. Under the effect of shear stresses $\tau_{(R)}$ applied a high local stress can be created in the jog zone delineated by red circle. If the local stress in this zone reaches the level of rupture strength $\tau_{u(R)}$ the fan-structure can be formed, after which a new extreme rupture will propagate through the intact rock mass loaded by low stress $\tau_{(R)}$ (blue line in Figure 35(d)). The new rupture governed by the fan-mechanism can be accompanied by abnormal energy release and violence.

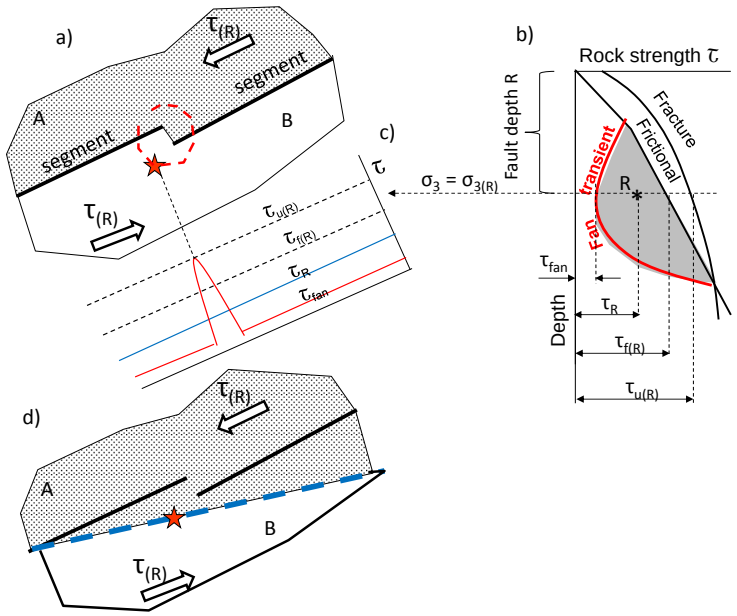

Figure 35 Features of generation of a new extreme rupture in pristine rock mass in the vicinity of a pre-existing fault at low field shear stresses caused by the fan-mechanism

8.2 Small stress-drop at rupture of intact rocks

The static stress-drop is one of the most important and frequently used source parameters of earthquakes. In the context of earthquake rupture, stress-drop is the difference between the stress across a fault before and after an earthquake rupture. Stress-drop is related to the energy released as a consequence of an earthquake rupture (expressed by its seismic moment or magnitude) and to the dimensions of the rupture. Numerous laboratory studies initiated by the work of Brace and Byerlee (1966) showed that repeatable stick-slip instability on pre-cut specimens is accompanied by relatively small magnitudes of stress-drop, which is typical for earthquakes, in contrast to the large stress-drops observed at failure of intact specimens of all types of rock. These experimental observations support the modern frictional stick-slip concept.

Stress-displacement curves in Figures 36(a)–36(c) illustrate schematically the difference in stress-drop $\Delta\tau$ and released energy (yellow area) for different rock specimens tested under soft loading conditions. Red dotted lines here characterise stiffness of the loading system. Figure 36(a) represents stick-slip along a pre-existing rupture with small stress-drop $\Delta\tau$. Curves in Figures 36(b) and 36(c) reflect post-peak properties of intact rocks associated with propagation of a shear rupture governed by the conventional (frictional) rupture mechanism and by the fan-mechanism (see explanation in Figures 20(c) and 20(d)). The failure of intact rocks for both rupture mechanisms is accompanied by the same large stress-drop $\Delta\tau$ compared with the stick-slip situation in Figure 36(a). However, in natural conditions the fan-mechanism can provide very low static stress-drop when shear rupture is generated in intact rock at low shear stresses. This situation is explained in Figures 36(d)–36(g).

Figure 36(d) shows strength profiles characterising rock strength at different σ_3 (or corresponding depths) as discussed in Figure 26(a) and 32(b). Let us consider the situation at point R characterised by the field stress $\tau = \tau_{(R)}$ and $\sigma_3 = \sigma_{3(R)}$. The graph in Figure 36(e) represents a hypothetical stress versus displacement (τ–d) curve reflecting the loading of the field scale intact rock mass at confining stress $\sigma_3 = \sigma_{3(R)}$ up to $\tau = \tau_{(R)}$. The applied shear stress $\tau_{(R)}$ is significantly less than the frictional strength $\tau_{f(R)}$ which implies stable (safe) conditions according to the conventional frictional concept. The red dotted line here indicates symbolically the loading stiffness. However, if for some reason (natural or artificial), a high local stress generates the initial fan-structure, a new large dynamic fault will be created by the fan-head spontaneously propagating through the intact rock mass. This failure process is illustrated in Figure 36(f). The energy release here corresponding to the yellow area is relatively high. However, the static stress-drop $\Delta\tau_{fan}$ caused by shear rupture propagation in intact rock in this situation can be very small. Figure 36(g) shows that, after failure

at the stress level $\tau = \tau_{(R)}$, the failed rock mass can be loaded stably, up to the frictional strength $\tau = \tau_{f(R)}$. Once the field stress reaches the level $\tau = \tau_{f(R)}$ frictional stick-slip instability can be generated along the same fault. Figures 36(f) and 36(g) illustrate that the fan-mechanism can provide smaller stress-drop $\Delta\tau_{fan}$ compared with the stick-slip mechanism $\Delta\tau_f$. At the same time the energy release (yellow areas) associated with the fan-mechanism is higher compared with the stick-slip frictional mechanism. The combination of very small stress-drop with high energy release is one more paradoxical feature of the fan-mechanism.

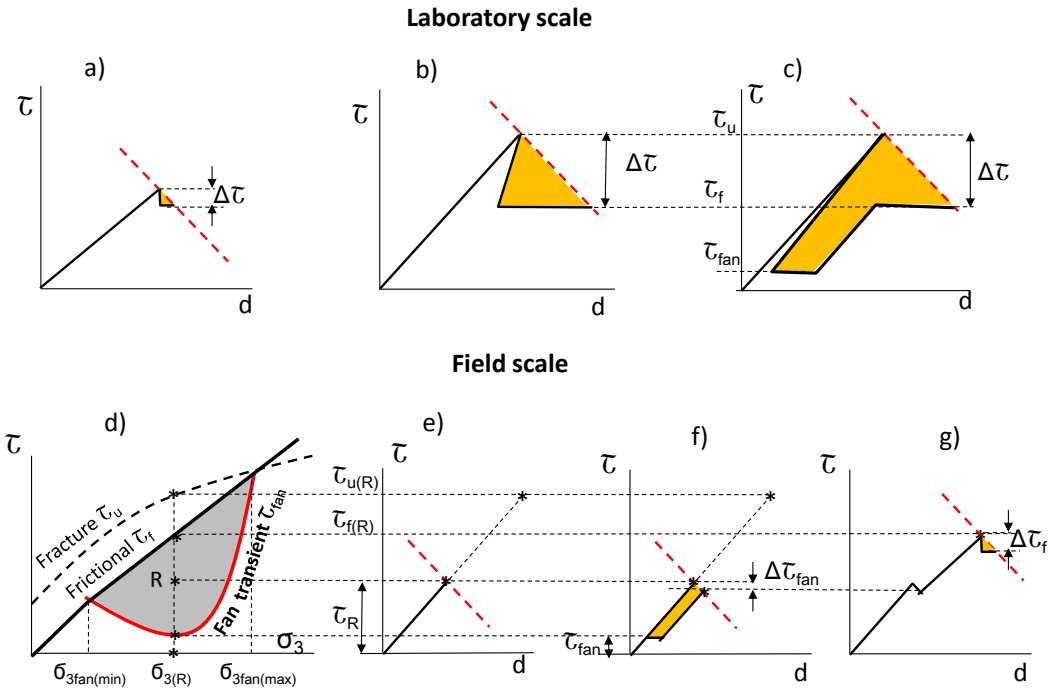

Figure 36 Features of stress-drop and energy release associated with rock failure caused by shear rupture propagation in (a)–c) laboratory specimens and (d)–(g) in natural conditions

8.3 Depth distribution of lithospheric strength and earthquake activity

It is generally accepted that the depth lithospheric strength distribution in the upper crust is determined by Byerlee's friction law, while in the lower crust it follows a high-temperature steady-state flow law (Byerlee 1978; Brace & Kohlstedt 1980; Scholz 2002). In Figure 37(b) this model of lithospheric strength distribution is represented by the frictional and creep curves. Taking into account the fact that the fan-mechanism operates in strong and brittle rocks, we can suppose that the depth range of the fan-mechanism activity should be above a zone of brittle-plastic transition. Colour curves in Figures 37(a)–37(c) show correspondingly depth distributions of the following parameters determined by the fan-mechanism: efficiency of the fan-mechanism operation, rock transient strength, and rock brittleness. Figure 37(d) represents a typical histogram of depth distribution of earthquake frequency.

The improved model of lithospheric strength (Tarasov 2013; Tarasov & Randolph 2016) in Figure 37(b) shows that at depths corresponding to $\sigma_3 < \sigma_{3fan(min)}$ the lithospheric strength is determined solely by friction. Within the depth range of the potential fan-mechanism activity the situation is very specific. In the absence of conditions for activation of the fan-mechanism, the lithospheric strength is determined by friction. However, if the fan-mechanism is activated somewhere, the transient lithospheric strength in that region is determined by the fan strength. After completion of the failure process the lithospheric strength corresponds again to the frictional strength. It should be noted that the improved concept of the lithospheric strength incorporates all three types of rock strength determining the instability in the seismogenic layer: fracture strength τ_u, frictional strength τ_f, and fan-strength τ_{fan}. The fracture strength determines the level of local stress at which the initial fan-structure can be generated. The shaded area between the frictional and the fan transient profiles determines the field stress conditions under which the initiated fan-structure can propagate creating the earthquake.

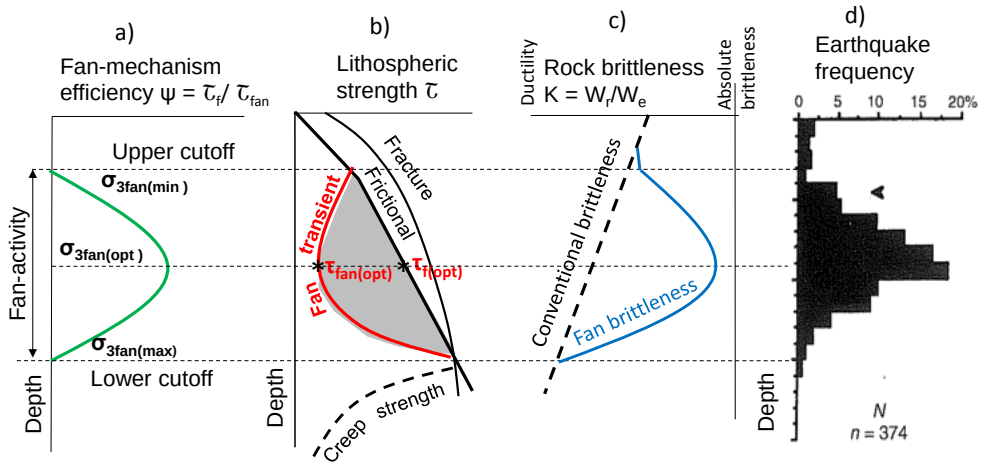

Figure 37 Relation between depth distribution of the fan-mechanism efficiency, lithospheric strength, rock brittleness and earthquake frequency

Importantly, the fan-mechanism can cause earthquakes at any level of field stress τ within the shaded zone. Due to this the highest probability of events is at a depth characterised by the maximum range between τ_{fan} and τ_f. This depth corresponds approximately to the depth of optimal efficiency of the fan-mechanism. At lower and greater depths the probability decreases. This feature determines the typical depth-frequency distribution of earthquake hypocentres. High rock brittleness caused by the fan-mechanism assists to rupture propagation with extreme dynamics. Variation in rock brittleness (blue curve in Figure 37(c)) is in accord with the typical distribution of earthquake frequency. The explanation for the depth distribution of earthquake frequency on the basis of the fan-mechanism differs fundamentally from the conventional explanation based on the velocity-weakening-strengthening concept (e.g. Scholz 1998, 2002). According to the new approach, the upper and lower cutoffs are determined by the zone of the fan-mechanism activity.

The fan-mechanism causes the following paradoxical effect. The transient low strength of intact rock below the frictional strength ($\tau_{fan} < \tau_f$) favours the generation of new faults in the strong intact rock mass adjoining a pre-existing fault in preference to frictional stick-slip instability along the weak fault. This is because the fan-mechanism can provide the formation of new dynamic faults in intact rock at stresses significantly below the frictional strength. Each earthquake generated by the fan-mechanism is associated with formation of a new fault at a new location but in the vicinity of a pre-existing fault which services as a stress concentrator causing the formation of the initial fan-structure. This explains the spatial distribution of the earthquake hypocentres and the fact that the Earth's crust is riddled with faults. Figure 38 illustrates this feature. It shows a set of earthquake faults generated in New Zealand. Different faults are associated with different earthquakes.

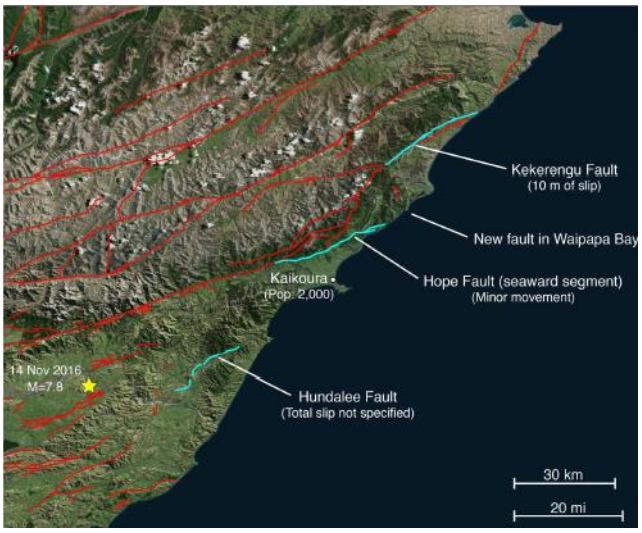

Figure 38 A map of activated faults in New Zealand (Temblor 2017)

8.4 Earthquakes in complex crust consisting of two layers of different rocks

Experiments (Tarasov 2010; Tarasov & Randolph 2011) have shown that the efficiency of the fan-mechanism depends on the rock strength: the stronger the rock, the greater the fan-mechanism efficiency and the wider the confining pressure range over which the fan-mechanism is active (see Figure 22). Figure 39(a) illustrates schematically depth distributions of the fan-mechanism activity for four rocks characterised by different strength, with strength increasing from rock 1 to rock 4. Figure 39(b) shows a situation when the Earth's crust is represented by two layers of rocks of different strength (rock 1 and rock 3). In this case, two zones of earthquake activity may be observed. Rock 1 will exhibit the typical (complete) form of earthquake activity depth distribution, while rock 3 will show a truncated form. Such features of earthquake behaviour have been observed in nature (e.g. Albaric et al. 2009).

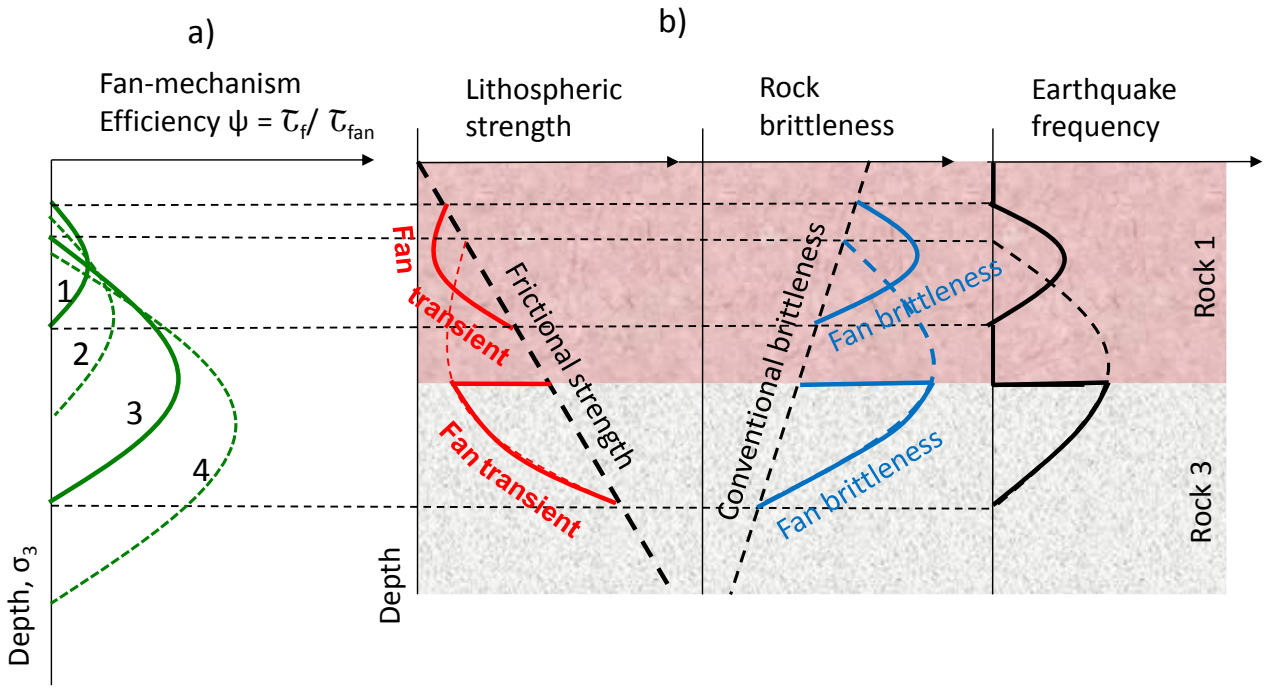

Figure 39 Illustration of depth distribution for rock transient strength, brittleness and earthquake frequency in the Earth's crust represented by two layers of rocks of different strength

9 Conclusion

This paper proposes that shear ruptures of extreme dynamics (up to supersonic velocities) propagating in intact rocks and in pre-existing frictional and coherent interfaces are governed by the same mechanism that is associated with an intensive microcracking process in the rupture tip observed for all types of extreme ruptures. The microcracking process creates, in certain conditions, a special fan-like microstructure shear resistance of which is extremely low (up to an order of magnitude less than the frictional strength). The fan-structure representing the rupture head provides strong interface weakening and causes high slip and extreme rupture velocities. The fan-mechanism differs remarkably from all reported earlier mechanisms.

This paper briefly discusses the physical and mathematical models of the fan-mechanism and analyses such unique features of the fan-structure as the capability to cause dramatic strength weakening and significant intensification of tensile and shear stresses in the rupture head. Different features observed in experiments on extreme ruptures are explained on the basis of the fan-mechanism. Some of these features are:

- Dramatic embrittlement of hard rocks at highly confined compression.
- Extremely low transient material strength during the rupture process.

- The release of an abnormally high amount of elastic energy at failure of hard rocks at highly confined compression.
- Transition from pulse-like to crack-like (and vice versa) rupture mode at variation in stress conditions.
- Off-fault tensile cracking in a bonded interface and the absence of cracks in the frictional interface.
- Two stages of the spontaneous rupture development: rupture acceleration and constant high rupture velocity.
- The relationship between the slip and rupture velocities.
- The influence of the interface smoothness on the rupture velocity.

Features of the fan-mechanism activation in natural complex faults have been discussed. Alternative mechanisms of shear rupture rockbursts and earthquakes based on the fan-mechanism have developed. The new approach can explain the following combination of characteristic features of shear rupture rockbursts:

- Great depths of rockburst activity.
- Generation of new faults of extreme dynamics in pristine hard rocks.
- Fault nucleation at a point of a considerable distance away from the opening surface.
- Fault propagation at low shear stresses.
- Abnormal violence.

This paper has proposed an improved concept of lithospheric strength and earthquake activity at shallow depths. The improved concept proposes an alternative explanation for different earthquake features, such as:

- Upper and lower cutoffs.
- The typical shape of depth distribution of earthquake hypocentres.
- Potentially low magnitudes of stress drop.
- Observed spatial patterns of earthquake occurrence, etc.

Acknowledgement

The authors acknowledge the support provided by the Centre for Offshore Foundation Systems (COFS) at the University of Western Australia, which was established under the Australian Research Council's Special Research Centre scheme. I am very grateful to the Conference Chair, Dr Johan Wesseloo, for inviting me as a keynote speaker and for very useful comments and suggestions made during the preparation of this paper.

References

Albaric, J, Deverchere, J, Petit, C, Perrot, J & Le Gall, B 2009, 'Crustal rheology and depth distribution of earthquakes: Insights from the central and southern East African Rift System', *Tectonophysics*, vol. 468, pp. 28–41.

Andrews, DJ & Ben-Zion, Y 1997, 'Wrinkle-like slip pulse on a fault between different materials', *Journal of Geophysical Research*, vol. 102, pp. 553–71.

Ben-David, O, Rubinstein, SM & Fineberg, J 2010, 'Slip-stick and the evolution of frictional strength', *Nature,* vol. 463, pp. 76–79.

Ben-Zion, Y 2001, 'Dynamic ruptures in recent models of earthquake faults', *Journal of the Mechanics and Physics of Solids,* vol. 49, pp. 2209–2244.

Brace, WF & Kohlstedt, D 1980 'Limits on lithospheric stress imposed by laboratory experiments', *Journal of Geophysical Research*, vol. 85, pp. 6248-6252.

Brace, WF & Byerlee, JD 1966, 'Stick-slip as a mechanism for earthquakes, *Science,* vol. 153 (3,739), pp. 990–992.

Bowden, FP & Tabor, D 2001, *The friction and lubrication of solids*, Oxford University Press.

Brune, JN, Brown, S & Johnson, PA 1993, 'Rupture mechanism and interface separation in foam rugger model of earthquakes: a possible solution to the heat flow paradox and the paradox of large overthrusts', *Tectonophysics*, vol. 218, pp. 59–67.

Brune, JN, Henyey, TL & Roy, RF 1969, 'Heat flow, stress, and rate of slip along the San Andreas fault, California', *Journal of Geophysical Research,* vol. 74, pp. 3821–3827.

Byerlee, JD 1978, 'Friction of rocks', *Pure and Applied Geophysics*, vol. 116, pp. 615–626.

Cochard, A & Madariaga, R 1994, 'Dynamic faulting under rate-dependent friction', *Pure and Applied Geophysics,* vol. 142, no. 3/4, pp. 419–445.

Dieterich, JH 1979, 'Modeling of rock friction; 1. Experimental results and constitutive equations', *Journal of Geophysical Research,* vol. 84, pp. 2162–2168.

Di Toro, G, Goldsby, DL & Tullis, TE 2004, 'Friction falls towards zero in quartz rock as slip velocity approaches seismic rates', *Nature* vol. 427, pp. 436–439.

Gay, N C & Ortlepp, W D 1979, 'Anatomy of a mining-induced fault zone', *Geological Society of America Bulletin*, vol. 90, pp. 47–58.

Ghaffari, HO, Thompson, BD & Young, RP 2014, 'Complex networks and waveforms from acoustic emissions in laboratory earthquakes', *Nonlinear Processes in Geophys*ics, vol. 21, pp. 763–775.

Griffith, WA, Rosakis, A, Pollard, DD & Ko, CW 2009, 'Dynamic rupture experiments elucidate tensile crack development during propagating earthquake ruptures', *Geology,* vol. 37, pp. 795–798.

Heaton, TH 1990, 'Evidence for and implications of self-healing pulses of slip in earthquake rupture', *Physics of the Earth and Planetary Interiors,* vol. 64, no. 1, pp. 1–20.

Horii, H & Nemat-Nasser, S 1985, 'Compression-induced micro-crack growth in brittle solids: axial splitting and shear failure', *Journal of Geophysical Research*, vol. 90, pp. 3105–3125.

Kanamori, H & Heaton, TH 2000, 'Microscopic and macroscopic physics of earthquakes', in JB Rundle, DL Turcotte & W Klein (eds), *Geophysical Monograph Series: Geo Complexity and the Physics of Earthquakes*, American Geophysical Union, Washington DC, vol. 120, pp. 147–163.

King, GCP & Sammis, CG 1992, 'The mechanisms of finite brittle strain', *Pure and Applied Geophysics,* vol. 138, pp. 611–640.

Kostrov, B 1966, 'Self-similar problems of propagation of shear cracks', *Journal of Applied Mathematics and Mechanics*, vol. 28, pp. 1077-1078.

Lachenbruch, AH 1980, 'Frictional heating, fluid pressure, and the resistance to fault motion', *Journal of Geophysical Research,* vol. 85, pp. 6097–6112.

Lei, X, Kusunose, K, Rao, MVMS, Nishizawa, O & Satoh, T 2000, 'Quasi-static fault growth and cracking in homogeneous brittle rock under triaxial compression using acoustic emission monitoring', *Journal of Geophysical Research,* vol. 105, pp. 6127–6139.

Lu, X, Lapusta, N & Rosakis, AJ 2007, 'Pulse-like and crack-like ruptures in experiments mimicking crustal earthquakes', *Proceedings of the National Academy of Science USA*, vol. 104, pp. 18931–18936.

Lu, X, Lapusta, N & Rosakis, AJ 2010, 'Pulse-like and crack-like dynamic shear ruptures on frictional interfaces: experimental evidence, numerical modeling, and implications', *International Journal of Fracture,* doi:10.1007/s10704–010–9479–4, pp. 27–39.

Lykotrafitis, G, Rosakis, A J & Ravichandran, G 2006, 'Self-healing pulse-like shear ruptures in the laboratory', *Science*, vol. 313, pp. 1765–1768.

Magloughlin, JF & Spray, JG 1992, 'Frictional melting processes and products in geological materials: introduction and discussion', *Tectonophysics,* vol. 204, pp. 197–206.

Megahid, AR, Soghair, H, Hageed, MAA & Hafer AMAA 1993, 'Strength and deformation capacity of slender RC beams', in HP Rossmanith (ed.), *Proceedings Fracture and Damage of Concrete and Rock – FDCR-2*.

Melosh, HJ 1979, 'Acoustic fluidization: a new geologic process?', *Journal of Geophysical Research,* vol. 84, pp. 7513–7520.

McGarr, A, Pollard, D, Gay, NC & Ortlepp, WD 1979, 'Observations and analysis of structures in exhumed mine-induced faults', *U.S. Geological Survey Open File Report*, vol. 79 – 1239, pp. 101–120.

Ngo, D, Huang, Y, Rosakis, A, Griffith, W A & Pollard, D 2012, 'Off-fault tensile cracks: a link between geological fault observations, lab experiments, and dynamic rupture models', *Journal of Geophysical Research,* vol. 117, doi: 10.1029/2011JB008577.

Ohnaka, M & Kuwahara, Y 1990, 'Characteristic features of local breakdown near a crack-tip in the transition zone from nucleation to unstable rupture during stick-slip shear failure', *Tectonophysics,* vol. 175, pp. 197–220.

Ohnaka, M & Shen, L 1999, 'Scaling of the shear rupture process from nucleation to dynamic propagation: implications of geometric irregularity of the rupturing surface', *Journal of Geophysical Research,* vol. 104, pp. 817–844.

Olsen, KB, Madariaga, R & Archuleta, RJ 1997, 'Three-dimensional dynamic simulation of the 1992 Landers earthquake', *Science,* vol. 278, pp. 834–838.

Ortlepp, WD 1997, *Rock Fracture and Rockbursts*, The South African Institute of Mining and Metallurgy, Johannesburg.

Ortlepp, WD, Armstrong, R, Ryder, JA & O'Connor, D 2005, 'Fundamental study of micro-fracturing on the slip surface of mine-induced dynamic brittle shear zones', in Y Potvin & M Hudyma (eds), *Proceedings of the 6th International symposium on Rockburst and Seismicity in Mines*, Australian Centre for Geomechanics, Perth, pp. 229–237.

Otsuki, K & Dilov, T 2005, 'Evolution of hierarchical self-similar geometry of experimental fault zones: Implications for seismic nucleation and earthquake size', *Journal of Geophysical Research,* vol. 110, B03303, doi: 10.1029/204JB003359.

Peng, S & Johnson, AM 1972, 'Crack growth and faulting in cylindrical specimens of Chelmsford granite', *International Journal of Rock Mechanics and Mining Sciences,* vol. 9, pp. 37–86.

Reches, Z & Lockner, D A 1994, 'Nucleation and growth of faults in brittle rocks', *Journal of Geophysical Research,* vol. 99, pp. 18159–18173.

Rice, JR 1992, 'Fault stress states, pore pressure distributions, and the weakness of the San Andreas fault', *Fault Mechanics and Transport Properties of Rocks*, Academic, San Diego, California, pp. 475–503.

Rice, JR 2006, 'Heating and weakening of faults during earthquake slip', *Journal of Geophysical Research,* vol. 111, B05311, doi: 10.1029/2005JB004006.

Richards, PG 1976, 'Dynamic motions near an earthquake fault: a three-dimensional solution', *Bulletin of Seismological Society of America*, vol. 66, pp. 1–32.

Rosakis, A J 2002, 'Intersonic shear cracks and fault ruptures', *Advances in Physics,* vol. 51, pp. 1189-1257.

Rosakis, AJ, Samudrala, O & Coker, D 1999, 'Cracks faster than the shear wave speed', *Science*, vol. 284, pp. 1337–1340.

Rubinstein, S M, Cohen, G & Fineberg, J 2004, 'Detachment fronts and the onset of dynamic friction', *Nature,* vol. 430, pp. 1005–1009.

Rummel, F & Fairhurst, C 1970, 'Determination of the post-failure behavior of brittle rock using a servo-controlled testing machine', *Rock Mechanics and Rock Engineering,* vol. 2, no. 4, pp. 189–204.

Samudrala, O, Huang, Y & Rosakis, AJ 2002, 'Subsonic and intersonic shear rupture of weak planes with a velocity weakening cohesive zone', *Journal of Geophysical Research,* vol. 107 (B8), pp. 2,170, doi:10.1029/2001JB000460.

Scholz, CH 1998, 'Earthquakes and friction laws', *Nature*, vol. 391, pp. 37–42.

Scholz, CH 2002, *The mechanics of earthquakes and faulting*, Cambridge University Press, Cambridge.

Segal, P & Pollard, DD 1980, 'Mechanics of discontinuous faulting', *Journal of Geophysical Research*, vol. 85, pp. 4337–4350.

Sibson, RH 1982, 'Fault zone models, heat flow, and the depth distribution of earthquakes in the continental crust of the United States', *Bulletin of the Seismological Society of America*, vol. 72, pp. 151–163.

Sibson, R 1992, 'Power dissipation and stress levels during seismic faulting', *Journal of Geophysical Research,* vol. 85, pp. 6239–6247.

Stavrogin, AN & Tarasov, BG 2001, *Experimental Physics and Rock Mechanics*, Balkema, Rotterdam.

Tarasov, BG 2010, 'Superbrittleness of rocks at high confining pressure', in M Van Sint Jan & Y Potvin (eds), *Proceedings of the Fifth International Seminar on Deep and High Stress Mining*, Australian Centre for Geomechanics, Perth, pp. 119–133.

Tarasov, BG 2013, 'Depth distribution of lithospheric strength determined by the self-unbalancing shear rupture mechanism', in *Proceedings of the International Symposium, Rock Mechanics for Resources, Energy and Environment (Eurock),* Wroclaw, Poland, pp. 165-170.

Tarasov, BG 2014, 'Hitherto unknown shear rupture mechanism as a source of instability in intact hard rocks at highly confined compression', *Tectonophysics,* vol. 621, pp. 69–84.

Tarasov, BG 2014a, 'Fan-structure shear rupture mechanism as a source of shear rupture rockbursts, *Journal of the Southern African Institute of Mining and Metallurgy*, vol. 114, no. 10, pp. 773–784.

Tarasov, BG 2016a, 'Shear fractures of extreme dynamics', *Rock Mechanics and Rock Engineering*, vol. 49, no. 10, pp. 3999–4021.

Tarasov, B 2016b, *Fan-hinged shear*, online video, 19 July, viewed 6 December 2016, https://www.youtube.com/watch?v=_-AUzCEw35M&feature=youtu.be

Tarasov, BG 2016c, 'Low transient strength of hard rocks at spontaneous failure', in *Proceedings of the 2nd International Conference on Rock Dynamics and Applications (RocDyn-2)*, Suzhou, China, pp. 503–509.

Tarasov, BG & Ortlepp, WD 2007, 'Shock loading-unloading mechanism in rockburst shear fractures in quartzite causing genesis of polyhedral sub-particle in the fault gouge', in Y Potvin (ed.) *Proceedings of the Fourth International Seminar on Deep and High Stress Mining*, Australian Centre for Geomechanics, Perth, pp. 183–192.

Tarasov, BG & Randolph, MF 2011, 'Superbrittleness of rocks and earthquake activity', *International Journal of Rock Mechanics and Mining Science*, vol. 48, pp. 888–898.

Tarasov, B & Potvin, Y 2013, 'Universal criteria for rock brittleness estimation under triaxial compression', *International Journal of Rock Mechanics and Mining Science*, vol. 59, pp. 57–69.

Tarasov, BG & Guzev, MA 2013, 'New insight into the nature of size dependence and the lower limit of rock strength', in AD Malovichko (ed.), *Proceedings 8th International Symposium on Rockbursts and Seismicity in Mines*, St-Petersburg, Russia, pp. 31–40.

Tarasov, BG & Randolph, MF 2016, 'Improved concept of lithospheric strength and earthquake activity at shallow depths based upon the fan-head dynamic shear rupture mechanism', *Tectonophysics,* vol. 667, pp. 124–143.

Temblor 2017, *Temblor*, http://www.temblor.net

Van Aswegen, G 2008, 'Ortlepp shears — dynamic brittle shears of South African gold mines', in Y Potvin, J Carter, A Dyskin & R Jeffrey (eds), *Proceedings of the First Southern Hemisphere International Rock Mechanics Symposium*, vol. 2, Australian Centre for Geomechanics, Perth, pp. 111–120.

Wawersik, WR & Brace, WF 1971, 'Post-failure behaviour of a granite and diabase', *Rock Mechanics*, vol. 3, pp. 61–85.

Wawersik, WR & Fairhurst, C 1970, 'A study of brittle rock fracture in laboratory compression experiments', *International Journal of Rock Mechanics and Mining Science,* vol. 7, pp. 561–575.

Wen, YY, Ma, KF, Song, TRA & Mooney WD 2009, 'Validation of the rupture properties of the 2001 Kunlun, China (Ms = 8.1), earthquake from seismological and geological observations', *Geophysical Journal International*, vol. 177, pp. 555–570.

Xia, K, Rosakis, A J & Kanamori, H 2004, 'Laboratory earthquakes: the sub-Rayleigh-to-supershear rupture transition', *Science,* vol. 303, pp. 1859–1861.

Zheng, G & Rice, JR 1998, 'Conditions under which velocity-weakening friction allows a self-healing versus a crack-like mode of rupture', *Bulletin of the Seismological Society of America,* vol. 88, pp. 1466–1483.